UNIVERSITÀ DEGLI STUDI DI TRIESTE

XXXI CICLO DEL DOTTORATO DI RICERCA IN

NANOTECNOLOGIE

HETERO-INTERFACES: FUNCTIONAL MOLECULAR FILMS AND LOW DIMENSIONAL MATERIALS

Settore scientifico-disciplinare: **FIS/03**

DOTTORANDO
Matuš Stredansky

COORDINATORE
Prof.ssa Lucia Pasquato

SUPERVISORE DI TESI
Prof. Alberto Morgante

ANNO ACCADEMICO 2017/2018

One must still have chaos in oneself to be able to give birth to a dancing star.

Friedrich Nietzsche

ABSTRACT

The aim of this PhD work is to study the formation and the electronic and morphologic properties of complex organo-metallic and hetero-organic architectures, grown on metal surfaces via a bottom-up approach. Different systems have been investigated, in order to monitor distinct situations occurring on a surface. The largest part of this work has been focused on the boroxine-based systems. This covalently-bonded films have been explored with a multi-technique approach that allowed a deeper insight in their nature. We have prepared a novel 2D material based on the boroxine unit and consisting in boron and oxygen atoms only. Moreover, we have found interesting electronic properties, such as a channel for ultra-fast charge delocalization toward the golden substrate in all the boronic systems and a dispersion in the valence band for this 2D material. These results allow to gain a new perspective in the boroxine based systems. From material mostly known for their morphological properties, we have highlighted the presence of interesting electronic properties. In addition to the covalently bonded boroxine systems, we have focused also on the possibility of building more complex architectures upon metallic substrates via weak interactions. In particular, we have taken advantage of one of the already investigated boroxine systems to study the interplay between the boron molecule, acting as a Lewis acid, and an amine acting as a Lewis base. We have evidenced a very interesting morphological change confirming that the interaction has taken place. Similarly, we have built another complex architecture relying on weak interactions. We have taken advantage of a H-bonding to anchor a crown ether derivative on a substrate. Then we used the interaction between sodium and crown ethers to trap an alkali metal on the surface. In this experiment, we have used the crown ether for the first time on a substrate in UHV, and we have found that the affinity toward the metal is preserved. The last investigated system is also characterized by the presence of weak interactions between the molecules deposited on the surface. Despite of this similarity with the previous scientific case, the application target was completely different. We were not interested in building structures on a substrate, but we decided to take advantage offered by the UHV to study the behavior of molecules important in catalysis. In this case, we have studied the melamine and melem molecules, precursors of the 2D carbon nitride, an interesting photocatalyst for the water splitting reaction. This approach has been successful, and we gained a deeper insight in the H-bonding properties of the monitored molecules.

CONTENT

INTRODUCTION

The aim of this PhD work is to study the formation and the electronic and morphologic properties of complex organo-metallic and hetero-organic architectures, grown on metal surfaces via a bottom-up approach. In the recent years, these classes of systems have been deeply investigated and shown to be a valuable route to the design of new materials and to explore new chemical possibilities allowed by the two-dimensional (2D) confinement of reactants.[1] The possible fields that can take advantage from this quickly developing branch of research comprehends photovoltaics,[2] fuel cell,[3] biomaterials,[4] sensors[5] and molecular electronics.[6] In this view however, the understanding of fundamental properties like charge transport[7] and chemical reactivity[8] of these systems is mandatory to obtain their efficient use in prototypical devices.[9] Despite this importance, most of the papers on supramolecular assembly on surfaces present in literature are focused on the characterization of the morphology of the systems and the investigation of the electronic properties of complex organic systems is present in a limited number of works. In the present thesis, a combined morphologic and electronic study of some complex interfaces is presented. By means of x-ray spectroscopy techniques we have studied three distinct aspects related to these systems, in particular: the electronic properties in terms of charge transport, at the interface between electrodes and on-surface synthesized covalent molecular superstructures; the use of functional and active molecules to obtain specific chemical affinity of a surface; and the possibility to use a properly functionalized surface in controlled conditions as a reference model for catalytical processes.

Concerning the first point, we have focused our attention on molecular superstructures obtained via the on-surface condensation of boronic molecular precursors. Briefly, the condensation of boronic acids leads to the formation of the boroxine, a six-membered ring connecting three boronic functionalities. In surface science, boroxine has gained a preeminent role in the synthesis of 2D covalent organic frameworks (2D COFs). A COF is an organic crystalline porous material with atomically precise integration of building blocks into periodic two-dimensional (2D) structures.[10] The use that in literature is reported for these materials is of a template agent for surfaces, exploiting the favorable morphologic properties. The regularly distributed nanopores of the COF act as host for guest molecules of interest. In these complex guest-host architectures, the electronic properties of the COF-electrode interface are of fundamental importance, because they determine the charge transport between guest molecules and the substrate. In this context, we selected one of the most adopted class of COFs, the boroxine ones, and have focused the attention first on the electronic properties of the interface between the COF and the substrate. For that purpose, we have chosen to start our investigation with a prototype system, constituted by an on-surface synthesized boroxine molecular system that reproduce well the properties of an extended architecture. A multi-technique approach involving X-ray based spectroscopies, STM imaging and theoretical modeling allowed us to discover an interesting channel for ultra-fast electron delocalization between the boronic layer and the gold substrate. Once gained this information, we moved our focus on a novel extended system constituted on boron and oxygen atoms only. During this investigation we have also tackled an aspect that can be seen as one of the drawbacks of the boronic frameworks. In particular, a very low band dispersion has been foreseen for these materials, precluding an efficient charge transport in the in-plane direction.[11,12] We have demonstrated the presence of band dispersion in the material we have prepared. These two findings concerning the ultra-fast charge transport and the band dispersion respectively, give a deeper insight into the boroxine-based structures, going beyond the studies present in literature,

performed by STM and related mostly to the morphology of the systems.[13,14] The work on the boronic acid-based systems has been continued looking at them from a more chemical point of view. Indeed, the boron-containing product has also been investigated for its Lewis acid properties, that can be expressed if put in contact with a base. This approach has enabled us to anchor an amino-functionalized molecule over the boronic layer, synthesizing a complex architecture on the substrate. We have found an interesting evidence of a geometrical change in the boron environment induced by the presence of the amino molecule that can serve as a fingerprint of the reaction.

Referring to the list of the three distinct aspects we have challenged in this thesis, we have also studied the use of functional and active molecules to obtain specific chemical affinity of a surface. Aiming at this goal, we have employed for the first time in UHV environment a crown ether molecule to act as a trap for an alkaline metal. The crown ethers are a class of macrocyclic molecules known in wet chemistry for their ability in binding positively-charged ions. Moreover, they show a particular affinity toward alkali metals based on a shape matching.[15] These compounds have found an application in many fields, such as in analytical chemistry or in the mimicking of bioprocesses. We have monitored their properties in UHV environment. We have taken advantage of an ordered, crown ether-containing structure on the substrate surface to obtain a trapping of sodium proving that the macrocycle retains its affinity toward the alkaline metal even in UHV conditions. In particular, it has been demonstrated that the sodium is showing a higher affinity toward the crown ether with respect to a porphyrin macrocycle also present on the surface.

The last aspect of molecular assembly we have tackled concerns the use of the substrate surface as a simplified environment for elucidating chemical reactions. This approach can be employed in the study of catalysis in simplified conditions to make the understanding of the reaction mechanism easier,[16] even if the extrapolation of the results is not always straightforward.[17] We have adopted this strategy to study a model version of carbon nitride, a catalytic material for the photoinduced water splitting reaction.[18] It is interesting for its inexpensive and earth-abundant constituents. We have studied two molecules, the melem and the melamine, precursors in the synthesis of this polymeric catalyst, as models for the whole catalyst. We have focused our attention on the X-ray and UV spectroscopic characterization of the H-bonding with water molecules, since it is believed that this is the first step of the catalytic process.[19] We have achieved a spectroscopic characterization of the two systems, that can serve as a reference for future works.

The thesis is organized as follows:

Chapter 1 introduces the experimental techniques employed in this work and describes the experimental setup that has been used. It is not intended to be an exhaustive theoretical and practical description, but a concise overview on the different experimental methods. More space is dedicated to the ALOISA beamline with its ANCHOR end station where the majority of the spectroscopic data have been collected, but also the Surface Physics Laboratory and the OSMOS laboratory are described.

In Chapter 2 the boroxine related systems are presented, with in particular the study of their electronic properties.

Chapter 3 presents the experiment performed on the precursors of the carbon nitride.

In Chapter 4 two more complex systems are reported. We have studied the interaction between the boroxine ring and an amino terminated molecule.

Part of the thesis has already been published in the following papers:

1) **On-surface synthesis of a 2D boroxine framework: a route to a novel 2D material?**, Matus Stredansky, Alessandro Sala, Tommaso Fontanot, Roberto Costantini, Cristina Africh, Giovanni Comelli, Luca Floreano, Alberto Morgante and Albano Cossaro, Chem. Commun., 2018, 54, 3971-3973, DOI: 10.1039/C8CC01372A

2) **ANCHOR-SUNDYN: a novel endstation for time resolved spectroscopy at the ALOISA beamline,** R. Costantini, Matus Stredansky, D. Cvetko, G. Kladnik, A. Verdini P. Sigalotti, F. Cilento, F. Salvador, A. De Luisa, D. Benedetti, L. Floreano, A. Morgante, A. Cossaro, M. Dell'Angela, Journal of Electron Spectroscopy and Related Phenomena 229 (2018) 7–12

3) **Spectroscopic fingerprints of intermolecular H-bonding interactions in carbon nitride model compounds**, Valeria Lanzilotto, Jose Luis Silva, Teng Zhang, Matuš Stredansky, Cesare Grazioli, Konstantin Simonov, Erika Giangrisostomi, Ruslan Ovsyannikov, Monica de Simone, Marcello Coreno, Carlos Moyses Araujo, Barbara Brena and Carla Puglia, *Chem. Eur. J. 10.1002/chem.201802435*

4) **Electronic properties of the boroxine–gold interface: evidence of ultra-fast charge delocalization,** Daniele Toffoli, Matus Stredansky, Zhijing Feng, Gabriele Balducci, Sara Furlan, Mauro Stener, Hande Ustunel, Dean Cvetko, Gregor Kladnik, Alberto Morgante, Alberto Verdini, Carlo Dri, Giovanni Comelli, Giovanna Fronzoni and Albano Cossaro, *Chem. Sci., 2017, 8, 3789-3798,* doi: 10.1039/C6SC05632F

BIBLIOGRAPHY:

1. Lindner, R. & Kühnle, A. On-Surface Reactions. *ChemPhysChem* **16,** 1582–1592 (2015).

2. Vilan, A. *et al.* Molecules on Si: Electronics with Chemistry. *Adv. Mater.* **22,** 140–159 (2010).

3. Willner, I. Biomaterials for Sensors, Fuel Cells, and Circuitry. *Science (80-.).* **298,** 2407 LP-2408 (2002).

4. Prime, K. L. & Whitesides, G. M. Adsorption of proteins onto surfaces containing end-attached oligo(ethylene oxide): a model system using self-assembled monolayers. *J. Am. Chem. Soc.* **115,** 10714–10721 (1993).

5. Gooding, J. J. Advances in Interfacial Design for Electrochemical Biosensors and Sensors: Aryl Diazonium Salts for Modifying Carbon and Metal Electrodes. *Electroanalysis* **20,** 573–582 (2008).

6. McCreery*, R. L. Molecular Electronic Junctions. (2004). doi:10.1021/CM049517Q

7. David M. Adams, † *et al.* Charge Transfer on the Nanoscale: Current Status. (2003). doi:10.1021/JP0268462

8. Chechik, V., Crooks, R. M. & Stirling, C. J. M. Reactions and Reactivity in Self-Assembled Monolayers. *Adv. Mater.* **12,** 1161–1171 (2000).

9. Ulman, A. Formation and Structure of Self-Assembled Monolayers. *Chem. Rev.* **96,** 1533–1554 (1996).

10. Xu, S.-Q., Zhan, T.-G., Wen, Q., Pang, Z.-F. & Zhao, X. Diversity of Covalent Organic Frameworks (COFs): A 2D COF Containing Two Kinds of Triangular Micropores of Different Sizes. *ACS Macro Lett.* **5,** 99–102 (2016).

11. Wang, R.-N., Zhang, X., Wang, S.-F., Fu, G. & Wang, J. Flatbands in 2D boroxine-linked covalent organic frameworks. *Phys. Chem. Chem. Phys.* **18,** 1258–1264 (2016).

12. Gutzler, R. Band-structure engineering in conjugated 2D polymers. *Phys. Chem. Chem. Phys.* **18,** 29092–29100 (2016).

13. Dienstmaier, J. F. *et al.* Synthesis of well-ordered COF monolayers: Surface growth of nanocrystalline precursors versus direct on-surface polycondensation. *ACS Nano* **5,** 9737–9745 (2011).

14. Dienstmaier, J. F. *et al.* Isoreticular two-dimensional covalent organic frameworks synthesized by on-surface condensation of diboronic acids. *ACS Nano* **6,** 7234–7242 (2012).

15. Gokel, G. W., Leevy, W. M. & Weber, M. E. Crown ethers: Sensors for ions and molecular scaffolds for materials and biological models. *Chem. Rev.* **104,** 2723–2750 (2004).

16. Musselwhite, N. & Somorjai, G. A. Investigations of Structure Sensitivity in Heterogeneous Catalysis: From Single Crystals to Monodisperse Nanoparticles. *Top. Catal.* **56,** 1277–1283 (2013).

17. Bridging the pressure and material gap in heterogeneous catalysis. *Phys. Chem. Chem. Phys.* **9,** 3459 (2007).

18. Wang, X. *et al.* A metal-free polymeric photocatalyst for hydrogen production from water under

visible light. *Nat. Mater.* **8,** 76–80 (2009).

19.   Ehrmaier, J., Karsili, T. N. V., Sobolewski, A. L. & Domcke, W. Mechanism of Photocatalytic Water Splitting with Graphitic Carbon Nitride: Photochemistry of the Heptazine–Water Complex. *J. Phys. Chem. A* **121,** 4754–4764 (2017).

CHAPTER 1: EXPERIMENTAL TECHNIQUES AND LABORATORIES

During this PhD work different experimental techniques have been exploited accordingly to preparation and characterization needs. An important part of the characterization has been performed by photoelectron spectroscopies that are described below. These analytical methods enable a deep investigation of the sample at the important drawback of requesting ultra high vacuum (UHV) environment to allow the electrons to have a mean free path sufficient to reach the detector. This important aspect has to be taken in account during the choice and preparation of the samples. Even if this constrain may appear somehow restricting the field of applicability of the photoelectron spectroscopies, the scientific interest explored in this doctoral work lies in 2D systems and their interaction with metallic supporting surfaces. In such a field, the fine control combined by the reduction of unwanted interactions is welcome, so the ultra high vacuum limits the presence of contaminant species on a system, enabling the possibility to study the behavior of pure substances on a substrate without the interference of solvent or air particles. In addition to the spectroscopic data, the Scanning Tunneling Microscopy imaging technique has been used. The information retrieved has furnished a complementary view of the studied systems. From a practical point of view, this multi-technique approach has been achieved performing experiments in different apparatuses. The principal experimental setups are described after the introduction of the techniques.

1.1 X-RAY SPECTROSCOPIES

In the present thesis the X-ray spectroscopies have been the major investigation tool. This section describes employed techniques, starting from the X-ray photoelectron spectroscopy (XPS); then ultraviolet photoelectron spectroscopy (UPS) and near edge X-ray fine structure (NEXAFS) are introduced. A less commonly used technique, resonant photoemission spectroscopy is also presented. This brief summary of the techniques is not intended as a complete derivation, but as an introduction to the relevant aspect of the techniques with respect to the aims of this work. After this disquisition on the methodologies, an overview on the principal experimental setups is laid. Many efforts have been spent working on the ALOISA beamline of the ELETTRA synchrotron in Italy, so there is a brief description of the facility followed by the description of the ALOISA beamline. Moreover, data have been collected also in other laboratories, such as the Surface Physics Laboratory at the Uppsala university in Sweden. In addition, a limited number of experiments have been carried out also at the GasPhase beamline of the ELETTRA synchrotron and at the PM4 beamline of the BESSY II synchrotron facility in Berlin, Germany that are not described.

1.1A X-RAY PHOTOELECTRON SPECTROSCOPY

X-ray photoelectron spectroscopy (XPS) is an analytical technique able to retrieve relevant information from the matter, such as chemical composition and chemical state of the elements of a sample. From the historical point of view, the photoelectric effect, the base of XPS (as well as of ultraviolet photoemission spectroscopy), was discovered by Hertz in 1887[1] and explained in 1905 by Einstein invoking the quantum nature of light.[2] Photoemission takes place when the light used to probe the sample carries enough energy to promote electrons into the vacuum. The electrons move then with a certain kinetic energy which can be calculated from the basic equation governing this effect:

$$E_{kin} = h\nu - E_{bin} - \phi$$

where E_{kin} is the kinetic energy of the outcoming electrons, h is the Planck constant, ν is the frequency of the light, E_{bin} is the binding energy of the electron in the sample and ϕ stands for the work function of the material, which measures the minimal energy necessary for promoting one electron from the sample to the vacuum. Usually an XPS spectrum is reported by plotting the measured intensity as a function of the binding energy, making thus the scale independent from the particular photon energy used during the acquisition. For solids there is the convention to put the zero at the Fermi energy, while a gas phase experiment would have the zero of the energy scale set at the vacuum energy. One of the simplest models that are usually employed to explain the XPS is the three-step model.[3] In the first stage the photon is absorbed by an atom of the material, the photo-excited electron and the ion are formed. During the second stage, the excited electron travels to the surface, and finally in the third step the electron escapes in the vacuum. The XPS, thanks to the high energy of X-ray photons, permits to explore the binding
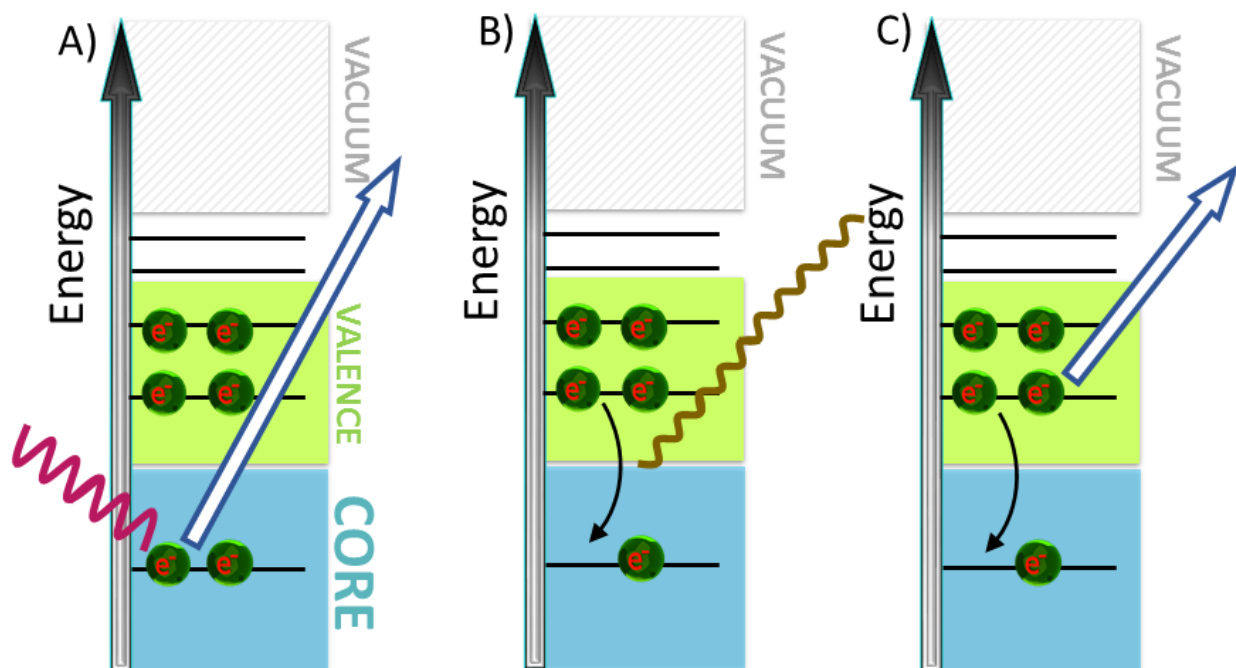

Figure 1: Schematic representation of XPS, A) interaction with X-rays can eject one electron of a core level into the vacuum. The gap between the valence (green) and vacuum (grey) is the work function of the material. B) fluorescent decay of the core-hole, C) Auger decay of the core-hole

energies of the tightly bonded electrons of the matter, the core levels. This implies that after the emission of the photoelectron the system is in a core-hole excited state. The decay process involves an electron occupying a higher energy state that fills the core hole, leaving a shallower hole. This decay can follow a radiative path whit emission of fluorescent light, or a non-radiative path with emission of a third electron, called Auger electron. The process is reported in figure 1 with also the decay paths of such an excited state. These electronic levels are element specific allowing the composition analysis of the sample. The XPS allows retrieving information about the stoichiometry of a sample by comparison of intensities of signals of different elements. The abundance of different elements can be correlated to the intensity of the photo-emitted peaks through their cross-section σ. This factor takes into account the probability of the transition upon illumination at certain wavelength. Following Hüfner[3], σ can be defined as:

$$\sigma = \frac{P_{if}}{F}$$

where P_{if} is the probability of transition and F is the photon flux per unit of time and area. The probability term can be calculated through the Fermi golden rule, with the dipole approximation, and introducing the dipole operator, leading to:

$$P_{if} \propto |\langle f|\boldsymbol{e}\cdot\boldsymbol{\mu}|i\rangle|^2$$

where **e** is the polarization unit vector and **μ** is the dipole operator (**μ**=e**r**). At this point another approximation can be employed to evaluate the initial and final wavefunctions. In particular, in a one electron view of the wavefunctions, they can be rewritten as product of functions of single electron, with quantum number k, that is being emitted (ϕ_k) and all the others ($\Psi^k_{Remaining}$ (N - 1)). The probability of transition becomes:

$$P_{if} = \langle \phi_{f,E_{kin}}|\mu|\phi_{i,k}\rangle\langle\Psi^k_{f,Remaining}(N-1)|\Psi^k_{i,Remaining}(N-1)\rangle$$

The function of the remaining electrons may be approximated as equal before and after the excitation (frozen orbital approximation) leading to one electron transition matrix elements. Another important aspect that has to be taken in mind is that while the penetrating power of photons in the soft x-ray region is in the order of micrometers[4], the volume of the sample which is actually producing the detectable signal is limited by the electron interaction with matter to some nanometers from the surface. This interaction can result in an energy loss, and the electrons that during their path in the material undergo these inelastic interactions, but have still enough energy to leave the sample, contribute to the background of secondary electrons. To quantify this phenomenon, it has to be considered that an electron flux (I) passing through a layer decays following Lambert-Beer law[5]:

$$I = I_0 e^{-\frac{d}{\lambda cos\alpha}}$$

where I_0 is the flux before attenuation, d is the thickness of the layer, α is the angle of emission measured from the surface normal, and λ is the inelastic mean free path (IMFP). This last quantity represents the thickness of a layer that reduces the flux to 1/e of its non-attenuated value. It can be calculated by the semi-empirical equation of Seah and Cumpson[6]:

$$\lambda = 0.316a^2 \left\{ \frac{E}{Z^{0.45} \left[ln\left(\frac{E}{27}\right) + 3 \right]} + 4 \right\}$$

which gives the resulting IMFP in nanometers, with a the lattice parameter, E the kinetic energy of electrons in eV and Z the mean atomic number of the compound. This aspect is very important in determining the portion of the sample from which the signal is acquired and makes XPS a surface sensitive technique. Moreover, the outgoing photoelectrons can also undergo a defined interaction with a valence electron, leaving the ion in an excited state upon transferring part of their kinetic energy. This event causes the appearing of a satellite peak in the spectrum. This satellite results to be a well-defined peak when the
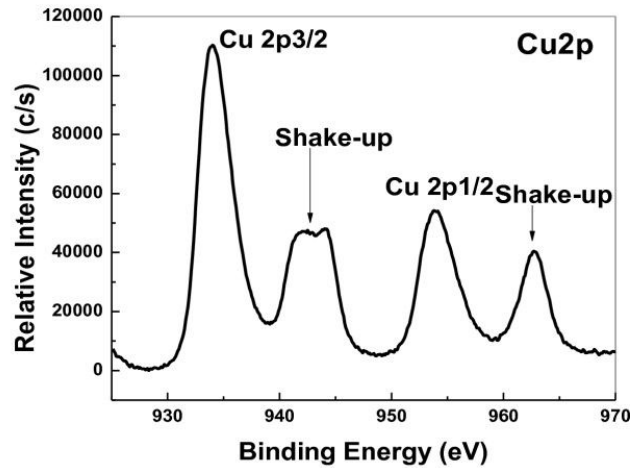
Figure 2: example of shake-up peaks in the XPS of copper taken during the study of CuO nanowires. Image adapted from Ethiraj and Kang[7]

valence band electron is promoted to a bound state (*shake-up* peak), whereas has more broad and undefined shape if the valence electron is promoted in the continuum of states beyond the vacuum level (*shake off)*. An example of a shake-up structure found in literature[7] is shown in figure 2.

 The dependence of the IMFP on E plays a crucial role also in the stoichiometry determination in the case of thick overlayers, where the intensity of the signal of the present elements is not only affected by abundance and cross-sections but also by the volume of sample contributing to the signal. In order to evaluate how the decrease affects the signal of different electrons, it is necessary to calculate the thickness of the layer. For this purpose, the intensity of the signal of a substrate peak is acquired with and without the overlayer. Knowing the thickness, for the evaluation of the stoichiometry of a film the intensity is rewritten for an emitting layer of thickness d:

$$I = I_0 \int_0^d e^{-\frac{x}{\lambda}} \, dx$$

which leads to:

$$I = I_0 \left(\lambda - \lambda e^{-\frac{d}{\lambda}} \right)$$

For a rather thick layer the exponential term becomes very small and only the IMFP can be considered. This implies that for two elements A and B another factor λ_A/λ_B must be taken into account to correct the relative intensities. In addition to the determination of the elements present in a sample and their stoichiometry, XPS allows also to investigate in the chemical state thanks to the *chemical shift* that the binding energies of core electrons present when the atoms they belong to are involved in different chemical environments. This shift can be due to initial and final state effects. The first are the most interesting in this work and reflect the state and the chemical environment in which an atom is found. Final state effects reflect the situation after the emission, such as relaxation of the electronic levels, polarization of the surrounding ions or core-hole screening.[5,8] This means that, in addition to the characterization of the stoichiometry of thin and thick films, it is also possible to investigate the differences between the monolayer and the multilayer coverage. In the multilayer, the signal is due to the molecules that are not interacting directly with the surface and it is often assumed, especially if it is a molecule known for congruent evaporation or sublimation, that they have not undergone any chemical change. By contrast, the monolayer is composed only by molecules interacting directly with the substrate, and its catalytic properties may have produced chemical reaction in the molecular film. In this perspective, not only the stoichiometry of the two coverages is important, but also the differences in chemical shifts of the XPS peak reflecting the novel situation. Unfortunately, a direct comparison of the binding energies of the peaks is not possible if the substrate is a metal because of the screening effect that is naturally shifting the peaks. This final state effect on the chemical shift can be explained by induction of an image charge in the metal by the photoionized atom that is emitting. While the hole positively charged is attracting the ejected electron, the image charge, negative, is repelling the electron by applying a screening on the hole. Since this effect is very sensitive to the distance between the hole and the surface, at the monolayer the screening effect is remarkable, whereas in the multilayer coverage the surface is distant, so the image charge interaction is weak leading to low or no screening. The image charge moves the position of peaks of the multilayer to higher binding energies with respect to the monolayer. To disentangle this natural shift from other changes in chemical shift due to a different initial state, it is possible in some cases to monitor the behavior of an element that is supposed to not participate to any reaction, so is unlikely to have some important changes in chemical shift except for the mirror charge effect and, since the screening effect can be supposed to be equal for every element present in the monolayer coverage (at least if the deposition geometry is flat), the measured shift of non-reacting atoms can be subtracted from the interacting ones, allowing to retrieve the residual chemical shifts.

1.1B Ultraviolet Photoelectron Spectroscopy

Ultraviolet photoelectron spectroscopy (UPS) is another valuable tool for the analysis of a sample. As XPS, it is based on the photoelectric effect but, instead of probing the strongly bound core electrons, UPS employs less energetic radiation to explore the valence band of a specimen, as depicted in figure 3 A). In the case of a metallic sample, the bands that lying higher in energy are studied. For molecules in gas phase or adsorbed on a substrate, this technique allows to access to the molecular orbitals not far from the vacuum level. It is possible to study the valence band even with more energetic photons, X-rays for instance, but it is more convenient to employ ultraviolet light because the cross-sections tend to decrease

when there is a large difference between the photon energy and the binding energy of the emitted electron. For this reason, UV sources, such as gas discharge lamps, are adopted. The discharge lamp produces well defined spectral lines applying a high voltage on a low-pressure gas, usually a noble one. Each gas has it specific emission lines and employing high purity gases enhances the monochromaticity. It is also possible to use a monochromator even if it causes a drop in the photon flux. The most commonly used gas is helium, which produces intense emission lines at 21.216 eV (584.334 Å)[9] called He I α and at 40.81 eV called He II α. There are also other lines at lower intensities, like He I β (23.087 eV)[10] or He II β (48.37 eV) which complicate the spectra taken without a monochromator. In addition to the monitoring of the valence band, the UPS is able also to provide an insight into the band structure of a material. Bearing in mind that the electronic states of a crystalline solid are described in term of bands with energy depending on wave vector **k**, retrieving information about the band structure becomes a very important issue in order to characterize a material. For a better understanding of this technique, it is possible to invoke the three-step model. The first step is represented by the absorption of the photon and the optical transition between two bands with the final state above the vacuum energy. The internal energy distribution N is given, neglecting the momentum of the incoming photon, following Hüfner[3]:
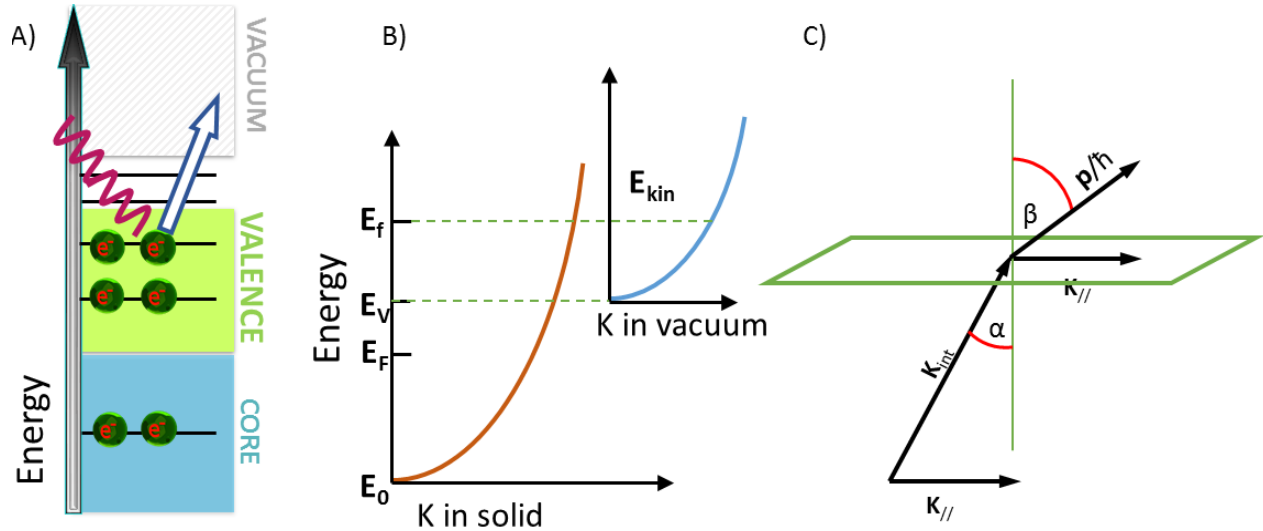

Figure 3: Schematic representation of UPS, A) the photoemission process, B) dispersion of electrons in the solid on the left and in the vacuum on the right with scale adjusted to match between the two cases. C) The scheme of momentum conservation during the third strep of the three-step model. The $K_{//}$ is conserved while the perpendicular component does not.

$$N(h\nu, E) \propto \sum_{i,f} \left\langle i, \boldsymbol{k}_i \left| \frac{e}{mc} \boldsymbol{A} \cdot \boldsymbol{p} \right| f. \boldsymbol{k}_f \right\rangle^2 \delta(E_f(\boldsymbol{k}_f) - E_i(\boldsymbol{k}_i) - h\nu)\, \delta(\boldsymbol{k}_f - \boldsymbol{k}_i - \boldsymbol{G})\, \delta(E - [E_f(\boldsymbol{k}_f) - \phi])$$

where |i,k_i> and |i,k_f> represent the initial and final band with energies of $E_i(\boldsymbol{k}_i)$ and $E_f(\boldsymbol{k}_f)$ respectively, the interaction operator neglects the non-linear process being **A** the vector potential and **p** is the momentum operator. The first delta function ensures the energy conservation, the second takes care of the momentum conservation while the last one points out that the kinetic energy measured outside the sample must be equal to the initial energy plus the work function.

During the second step of this model, the electrons travels toward the surface. The main cause that is preventing photoelectrons from reaching the surface, is the electron-electron interaction. Introducing the scattering frequency τ, the inelastic mean free path can be viewed as:

$$\lambda(E, k) = \tau v_g = \frac{2\tau\pi}{h}\frac{dE}{dk}$$

with v_g the group velocity in the final state.

Once the electron has reached the surface, there is the last step, the escape into the vacuum. For a better insight, it is possible to invoke the escape-cone argument. It has to be taken in mind that only electrons with the component of kinetic energy perpendicular to the surface sufficient to overcome the surface potential barrier will be able to escape, see also figure 3 panel B) for energy scales. Written in equation this request becomes:

$$\frac{\hbar^2}{2m} K_\perp^2 \geq E_v - E_0$$

where $K_\perp$ is the component of the wave vector perpendicular to the surface, E_0 is the bottom of the valence band and E_v is the level of vacuum. The transmission of the excited photoelectron leaves unchanged the component of its wave vector parallel to the surface, $K_{//}$. Thus, in a free electron model, it is possible to retrieve a Snell law for the electrons:

$$K_{//} = \sin\beta \left(\frac{2m}{\hbar^2}E_{kin}\right)^{\frac{1}{2}} = \sin\alpha \left[\frac{2m}{\hbar^2}(E_f - E_0)\right]^{\frac{1}{2}}$$

with β the external angle between the wavevector and the surface normal and α the internal one, as reported in the figure 3 C). This implies that there is a critical angle α_{cri} which defines a cone from which electrons can escape.

$$\sin\alpha_{cri} = \left(\frac{E_{kin}}{E_f - E_0}\right)^{\frac{1}{2}}$$

E_{kin} is the kinetic energy outside the solid. It can be viewed as:

$$E_{kin} = \frac{\hbar^2}{2\pi m}\left[K_{//}^2 + \left(\frac{p_\perp}{\hbar}\right)^2\right] = E_f - E_v$$

where $p_\perp$ is the component perpendicular to the surface of the momentum of the electron outside of the solid, and the last term states that the energy of the electron outside is equal to the energy of the final band inside the solid minus the vacuum energy. For a better understanding of the energy levels, it is possible to refer to figure 3 B). The component of the momentum perpendicular to the surface is not conserved for solid. Retrieving also this information is not trivial, unless when working with 2D materials where only $K_{//}$ matters, which are the scientific cases of this thesis. The dispersion in angle then can be converted in dispersion in reciprocal space considering that measuring kinetic energy of electrons is measured in eV:

$$K_{//} = \sin\beta \left(\frac{2\pi m}{\hbar^2}E_{kin}\right)^{\frac{1}{2}} = 0.512 \sqrt[2]{E_{kin}} \sin\beta$$
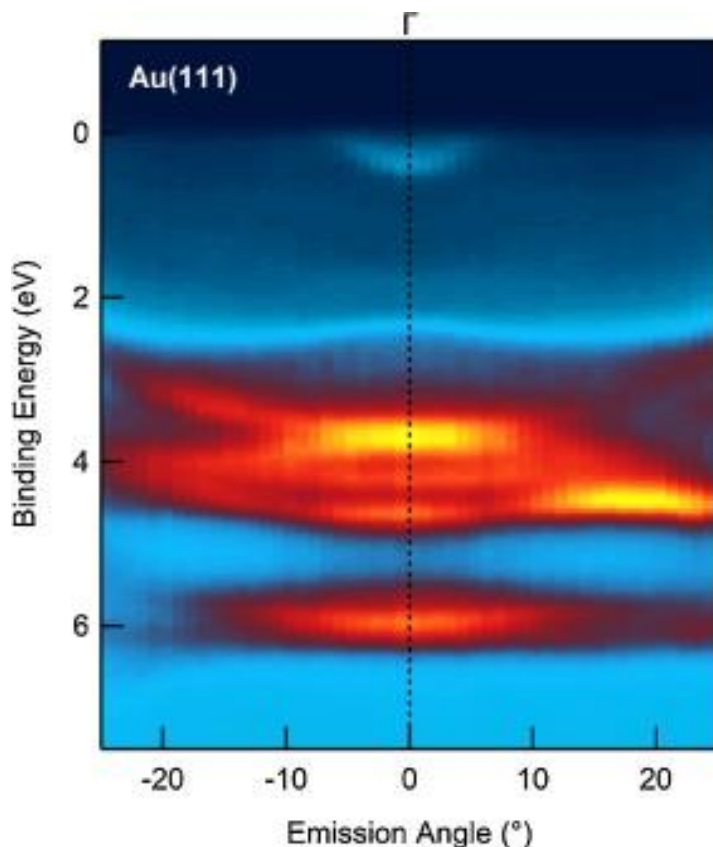
Figure 4: ARUPS map of clean gold surface. Acquired with a non-monochromatized He lamp employing the He(II) spectral line. The pass energy of the electron analyzer was set to 10 eV. The map has been normalized to the region around 7 eV to have all the spectra at the same intensity in this featureless region. A similar procedure has been adopted for all the ARUPS maps shown in the thesis.

The band structure of a solid often deviates significantly from the ideal free electron model. For instance, figure 4 reports the band structure of the gold.

1.1C Near Edge X-ray Absorption Fine Structure

Near Edge X-ray Absorption Fine Structure (NEXAFS) is another spectroscopic technique which employs light to promote electronic transitions and explores the unoccupied states of molecules and materials. When applied to molecular systems, the technique allows obtaining information about the unoccupied levels energy distribution as well as about the orientation of the molecular orbitals with respect to the surface, i.e. about the molecular adsorption geometry. In a NEXAFS measurement, the energy of photons is varied across a photoemission threshold of an element. The absorption of photons exhibits a peak in correspondence of a core-empty state transition, as represented in figure 5A). From a theoretical point

view, it is possible to start again with the Fermi golden rule that states that the transition probability P is equal to[11]:

$$P_{if} = \frac{2\pi}{\hbar}\,|\langle f|O|i\rangle|^2 \rho(E)$$

where |i> and |f> denote the wavefunctions of the initial and final states respectively, ρ(E) is the density of final states, O is the transition operator. The approximations made for the XPS are no longer valid, even if the NEXAFS signal still reflects the unoccupied molecular density of states weighted by the dipole transition matrix:

$$D_{if} = \int \Psi_f^* \, \boldsymbol{\mu} \, \Psi_i \, d\boldsymbol{r}$$

To estimate these matrix elements, it is useful to make use of group theory. In particular the product inside the integral can be discussed in terms of parity of the factors. If it is antisymmetric, then at least along one axis the integral is zero meaning that the transition is forbidden. Then for the estimation of the possibility of a transition, the parity of each term must be known. For instance, in an experiment with the K-edge of low Z elements, as B, C, N, O, the initial state |i> is to a good approximation the 1s atomic orbital, symmetric to any plane. The symmetry of the operator is determined by the polarization of the light, and employing linearly polarized light, the direction along which the photons are antisymmetric is determined by the polarization vector. The final orbital is a molecular unoccupied orbital, which is usually, with respect to the plane of the bonded atoms, of σ* or π* type. To justify this statement, it is worth noticing that in a one-electron view using the LCAO approximation (Linear Combination of Atomic Orbitals) each molecular orbital can be expanded in a base of the atomic orbitals and the final state can be approximated with one unoccupied molecular orbital of the initial state, with its symmetry. Moreover, the molecular orbitals
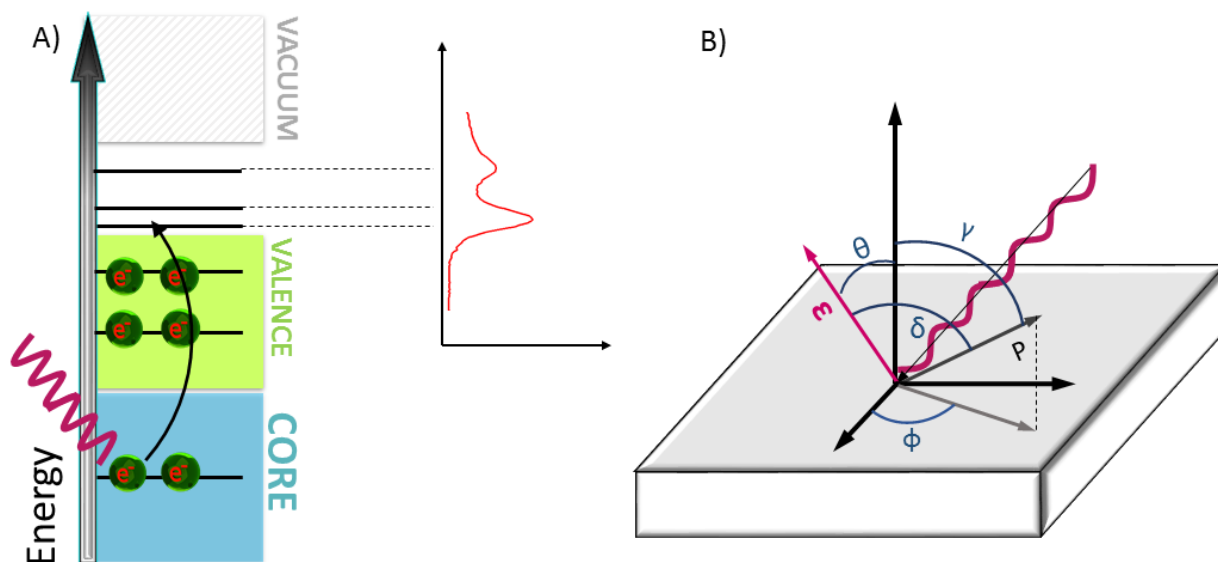

Figure 5: A) Schematic representation of NEXAFS spectroscopy. The sample is probed by X-rays of tunable energy and for certain values a promotion of an electron from a core orbital to an unoccupied one is possible. The spectrum is measured acquiring the intensity of the signal in function of the incoming photon energy. B) The angles in the text refers to the depicted scheme of illumination of the sample.

(MO) can be highly directional. In particular, in the unoccupied region the antibonding orbitals are

present, like σ* that has a spatial distribution along bonds and the π* which has a distribution orthogonal to the bond, having opposite symmetry compared to the previous one. This consideration leads also to understand another possibility of the NEXAFS spectroscopy. In the case of adsorbed molecules on a surface, it is possible to gain information about the geometry of adsorption exploiting the transition intensity dependence on the orientation of the polarization vector with respect to the molecular orbitals. The initial state is determined by the edge that is probed, in the simplest case it is a K-edge, for which, following the treatment of Stohr[11], it is possible to retrieve that the intensities of transitions to orbitals depend on the symmetry:

$$I(\sigma^*) \propto cos^2\delta \qquad\qquad I(\pi^*) \propto sin^2\delta$$

For the angles, refer to figure 5 B), and δ is the angle between the polarization vector of the light and the molecular orbital direction. Discussing the adsorption geometry, it is more useful to work in coordinates fixed to the substrate rather than on the molecule, so the intensity can be expressed as:

$$I \propto 1 - [\cos(\theta) cos(\gamma) + \sin(\theta) \sin(\gamma) \cos(\varphi)]^2$$

using the angles as defined in figure. In the case of twofold or higher symmetry, the cross-term containing the cos(φ) is eliminated upon averaging over domains, leading to simplification:

$$I \propto 1 - cos^2(\theta)cos^2(\gamma) - sin^2(\theta)sin^2(\gamma)cos^2(\varphi)$$

Interestingly, the dependency on γ of the above formula, vanishes for a certain value of the polarization angle θ. At this angle, θ$_{magic}$, the orientation of the molecules does not influence the absorption intensity. In particular, for a highly symmetric surface, threefold or manifold, it is possible to simplify the expression considering that there is no dependency on the azimuthal angle, i.e. $\langle cos^2(\varphi) \rangle = 1/2$:

$$I \propto 1 - cos^2(\theta)cos^2(\gamma) - \frac{1}{2}sin^2(\theta)sin^2(\gamma) = 1 - cos^2(\theta)\left[cos^2(\gamma) + \frac{1}{2}sin^2(\gamma)tan^2(\theta)\right]$$

From the last term it is clear that for vanishing the dependency on γ:

$$\tan(\theta) = \sqrt{2} \quad \rightarrow \quad \theta = \arctan(\sqrt{2}) \propto 54.7°$$

For the determination of geometry, it is necessary to measure NEXAFS spectra at two different angles of the polarization vector with respect to the surface, further simply addressed "polarization angle" or "polarization". On a threefold or higher symmetry surface, the two polarizations are obtained with the electric field of the radiation parallel or perpendicular to the substrate surface. In principle, a reliable theoretical calculation is requested for a correct attribution of measured peaks to MO with known geometry, but for many organic molecules it is also possible to compare the spectra with the ones obtained with known systems. For instance, molecules with aromatic rings or conjugated double bonds, are expected to show transitions to both σ* and π* empty orbitals which have opposite symmetry, and the π* unoccupied orbital lies lower in energy. The dependence of the probability of a transition on the mutual orientation between the orbital and the polarization vector can lead to dichroism between spectra taken at s and p-polarizations. If the geometry of the orbital is already known, this effect gives clues about orientation of the molecule with respect to the surface. The NEXAFS signal can be detected in different ways: with a photon detector, measuring the radiative decay of the excited system (fluorescence yield); with an electron analyzer, measuring the intensity of the Auger decay related to the observed transition (Auger yield);by measuring the drain current between ground and sample at each photon energy, that

compensate the charge emitted due to the absorption processes with a channeltron detecting the electrons emitted from the sample (total yield). The use of a particular detecting method depends on the studied systems. Fluorescence yield is preferred when dealing with high atomic number edges, for which the fluorescence decay is most probable; drain current is the most bulk sensitive method; electron-detection methods are more surface sensitive and therefore particularly suited for surface science studies.

1.1D RESONANT PHOTOEMISSION SPECTROSCOPY

Resonant Photoemission spectroscopy (RESPES) has been employed in this work to characterize the electronic dynamics at organo-metallic interface. As for NEXAFS, in RESPES the photon energy is varied across an absorption edge. For each photon value, the valence band photoemission spectrum is measured. In addition to the direct photoemission signal, the electrons due to the de-excitation processes are detected under these conditions. In fact, the de-excitation can follow different paths, the radiative one, with emission of a fluorescent photon, figure 6 D), or via the Auger non-radiative path. For elements with low Z, which are of interest in this work, the Auger decay prevails.[12] The Auger process may have two de-excitation paths, with different final states. When the core-hole is filled by an electron from an occupied state higher in energy, the second electron, that is gaining the energy and is getting ejected, can come from the higher occupied state, the one populated by the initial transition by the probing radiation (participator decay or Raman Auger, refer to figure 6 F), or can occupy another level (spectator decay) figure 6 E). The first path leaves the system with a shallow hole in the valence and is energetically degenerate with direct photoemission from the valence band (UPS). By contrast, the spectator decay leaves the system with two holes in the valence and one electron in a level that was unoccupied in the initial state of the system. The presence of this electron causes the *spectator shift*: the kinetic energy
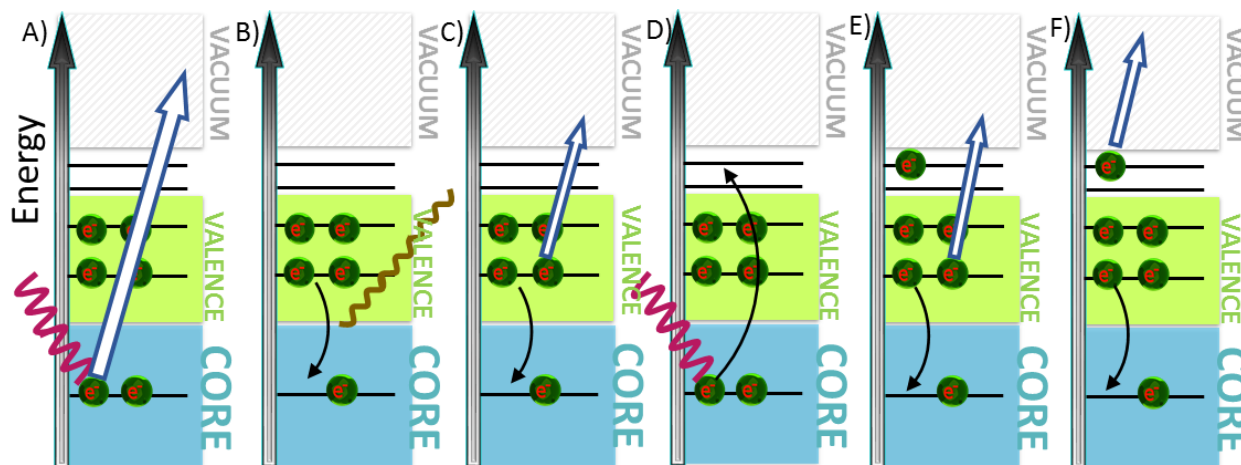

Figure 6: A) direct photoemission from a core level (XPS). B) decay of the core-hole excited system created in A via fluorescence, C) decay of the core-hole excited system created in A via Auger photoemission. D) promotion of an electron from a core level to an unoccupied orbital (like NEXAFS excitation). The created system has a core-hole and can non-radioactively decay via spectator decay E) or participator decay

spectrum of the electrons emitted in the spectator decay is very similar to the Auger spectrum but with

the lines shifted to higher energies. This uniform effect can be explained by the screening effect of the spectator electron on the holes, lowering the energy necessary to their creation, and thus allowing the Auger electron to leave the system with higher energy.[12,13] The RESPES measures the electrons emitted during the de-excitation process. For this purpose, it is necessary to acquire, for each incoming photon energy, the whole photoemission spectrum in the valence region. In principle, by integrating all the signal acquired at single photon energy, the corresponding point in the NEXAFS spectrum should be obtained. It is also important to stress out that the spectator decay channel is found at constant kinetic energy, whereas the participator (Raman Auger), since degenerate energetically with direct photoemission, can be found at constant binding energy. A theoretical treatment can be found in references.[13,14] Among the most relevant points of this spectroscopic technique is the enhancing of particular peaks of the valence spectrum: the enhancement can occur only for orbitals in proximity of the probed atom (the atoms of the element whose edge is probed).[15,16] Such an effect is due to the localized nature of the Auger process and core-hole wavefunction. Even if the wavefunction of the unoccupied orbital, that as a first approximation is assumed to be the final state of the excited electron, is often delocalized on the whole molecule, the interaction of the electron with the hole localizes the exciton near the core-hole formation site. This can be used for the detection of the participation to a molecular orbital of an element by tuning the X-rays across its photoemission edge. It is particularly important to detect the presence of less intense peaks of the studied system that lie at energies where there is a strong substrate contribution to the signal. Another important application of the RESPES is the possibility of studying ultra-fast charge delocalization that happens during the lifetime of the excited state, in a method that is named core-hole clock.[17] In particular, if we have a system that has undergone the transition from a core state to an unoccupied molecular orbital, it is possible in certain cases to transfer the electron from his new orbital to another system. In the case of molecules or a 2D material on a substrate, there can be a charge transfer between the two parts, and this can happen in both directions, from the overlayer to the substrate or vice versa. This application of the technique takes advantage of the short lifetime typical for systems with a core-hole. The typical lifetime of the core-hole for light elements is of the order of few femtoseconds.[18] For the purposes of this thesis, the RESPES has been used to investigate the possibility of an electron transfer between the layer formed on the surface and the gold substrate beneath. It is important to stress that for an exact quantification of the charge transfer time it is necessary to make a comparison with an isolated system, for example in the case of a molecule it would be necessary to compare the RESPES of the molecule on the surface and in the gas phase, where it can be supposed that there is no charge transfer. This is not possible in the case of a covalent framework, for which there is no gas phase corresponding system. We have dealt with such a case when working on boronic frameworks. In this case it is possible to make an estimation of the timescale involved in the transfer comparing the valence band corresponding to the excitation on the molecular orbital that is supposed to transfer, and the valence band acquired above the edge where decay happens through normal Auger process. Unfortunately, this implies that for our case only an estimation of the time scale involved in the charge transfer is available.

1.1E ALOISA Beamline at ELETTRA

The major part of the spectroscopic data of this doctoral work has been acquired at ALOISA beamline (Advanced Line for Over-layer, Interface and Surface Analysis) figure 7 of the ELETTRA synchrotron facility. ELETTRA is a third-generation light source. Differently from previous generation synchrotrons, the facility is composed by a "ring" formed by straight sections connected by curved parts. At ELETTRA the storage ring electron energy is of 2.0 or 2.4 GeV and machine works in top-up mode with frequent injections of small values to keep the current constant. To produce the synchrotron light, there are two types of devices, namely bending magnets and insertion devices, so named for their position inside of the ring. The bending magnets are present at any curved part connecting the ring straight sections. The undulators and wigglers are placed in the straight sections. They are composed by two facing arrays of magnets with alternating polarity which imposes to the electrons a curved trajectory. While the wiggler applies a stronger magnetic field that is able to deviate substantially the electron trajectory, the undulator employs a weaker field and the path of the electrons is only slightly affected experiencing a harmonic oscillation. One of the advantages of the wiggler and ondulator over the bending magnet is the tunability of the field, which changes the spectrum of the emitted radiation. In correspondence to every insertion device, there is a beamline, a structure where the light is employed for experiments. During this PhD work, ALOISA beamline changed its insertion device. For the first period an ondulator with magnets in an array of 19 periods of 80.36 mm (for a total length of 1527 mm) was used. The photons produced by this device range from 130 eV to 8000 eV. The second insertion device, again an ondulator, works differently from most ondulators. Usually, the magnetic field of the insertion device; and thus, the wavelength of maximal emission, is tuned increasing or decreasing the distance between the arrays of magnets (the gap). The novel ondulator keeps the distance between the arrays and changes the phase of the periodic magnetic system above and below the electron path one respect to the other. The permanent magnets are placed in an array of 21 periods. The operative range of the new ondulator is narrower and goes from 130 eV to 1800 eV. Both ondulators are calibrated to give the maximal photon fluence for a certain wavelength, for the first one in function of the gap between arrays of magnets, for the second as a function of the phase
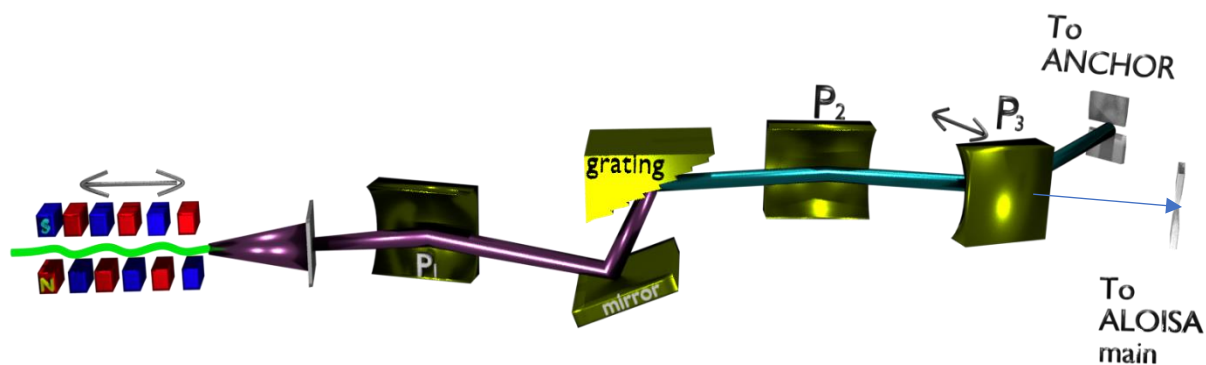

Figure 7: ALOISA beamline. From the left insertion device inside the storage ring of the synchrotron, that moves parallelly respect to the electron orbit in order to change phase of the arrays of magnets. The next element is the pinhole, which allows the extraction of the photons outside the ring. There is a first paraboloidal mirror P_1 that collimates the beam to the monochromator, composed by the mirror and grating in the image. The mirror P_2 focusses the beam on the exit slits of ALOISA main chamber. The beam can be directed instead of the main chamber (following the blue arrow) to the ANCHOR end-station by the mirror P_3, which is a toroidal mirror with a large radius, working similarly to a parabolic one.

between them. The emitted light is parallel to the electron beam until the first bending magnet where electrons deviate from straight trajectory while the photons proceed to the pinhole, which selects the radiation to be transferred outside the ring in the beamline.

At the exit of the pinhole the photon beam is collimated by a parabolic mirror toward the monochromator (the distance between the insertion device and the first mirror is of 21 m). The monochromator is a plane mirror/grating mirror operating in the range of 120-2000 eV. The beam can be directed to the ALOISA main chamber or to the ANCHOR end-station. If directed to the main chamber, the beam is focused by another parabolic mirror on the exit slit and finally a toroidal mirror focuses them on the sample inside the chamber. Between the monochromator and the second parabolic mirror, a retractable toroidal mirror can be placed in order to deviate the beam towards the ANCHOR end-station. All the optics are gold covered and designed to operate in grazing incidence, the deflection angle is of 1°. The photon flux is about 0.5-1 x 10^{12} photons per second, and the resolving power ($\Delta E/E$) is 5000 in the range 250 -900 eV.[19,20] The light presents a horizontal polarization (in the same plane as the undulations in the insertion device and thus parallel to the ground) of 95%. The dimension of the beam on the sample is 40 x 200 μm for the main chamber, while the optics on ANCHOR (AmiNo - Carboxyl Hetero-Organic aRchitectures) imposes a dimension of the spot of about 50 μm in vertical direction (tunable, reported value represents an optimum of flux and dimensions) and of 200-300 μm in the horizontal direction.[21,22]

1.1F ALOISA MAIN CHAMBER

The main chamber of the beamline is divided into two parts, one for the sample preparation and one for the analysis. The preparation chamber offers the possibility of cleaning and heating the sample, monitoring the surface status and depositing of molecules on the surface. The cleaning is achieved by an ion gun which removes contaminations by Argon ion sputtering. The cleaning is then completed by annealing of the sample obtained in two ways, up to 770 K with resistive filaments and, if necessary, further to 1070 K with electron bombardment of the sample holder (the temperature is read by a thermocouple of K type, with its termination on the sample holder). The preparation of a typical sample proceeds then with the deposition of a molecule on the surface through physical vapor deposition from Knudsen cells or from a vial. The cells are used if higher temperatures (570-670 K) are requested for the sublimation of the molecules. If ambient or slightly higher temperature is sufficient, then a Pyrex vial can be employed, sectioned from the chamber through a leak valve (up to two positions for evaporation available). The vial is also the first choice when the molecules are in liquid state. The deposition rate can be monitored with two quartz microbalances, while the sample surface can be monitored, before and after a deposition by a RHEED setup. This last device operates with an electron energy of 15 keV at a grazing angle of 4.25°. Moreover, the preparation chamber has a mass spectrometer (quadrupole), for monitoring residual gasses in the vacuum and controlling the deposition. The sample is mounted in both chambers and during the transfers on the same manipulator, which is fully motorized and has 6 degrees of freedom. The connection between the preparation and the analysis chamber is obtained with a large bronze ball bearing and a system of sliding O-rings. This coupling enables the rotation of the analysis chamber with respect to the ground (being the preparation one held in position) and thus changing the

orientation of the analyzers of the chamber with respect to the polarization of the light. The analysis chamber is equipped with a homemade electron hemispherical analyzer (XPS), with diameter of 66 mm, mounted inside the chamber. The detection of the electrons is achieved with a delay-line made by ELETTRA. In addition, a channeltron for detection of electrons is present, equipped with a grid that allows, if negatively charged, to repel part of the incoming electrons (NEXAFS in partial yield). There are also other 5 electron analyzers with low resolution for Auger coincidence spectroscopy. During the measurement, it is possible to keep the sample at different temperatures, also by cooling it with liquid nitrogen with a piping system; in this way the sample can reach 120 K. Both chambers are pumped into ultra high vacuum (UHV) by two stage pumping, the first achieved by scroll pumps, while the second relies on turbomolecular pumps. There is also a SAES getter passive pump. The operative base pressure is in the order of 10^{-11} mbar, monitored in the preparation chamber by an ion gauge.

1.1G ANCHOR SUNDYN END-STATION

Most of the experimental data reported in this thesis have been acquired at the ANCHOR end-station[23] located at a branch-line of the ALOISA beamline, graphically represented in figure 8. Differently from the main chamber, ANCHOR has only one chamber, used for preparation and for analysis. In addition to the spectroscopic techniques available on the ALOISA main chamber, on this chamber a femtosecond pulse width laser setup is present, optimized for the optical pump of organic systems. It has been integrated in the ANCHOR end-station in order to perform time resolved spectroscopies at MegaHertz repetition rate (the SUNDYN project). By combining resonant photoemission spectroscopy and pump-probe X-ray spectroscopies in the same chamber, we can study the dynamics of the electronic structure of organo-metallic interfaces from the femtosecond to the nanosecond timescales. The insertion of the sample is made possible by a transfer system on a fast entry-lock. The sample preparation includes the possibility of cleaning through sputtering with Argon ions, annealing with resistive filaments up to 920 K, and deposition of molecules from a Knudsen cell or from a pyrex vial separated by a leak valve for volatile substances. It is also possible to cool down the sample to 150 K with liquid nitrogen through pipes connected to the manipulator if a deposition on cold surfaces is requested. The distance between the cell and the sample depends on the employed cell and it is usually about 0.3 m. A different option is represented by a setup of four retractable cells (Kentax) that can be mounted in a vacuum chamber separated from the main one by a gate valve and can be moved inside at a distance of 0.1-0.15 m from the sample. The Kentax cells can be also heated, every single cell of the four independently, by a resistive filament and it is possible to control the current of this filament up to 0.01 A. In addition, it is also possible to dose in the chamber a sublimated liquid, such as water or ethanol, from a retractable needle that allows to approach the sample very close, 1-2 mm.
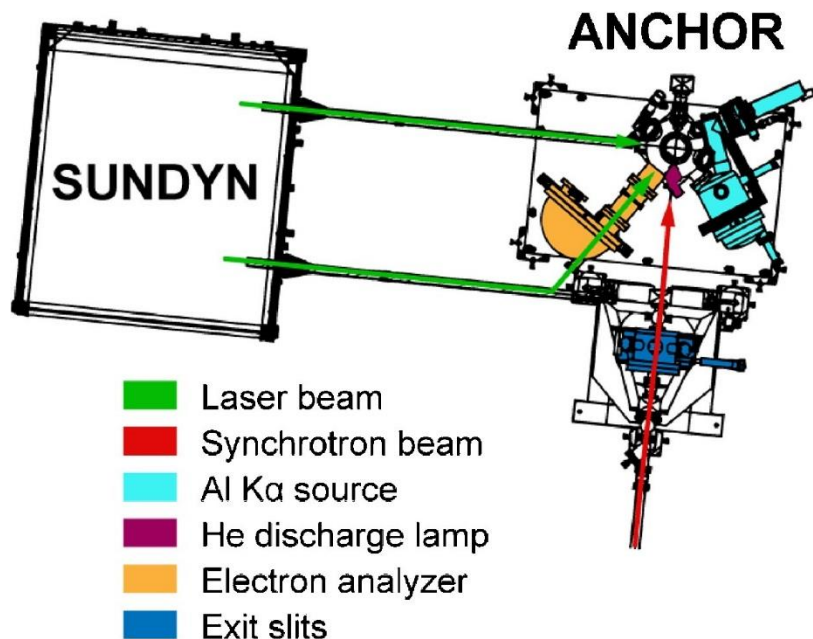
Figure 8: Technical drawing of the ANCHOR end-station and of the SUNDYN apparatus. The laser beam can enter the UHV chamber at an angle of 90° or 35° with respect to the synchrotron beam

Further treatment with vapors can be performed on the transfer line, where, being separated from the chamber by a gate valve, the pressure can be raised up to the atmospheric one. The manipulator offers the possibility of movement along all the three axes, and to rotate to change the azimuthal and axial angles. ANCHOR chamber offers also the possibility of operating without the synchrotron beam. It is equipped with a laboratory X-ray source and a gas-discharge lamp that employs He. The X-ray source is a XM 1000 MkII produced by Omicron and employs a water-cooled anode in aluminum to produce the Al Kα radiation line (1486.7 eV, 0.83396 nm), monochromatized by a Rowland circle monochromator. The gas-discharge lamp, model HIS 13 produced by the German company Focus, provides the possibility of measuring valence band spectra without synchrotron beam. This water-cooled lamp can be used with different gases but during this thesis only He (with purity 6.0) has been employed. The system of differential pumping ensures that the pressure of the chamber is in the range of $2 \times 10^{-8} - 8 \times 10^{-8}$ mbar during measurement. The pressure can be used also to select the desired wavelength between He (I) and He (II) emission lines: a lower gas pressure rises the ratio of the He (II) intensity with respect to the other one while the opposite occurs at higher pressures. The distance between the end of the capillary where the discharge takes place and the sample is about 15 cm and, taking into account the beam divergence of 0.8° provided by the producer, the spot on the sample is about 5.5 mm in diameter, further enlarged when operating at a certain angle between the beam and the sample normal. The relatively large spot and the motorization of the axial angle enables to acquire the valence spectrum as a function of the emission angle, monitoring the band dispersion. The measurements are performed with an electron analyzer mounted on the chamber. It is a PSP resolved 120 analyzer, where the 120 stands for its diameter in millimeters. This analyzer allows to operate at discrete pass energies 1 eV, 2 eV, 5 eV, 10 eV, 20 eV, 50 eV and 100 eV. At lower pass energy the signal is lower but higher is the energy resolution. The detector is a delay line from ELETTRA coupled with a micro channel plate, formed by an array of channeltrons which enhances the signal. The UHV in the chamber (base pressure of 4×10^{-10} mbar) is produced by a three-stage pumping system, composed by a mechanical scroll pump and two turbomolecular pumps all in

sequence. As mentioned before, the discharge lamp has a differential pumping system while the transfer line and the evaporation cells have a two-stage pumping system (scroll pump and a turbomolecular one). The pressure is monitored by an ion gauge and a quadrupole mass spectrometer for residual gases in the chamber and a Pirani in the transfer line.

1.1H SURFACE PHYSICS LABORATORY

Part of the present PhD work has been performed in collaboration with the group of prof. Carla Puglia of the Uppsala University in Sweden in the Surface Physics Laboratory, figure 9, of the Department of Physics and Astronomy. In this laboratory it is possible to use photoelectron spectroscopic techniques. The lab is provided with an UHV chamber composed, as in the previous cases, by a preparation stage, where an ion gun is able to sputter the sample and Knudsen cells to deposit molecules on the sample surface. The sample can be transferred between the sections on the same transfer line. The analysis section is equipped with an X-ray laboratory source, with a water-cooled cathode, able to produce both Al Kα and Mg Kα not monochromatized radiation, for studying the core levels, while the valence band is studied with a helium radiofrequency lamp with a monochromator. The pressure is measured by 2 ion gauges, one in the preparation chamber and one in the analysis one. The samples can be moved inside the chambers via an entry lock with a parking system. In the Surface Physics Laboratory it is possible to cool down the sample with liquid nitrogen, even if the system is not so effective and reaches only 230 K. The base pressure of the chamber is 10^{-9} mbar and is ensured by two stage pumping, scroll as primary pumps and then turbomolecular pumps.
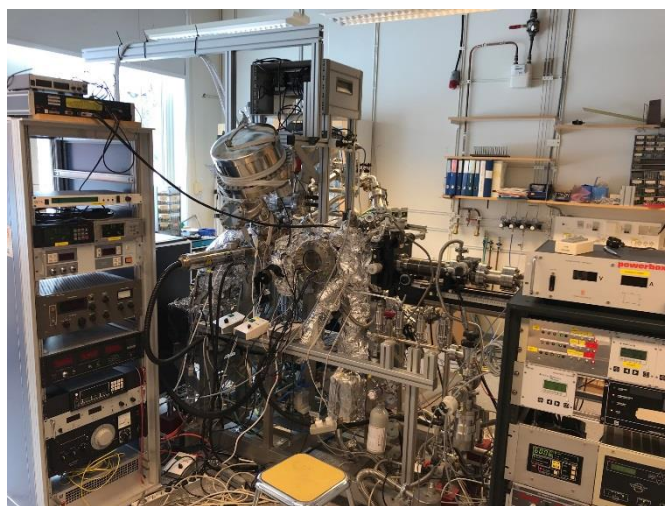

Figure 9: Surface Physics Laboratory, view of the instrumentation. Two chambers are present, separated by a gate valve. The first, on the right used for sample preparation and the second, on the left for the analysis.

1.2A SCANNING TUNNELING MICROSCOPY

In addition to the spectroscopic techniques, also Scanning Tunneling Microscopy, STM, has been very useful for the investigation of our systems. The great potential of this microscopy tool, invented by Binning and Rohrer,[24] resides in the imaging of the surface at the nanometer scale of a conducting material with the aid of a metallic tip. It is important to note that obtained images show not only the topographic contrast, which in this thesis we are more interested in, but also reflects the density of states of the studied material convoluted with those of the tip used to probe it. The working principle relies on the tunnel current measured applying a bias voltage between the sample and the tip. This quantum effect allows a particle to have a certain probability of being transmitted across the barrier. The solution of the Schrödinger equation limited to one dimension (z), presents in the barrier (starting at Z_0) a decaying solution of the type:

$$\varphi = \varphi(z_0)e^{-kz} \qquad\qquad k = \frac{\sqrt{2m(E-U)}}{\hbar}$$

with m the mass of the particle, electron in this case, E the energy and U the potential barrier, $\phi(z_0)$ is the value of the wavefunction at the start of the barrier. The current that is tunneling across the barrier is present only when applying a bias between the sample and a metallic tip and is proportional to:

$$I \propto \sum_{E_f - eV_b}^{E_f} |\varphi(z_0)|^2 e^{-2kd}$$

with d the dimension of the of the barrier, or in practice the sample-tip distance. It is very important to notice the exponential dependence of the current on the distance. In a STM experiment the tip is usually of wolfram or palladium-iridium, and the movements, on the nanometric scale, are done with piezoelectric motors.[25] There are two modes of acquiring STM images. It is possible to maintain the height (z) of the tip constant. In this mode the tip is scanning in the xy plane and is mapping the variations of current as a function of the xy position. This method is rather rapid but rough topographic variations can lead to a crash between the tip and the sample. Alternatively, it is possible to maintain constant the current and the height of the tip is corrected by a feedback circuit. In this way the scan is slower but there is minor risk to crash the tip. In this thesis STM has been used to provide an insight on the morphology and on the order of our 2D materials. Moreover, STM images have been important in guiding the DFT calculations.

1.2B OSMOS LABORATORY AT ELETTRA

Part of the scanning tunneling microscopy (STM) images has been acquired at the OSMOS[26] (On Surface Modification of Organic Semiconductors) laboratory. The experimental apparatus is composed of a preparation chamber where an ion gun allows to sputter the sample, which then can be heated with a resistive wiring to 720 K and through electron bombardment to 970 K on a sample manipulator with four degrees of freedom (three translations and the axial angle). The chamber offers also the possibility of deposing molecules from Knudsen cells and the monitoring of residual gases with a mass spectrometer. For a characterization of the surface of the sample there is a LEED (low energy electron diffraction) setup. Connected to the preparation chamber, there is the spectroscopic chamber where a gas discharge lamp and an electron analyzer are mounted. Connected with the preparation chamber there is also the proper STM chamber. The instrument, an Aarhus model of Specs, has a massive copper block covered by gold to avoid oxide formation, suspended by springs and elastomers, which help in noise suppression. Inside the copper block there are the piezo-electric motors that move the tip directed upward. The sample can be cooled to 120 K with liquid nitrogen. The STM chamber is also equipped with an ion gun for the sputtering of the tip. All the movements of the sample between chambers are performed by magnetically controlled "wobblesticks".

Figure 10: view of the OSMOS laboratory. On the right is the STM chamber, separated with a gate valve from the preparation chamber, where also the LEED is present.

BIBLIOGRAPHY:

1. Hertz, H. Ueber einen Einfluss des ultravioletten Lichtes auf die electrische Entladung. *Ann. Phys.* **267,** 983–1000 (1887).

2. Einstein, A. Über einen die Erzeugung und Verwandlung des Lichtes betreffenden heuristischen Gesichtspunkt. *Ann. Phys.* **322,** 132–148 (1905).

3. Hüfner, S. *Photoelectron Spectroscopy : Principles and Applications*. (Springer Berlin Heidelberg, 2003).

4. Chastain, J., King, R. C. & Moulder, J. *Handbook of X-ray photoelectron spectroscopy: a reference book of standard spectra for identification and interpretation of XPS data*. (Physical Electronics Division, Perkin-Elmer Corporation Eden Prairie, Minnesota, 1992).

5. Watts, J. F. & Wolstenholme, J. *An Introduction to Surface Analysis by XPS and AES*. (John Wiley & Sons, Ltd, 2003). doi:10.1002/0470867930

6. Cumpson, P. J. & Seah, M. P. Elastic scattering corrections in AES and XPS. II. Estimating attenuation lengths and conditions required for their valid use in overlayer/substrate experiments. *Surf. Interface Anal.* **25,** 430–446 (1997).

7. Ethiraj, A. S. & Kang, D. J. Synthesis and characterization of CuO nanowires by a simple wet chemical method Synthesis and characterization of CuO nanowires by a simple wet chemical method. 1–5 (2012). doi:10.1186/1556-276X-7-70

8. de Groot, F. & Kotani, A. *Core Level Spectroscopy of Solids*. **6,** (CRC Press, 2008).

9. Kinsinger, J. A., Stebbings, W. L., Valenzi, R. A. & Taylor, J. W. Spectral evaluation of a sealed helium discharge lamp for studies in photoelectron spectroscopy. *Anal. Chem.* **44,** 773–777 (1972).

10. Drake, G. W. F. GWF Drake and WC Martin, Can. J. Phys. 76, 679 (1998). *Can. J. Phys.* **76,** 679 (1998).

11. Stöhr, J. *NEXAFS spectroscopy*. **25,** (Springer Science & Business Media, 2013).

12. Brühwiler, P. A., Karis, O. & Mårtensson, N. Charge-transfer dynamics studied using resonant core spectroscopies. *Rev. Mod. Phys.* **74,** 703–740 (2002).

13. Föhlisch, A. Ultrafast charge transfer and nuclear dynamics studied with resonant X-ray spectroscopy. *Appl. Phys. A* **85,** 351–359 (2006).

14. Sakurai, J. J. & Commins, E. D. Modern quantum mechanics, revised edition. (1995).

15. Jennison, D. R. Auger-Electron Spectroscopy as a Local Probe of Atomic Charge: Si $L_{2,3}$ VV. *Phys. Rev. Lett.* **40,** 807–809 (1978).

16. Rye, R. R., Kelber, J. A., Kellogg, G. E., Nebesny, K. W. & Lichtenberger, D. L. Localization effects in the Auger spectra of ring nitrogen systems: Pyridine, poly(2-vinyl)pyridine, borazine, and boron nitride. *J. Chem. Phys.* **86,** 4375–4383 (1987).

17. Björneholm, O., Nilsson, A., Sandell, A., Hernnäs, B. & Mrtensson, N. Determination of time scales for charge-transfer screening in physisorbed molecules. *Phys. Rev. Lett.* **68,** 1892–1895 (1992).

18.   Keller, C. *et al.* Femtosecond dynamics of adsorbate charge-transfer processes as probed by high-resolution core-level spectroscopy. *Phys. Rev. B* **57,** 11951–11954 (1998).

19.   Cvetko, D. *et al.* First results from the new optical configuration for a synchrotron radiation monochromator applied to the ALOISA beamline. in **3150,** 3111–3150 (1997).

20.   Floreano, L. *et al.* Performance of the grating-crystal monochromator of the ALOISA beamline at the Elettra Synchrotron. *Rev. Sci. Instrum.* **70,** 3855 (1999).

21.   Busetto, E., Lausi, A. & Bernstorff, S. The high-energy monochromator for the ALOISA beamline at Elettra. *Rev. Sci. Instrum.* **66,** 2078–2081 (1995).

22.   Costantini, R. *et al.* ANCHOR-SUNDYN: A novel endstation for time resolved spectroscopy at the ALOISA beamline. *J. Electron Spectros. Relat. Phenomena* **229,** (2018).

23.   Costantini, R. *et al.* ANCHOR-SUNDYN: A novel endstation for time resolved spectroscopy at the ALOISA beamline. *J. Electron Spectros. Relat. Phenomena* **229,** 7–12 (2018).

24.   Binnig, G., Rohrer, H., Gerber, C. & Weibel, E. Surface Studies by Scanning Tunneling Microscopy. *Phys. Rev. Lett.* **49,** 57–61 (1982).

25.   Chen, C. J. Introduction to Scanning Tunneling Microscopy Second Edition. *Oxford Univ. Press* (2008) (2008). doi:10.1002/jemt.1070280110

26.   Baby, A. *et al.* Lattice Mismatch Drives Spatial Modulation of Corannulene Tilt on Ag(111). *J. Phys. Chem. C* **122,** 10365–10376 (2018).

CHAPTER 2: ON SURFACE SYNTHESIS OF BOROXINE BASED 2D SYSTEMS

The demand for technological advancement in many different field of industry and such as electronics, energy storage, health care, just to mention some of them, has put a significative accent on the preparation of smart devices at the nanoscale. The preparation of these novel tools relies upon two strategies differing for the fabrication approach, the top-down and the bottom up. Lithographic[1] and etching[2] techniques represents the classic examples of the first approach. The extension of objects that can be obtained with these techniques spans from tenth of nanometers to millimeters. This strategy has been applied to a large palette of materials and systems spacing from transistors[3] in electronic devices to novel biomedical devices.[4] With to the bottom up strategy, it is possible to fabricate nanomaterials or nanodevices starting with a smaller precursor, for instance molecules. It is possible to employ the bottom up concept for inorganic materials, such as $MoSe_2$[5] or MoS_2,[6] or for organic molecules that can be used as precursors of the nanostructures that are created.[7] In general, the use of molecules relies on chemical reactions that are able to link them together, forming a nanomaterial, usually a thin film. In this process a relevant role is played by the substrate on which growth processes take places from precursors molecules deposition to the synthesis. As for the reactions in solution, this synthesis can involve the breaking and establishing of bonds and changes in molecular conformation. The success of these processes relies on a well-defined and reproducible reactivity of the employed molecules. The present chapter is focused on a precise class of chemical compounds, the boronic acids, that fulfill these requests and currently are studied for nanostructured materials production. Their use in different fields is very shortly reviewed, for a much deeper insight of the various applications and studies of this compounds please refer to Hall.[8] After this brief description, the aim is restricted to the on-surface synthesis, where this class of compounds has an important role. Then the study of three systems is presented. The first one can be viewed as a prototypical system, useful to better understand the boronic materials that are reported in recent literature. This latter is especially suitable for a deep spectroscopic characterization supported by STM imaging and theoretical modeling.[9] The second system is quite similar to the first one and is useful to understand if the results obtained are extendible to other cases. The last system of this chapter is a novel 2D material based on boron and oxygen, that shows intriguing electronic properties.[10]

2.1 INTRODUCTION

Boronic acids are a class of chemicals that are widely adopted in many different fields. Structurally, the boronic functional group contains a trivalent boron atom with one carbon substituent and two hydroxyl groups. The electron deficiency of boron atom imposes a trigonal planar geometry to the functionality.[11] It is worth noticing that these compounds are not found in nature and have to be synthesized. In a historical context, the first synthesized boronic acid was ethylboronic acid by Frankland and Duppa in 1860 [12] , while the phenylboronic acid, used also in this thesis, was reported for the first time in 1880.[13] In 1909 was found what became the classical synthesis process for the boronic acids, the reaction of a trialkyl borate with a Grignard reagent followed by hydrolysis.[14,15] The boronic group has a character of weak Lewis acid due to the presence of the electron deficient atom of boron. This reflects to its behavior in water solutions, where it acts as an acid, but in contrast with carboxylic group, its anionic form (the

conjugate base) has a tetrahedral form, binding another hydroxyl group [RB(OH)$_3$]$^-$ as depicted in the figure 1 a). A look at their acid constants reveals in an even clearer way the weak nature of the boronic acids, being the pK$_a$ of phenylboronic acid 8.7,[16] while the methylboronic acid has the pK$_a$=10.4 (for comparison, for the boric acid it is 9.2[17]). From the point of view of the chemical synthesis, the interest in boronic acids relies on the possibility of different reactions that they can undergo. Analogously to many other acids, boronic esters can be prepared if hydroxyl groups are replaced by alkoxy ones, as shown in figure 1 d). The esterification reduces the polar nature of the boronic termination because there is no more the possibility of the hydroxyl groups to act as donor in H-bonding. This reversible condensation reaction is shifted toward the products when employing a preorganized diol molecule or removing the water molecules from the reaction environment.[18] The boronic acids and their esters are nowadays important building blocks for the organic chemist due to their application in the Suzuki-Miyuara reaction, one of the greenest coupling reactions.[19] Moreover, the formation of esters with diols (or polyols) especially if they have an important biological role, opens to applications in the biological and analytical fields for these compounds. Indeed, on the basis of the strong interaction of boronic acids and saccharides studied for the first time in 1954[20], it has been possible to design sensitive and selective receptors for
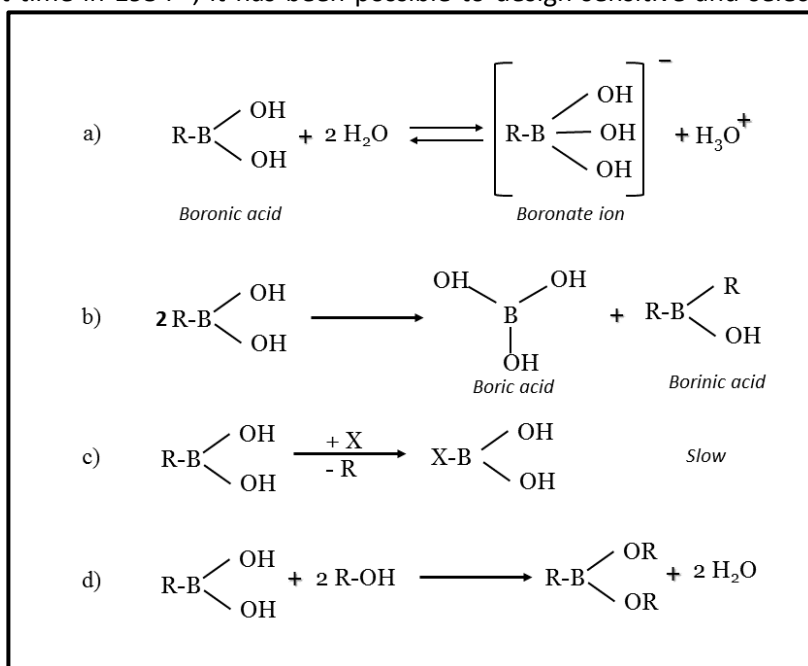
Figure 1: relevant reactions of the boronic functional group. a) the acid-base equilibrium in water solution of these acids with the formation of the tetrahedral boronate ion. b) disproportionation reaction of a boronic acid, c) substitution of the carbon substituent and d) formation of a boronic ester.

carbohydrates since 1992.[21] Changing field of application, the strong chemical affinity to diols, together with the Lewis acidity of the boron atom, make boronic acids suitable for interesting applications in biology and medicine, where they may be used as: enzyme inhibitors (as the Bortezomib[22], which has already been approved by the Food and Drug Administration); artificial sensors[23]; and as biomimetic agents.[8] Coming back to the analytical field, the interaction of boron, acting as a Lewis acid, with a Lewis base opens to the use of the boronic group in developing sensors for anions like fluoride[24], chloride[25], cyanide, dicarboxylic acids and α-hydroxy carboxylic acids[26]. Moving to the chemical synthesis, the condensation reaction, which boronic acids can undergo, is widely employed in the fabrication of
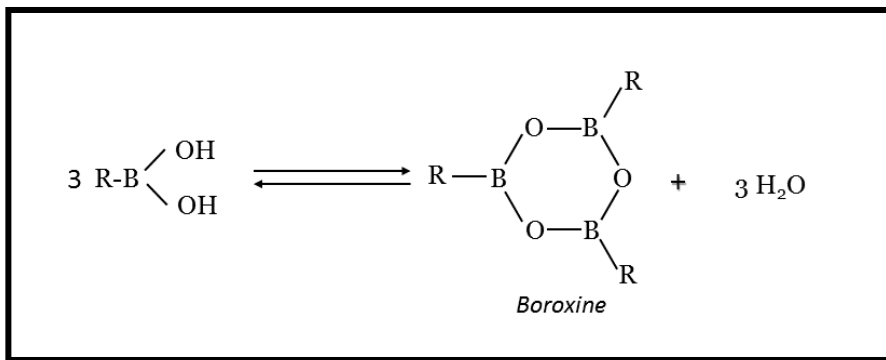
Figure 2: Boroxination reaction, also referred in this text as (auto)condensation reaction or boroxine formation.

heterogenous and polymeric structures. Both hetero-condensation with alcohols and auto-condensation are relevant for the synthesis of novel materials. The facile synthesis processes as well as their reversibility in presence of water are among the main advantages of the boronic-based polymer formation. In the case of boronic-diol condensation, these aspects have been used by Lavigne to create self-healing polymers.[27] Similar synthetic concepts have been borrowed also for hydrogels fabrication and have been recently reviewed by Guan and Zhang.[28] The undoubted advantages of the boronic-diol reaction have not passed unobserved in the covalent organic framework (COF) field. COFs are covalent networks of molecules, characterized by the presence of nanopores in their structure. The interest in these novel materials has risen in the past years due to their outstanding potential applications which include gas storage, gas separation, superhydrophobic interfaces, catalysis, energy conversion, energy storage, and optoelectronics.[29] The first example of COF was published in 2005 by Yaghi and since then many efforts have been spent for synthetizing and exploring new covalent organic frameworks.[30] Alternatively to the boronic-diol condensation, the anhydride formation (referred in this text also as boroxination or auto-condensation reaction, putting accent on the release of water and depicted in figure 2, which links three boronic groups into a six-membered boroxine ring, B_3O_3, of alternating boron and oxygen atoms, is another valuable route to the formation of polymeric structures. These rings possess a little aromaticity and are flat, as evidenced by X-ray crystallography.[31] The boroxine ring offers some interesting properties that makes it rather versatile. First of all, it is not difficult to prepare, and it imposes a specific triangular orientation of the attached groups that eases the formation of precisely shaped frameworks. Moreover, in solution there are two methods of inducing the boroxination reaction. One is the removal of water that is created during the reaction with a drying agent, but it is also possible to help the reaction using ligands.[32,33] These compounds, mostly based on nitrogen atoms that interact with their lone pairs with the electron poor boron, provide the driving force in the boroxine formation. In addition, this condensation reaction is an equilibrium reaction (equilibrium between the condensed ring plus three molecules of water on the one side and free boronic acid on the other).[34,35] This aspect can be exploited and in appropriate conditions there is the possibility to slow down the reaction and to improve the morphology of the framework. On the other hand, this equilibrium in the formation reaction is also the weak point of the frameworks based on the boronic acids, making them suffer of water instability. These aspects of the boroxine ring have to be evaluated differently if working under ultra high vacuum conditions rather than in solution. On the one hand, there is no more the structural instability caused by the presence of water, while on the other hand the possibility of error correction is hardly feasible due to the quick removal of H_2O molecules. Nowadays, the idea of the COF does not belong only to the 3D domain, but also the surface

science investigates upon the possibility of forming regular organic frameworks, limiting the dimensionality of the system to 2D. In particular, surface science has been attracted by the advantages of the boronic acids in forming frameworks. In this branch of research, it is crucially important to tailor the structural and chemical properties of the substrates at the nanoscale.[36,37] The 2D COFs have shown a great variability in shape and have evidenced the possibility of a rational design in the 2D material field. Coupling this property with their great stability coming from the covalent nature of the created bonds, they have been proposed as an alternative to the hydrogen bond or Van der Waals interaction-based frameworks. In this view, the COFs are very interesting as host-guest templates of surfaces, specially taking into account that conventional nanopatterning of a surface relies on lithography, a technique that, suffering the diffraction limit and the beam scattering, has a resolution of few tens of nanometers. This value is rather large when compared with the pore diameter of a boronic COF, for instance the one created by 1,4 benzendiboronic has pores of about 1.5 nm. In this direction, an outstanding example of the templating capabilities of boronic COFs has been published by Plas et al.[38] showing the possibility of the framework to direct the subsequent deposition of another molecule, C_{60} in that case, in precise positions on the surface. Regarding the preparation, the synthesis of 2D COFs can be performed both in solution and UHV conditions. The precursors are molecules with two boronic functionalities linked by a "spacer" which, in the works present in literature, contain an aromatic subunit. On the other hand, a frequent issue in the synthesis of these films is the proliferation of defects that makes the material deviate from the ideal structure. Working in solution, a strategy to limit this problem consists in taking advantage of the reversibility of the polycondensation reaction that leads to the formation of the COF. Moreover, Dienstmaier et al. have explored the effect of a partial pre-polymerization in solution on the order of a boronic framework.[39] In the case of an UHV synthesis, the defects are function of the interaction of the precursor molecule and substrate as well as of the growing conditions. Apart from the presence of defects, the boroxine-based framework suffers another drawback. In particular, the boronic COFs transport electrons with low efficiency. The reason beyond this aspect is that usually a boroxine based COF is constituted by boroxine rings and aromatic spacers between them. Since the first possess only a low aromaticity, they cannot act as electron-transferring bridges between the aromatic subunits.[40,41] Therefore, the in-plane conduction is suppressed and the valence band near the Fermi level shows flat-band characteristic. In this perspective, it is difficult to think at boroxine based COFs as electrodes, but thanks to their shape tunability and robustness they can have a role in the tailoring of an electrode.

2.2 THE BOROXINE-AU INTERFACE: PHENYL BORONIC ACID (PBA) ON AU(111)

The study of boronic terminated molecules on surfaces has been so far limited to di-boronic species, which possibly lead, upon condensation, to the formation of extended 2D frameworks. However, the assembly of molecules with a single boronic termination presents two interesting issues we have tackled. First, as the result of the boroxination of the precursors, larger molecules can be synthesized on surface, which may have interesting properties to be studied; second, the system represents a valuable reference for investigating both the boroxination process and the properties of the boroxine-substrate interface, to be then employed to describe the more complex cases of COFs. For this purpose, we have chosen a simple boronic acid, namely the phenylboronic acid (shortly PBA, depicted in the lower part of the figure 3) to study its self-assembly on the Au(111) surface, which to our knowledge has not been done yet. The study of PBA does not only ease the interpretation of experimental results, but also sharpen the theoretical

investigation limiting the case of interest to a trimer on a metallic substrate. In order to obtain a reliable insight into the properties of the system we have performed an XPS investigation, necessary also to confirm the boroxine formation, a NEXAFS study to understand more deeply the electronical properties further investigated by the RESPES technique. The spectroscopic study was completed by density functional theory (DFT) simulations, performed by the group of prof. Fronzoni, University of Trieste, and STM measurements acquired in collaboration with the group of prof. Comelli, University of Trieste and CNR-IOM.

2.3 EXPERIMENTAL SECTION PBA ON AU(111)

The Au(111) substrate was cleaned by cycles of sputtering and annealing and the presence of contaminants was monitored by XPS. The PBA (Sigma Aldrich, 97% of purity) has been dosed from a Pyrex vial connected to the chamber through an all-metal valve. The sample has been held at room temperature to obtain the monolayer, while the multilayer coverage has been reached cooling the sample at 230 K. The calibration of the XPS measurement of the deposited PBA on gold substrate were done with Au 4f peaks. The STM images were acquired at 4 K with a liquid Helium cooling.

2.4 XPS AND STM RESULTS OF PBA ON AU(111)

The XPS measurements taken at monolayer and at multilayer coverages, reported in figure 3, allow evaluating the proceeding of the boroxination reaction. In the multilayer stage, the molecules of the outer layers are not in contact with the substrate. The picture of a weakly interacting thick film is confirmed by the desorption of the film occurring at low temperatures: at ambient temperature only a single layer, directly interacting with gold, is present, which is stable upon annealing of the sample up to 450 K. The monolayer stage can be obtained by depositing the PBA at room temperature (RT), where the formation of a second layer is inhibited. In this case, a deposition of 5 minutes at a pressure of $5*10^{-7}$ mbar is enough to form the layer. The analysis reveals that the spectra are affected by a clear image charge effect that shifts the signal between the two coverages, multilayer and monolayer. Assuming that there is no chemical change on the carbon atoms (since the interaction with the substrate is weak), we have aligned these peaks and imposed a correction of the same value on the oxygen and boron peak. The resulting spectra, reported in figure 3, indicate that there is a chemical shift on O1s signal of 0.3 eV toward lower binding energy and a very small shift on B1s toward higher binding energy. A significant chemical shift on oxygen is in line with what reported by Dienstmaier[39] et al. The interpretation we give to this change is that at the multilayer coverage, the molecules are weakly interacting and are not boroxinated, but at the monolayer coverage the molecules are found in boroxinated form. This interpretation is confirmed by the
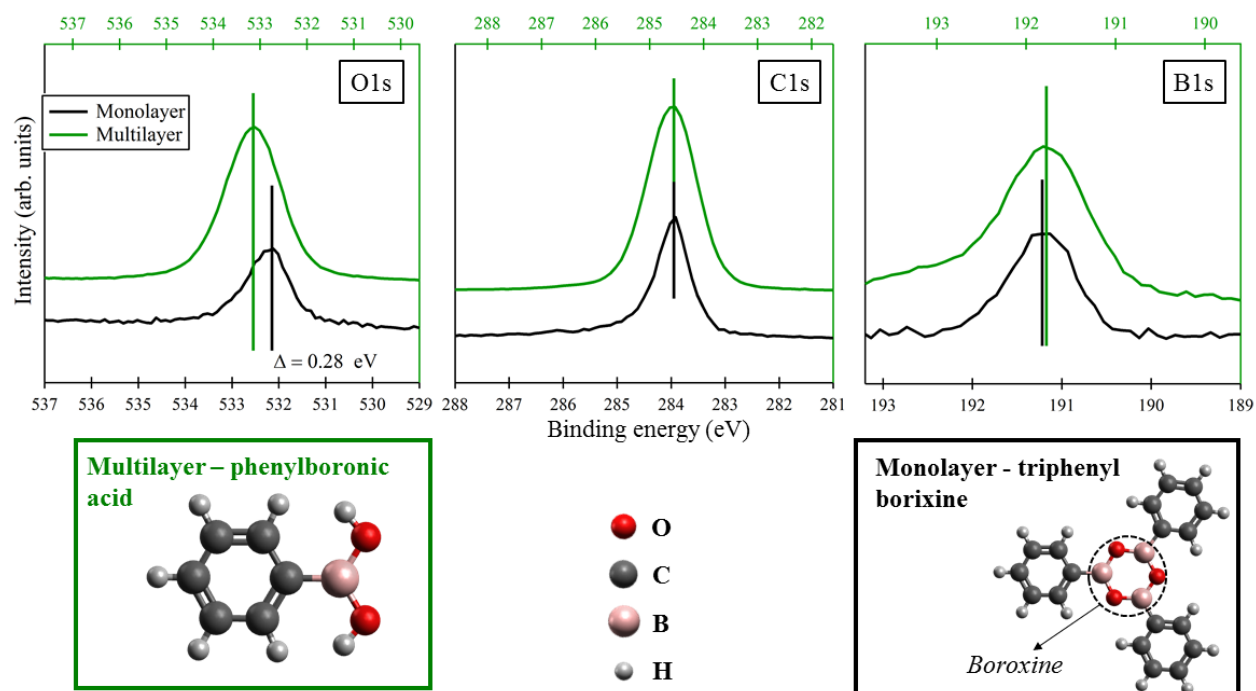
Figure 3: In the upper part the XPS spectra of O, C and B are reported. The green line represents the signal of the multilayer while in black the monolayer is reported. The multilayer binding energy is referred to the green scale on the top of each spectrum, whereas the monolayer binding energy is referred to the bottom black scale. To take into account the screening effect, the carbon peaks have been aligned, imposing a shift of 0.6 eV between the two energy scales in each spectrum. The O1s monolayer is shifted toward lower binding energies, even after subtracting the screening effect, indicating a change in the chemical environment. Also, the B1s signal shows a minor change, in the opposite direction. The species present at the multilayer coverage, unreacted phenylboronic molecules, and at the monolayer coverage, trimeric triphenyl boroxine units, are shown in the lower part. All the XPS spectra have been taken at 650 eV photon energy and 20 eV of pass energy. The peak position has been calibrated with the substrate Au4f$_{7/2}$ at 84 eV. The colors of the ball and stick model are preserved in the whole chapter.

reciprocal signal intensities, corrected for the cross-section factors and -for multilayer- also for the different inelastic mean free path, it is possible to observe that the ratio between the boron and oxygen atoms decreases of a factor two passing from the thick film to the monolayer, as expected from the proposed condensation reaction. In addition to the XPS data, also the STM technique, providing an insight in the situation on the surface, suggests that the boroxination reaction takes place at the monolayer. Indeed, the images acquired at this level of coverage reveal the presence of trilobate structures compactly assembled on the surface, as can be evicted from the image reported in figure 4. The shape and dimensions of these structures are compatible with the product of the condensation of the PBA in triphenylboroxine (TPB). It has also been possible to acquire images of a 1.5-layer coverage, visualizing trimeric objects on the surface which are of different dimensions than the condensed units. We suggest that the second layer is formed by unreacted molecules and we propose a model, shown in the inset of figure 4, of three PBA molecules interacting via hydrogen bonding, which can represent the morphology visualized by STM. It is important to point out that the boroxine formation reaction of PBA is taking place at room temperature. This is in contrast with what was observed for the di-boronic phenyl, the 1,4 benzendiboronic acid, which undergoes the same condensation reaction only after heating to 380 K.[42] A possible explanation of this discrepancy can be found in the morphology of the thick film. The PBA
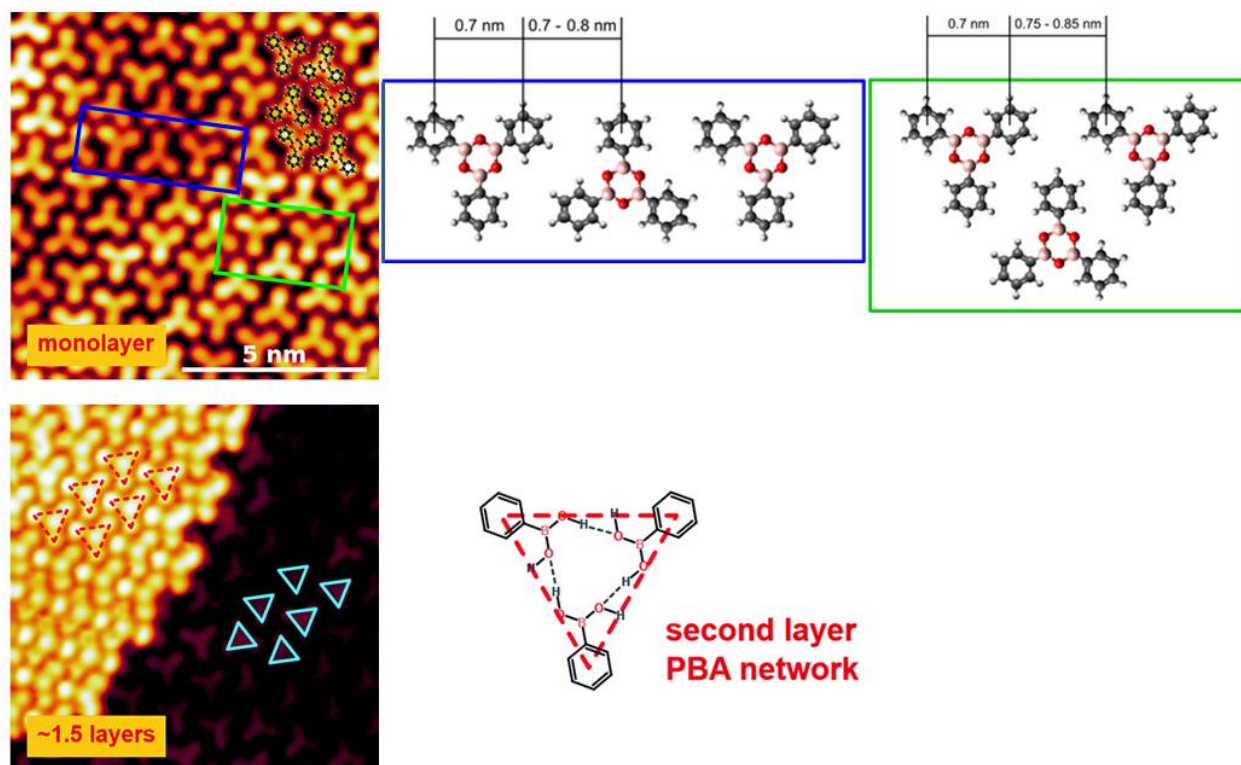
Figure 4: in the upper part are shown the image of the monolayer coverage with molecular models of the condensed trimers. In the lower part is reported an image acquired at 1.5 monolayer which enables to measure the unreacted molecules. The assembly even driven by the hydrogen bonding present already trimers. The model of this film shown on the left. The parameters of acquisition of the STM images: for the upper $V_s = -2.0$ V, $I_t = 0.5$ nA, 10×10 nm², for the lower $V_s = +0.1$ V, $I_t = 0.1$ nA, 10×10 nm². The images have been acquired in collaboration with the group of prof. Comelli. The image has been adapted from ref 9

molecules studied here, already in the unreacted stage (the 1.5-layer coverage is taken as a model for the unreacted monolayer) assemble in a geometry that somehow pre-organizes the molecules for the condensation reaction into boroxine. By contrast, 1,4 benzendiboronic acid at low temperatures forms a different pattern of H-bonded phase. The para position between the boronic groups promote a head-to-tail interaction geometry with only pairs of molecules interacting per time, leading to a rather compact phase formed by molecular chains. Thus, they assemble in a different geometry than the boroxinated phase and a certain steric constraint hinders the conversion. Moreover, a careful investigation also points out a different peak broadening in the O1s signal, having the monolayer peak of a narrower shape than the multilayer. Even this feature can be explained with the proposed model of hydrogen bonded phase, where two inequivalent oxygen atoms are present.

2.5 NEXAFS and RESPES analysis of PBA on Au(111)

In order to better characterize this prototypical system, we have performed a NEXAFS spectroscopic study aimed to monitor the empty states of the boroxinated phase. Both boron and oxygen K-edges NEXAFS spectra are strongly dichroic between s and p polarization and indicate a flat geometry deposition consistent with the STM images. The attribution of peaks to transitions to unoccupied orbitals is possible thanks to theoretical calculations. For a better understanding, the calculation has been performed first on
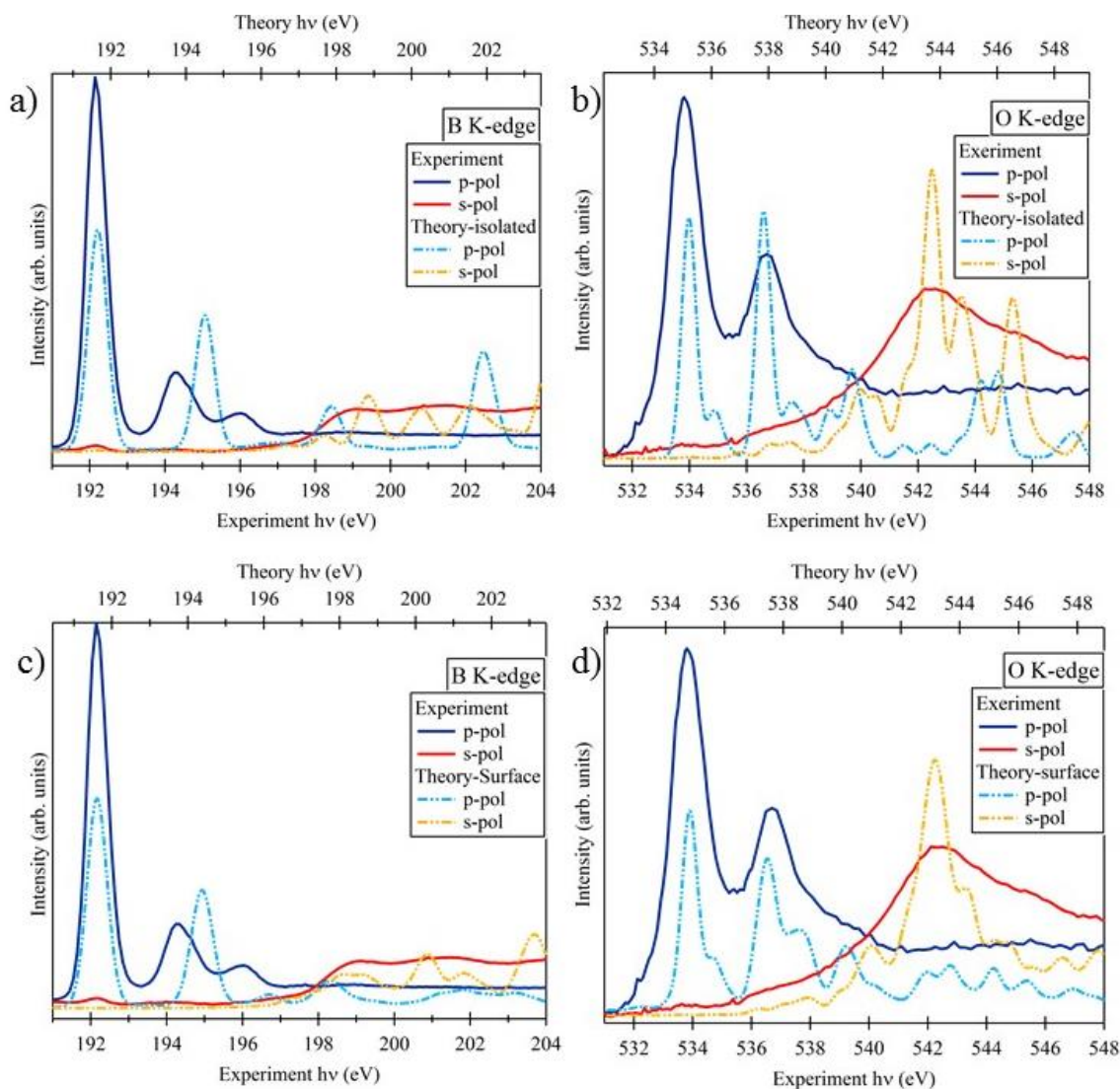
Figure 5: NEXAFS spectra of the triphenyl boroxine (TPB) in every graph the experimental spectrum is referred to the bottom scale while the calculated one is referred to the top energy scale. The experiment and simulation have been aligned to the first peak shifting relatively the two energy scales. a) the boron K-edge spectrum in both polarizations compared with the calculated one of a TPB isolated in vacuum. b) The same for the oxygen K-edge signal. c) and d) report the same experimental spectra but confronted to the simulation performed on TPB on the Au(111) surface. The calculations have been obtained in collaboration with the group of prof. Fronzoni. The experimental NEXAFS signals have been acquired in partial electron yield, with a cutoff at 150 eV for boron and 450 eV for oxygen spectra. The overall resolution is 100 meV for B and 200 meV for O signal. Image adapted from ref. 9.

the boroxinated trimer isolated in vacuum, then the surface has been added to evaluate the effect of the substrate (the lateral interaction between molecules can be supposed to be weak, because of the large distance, 7-8 Å, between them as shown by the STM images). Regarding the experimental B K-edge
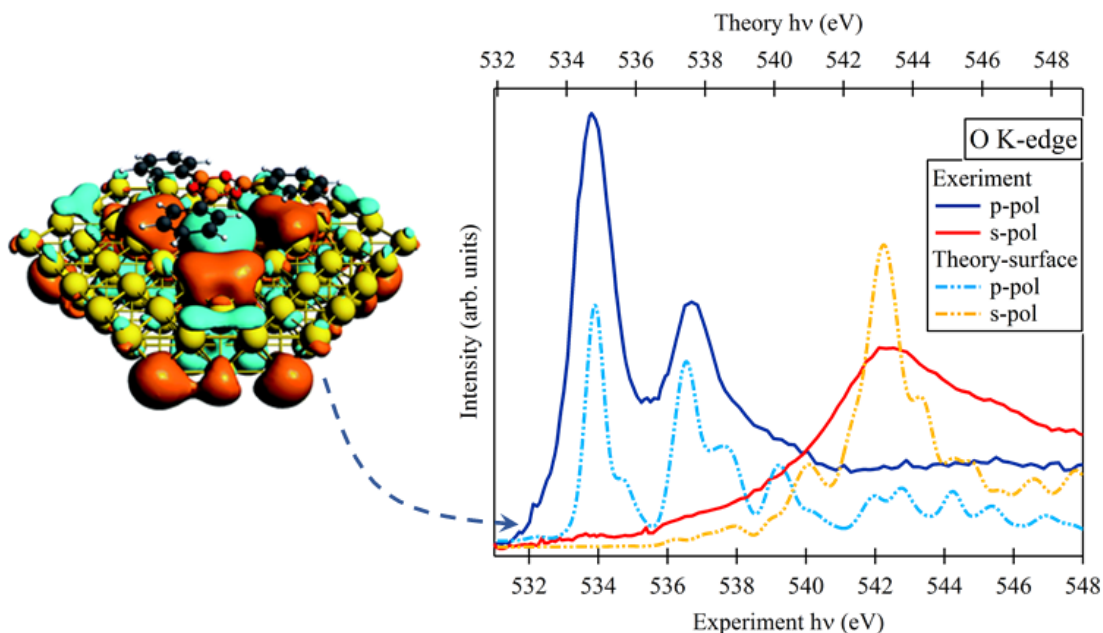
Figure 6: the NEXAFS signal of the O K-edge presents a broader first peak and the calculation of the spectrum in presence of the surface indicates a transition to an orbital, reported in the left part, that has a strong component of the Au atomic orbitals. The graph reports the same as in figure 5 d). image adapted from ref 9.

NEXAFS, the p-polarization spectrum presents two main features at 192.15 and 194.25 eV of photon energy. By comparison with the calculation of freestanding TPB, after alignment of the experimental spectrum and of the simulated one on the first peak of each NEXAFS, they can be attributed to transitions to empty orbitals with π^* geometry which, in a LCAO view, come from the B $2p_z$ atomic component of the boroxine ring and from the C $2p_z$ components of the phenyl ring. Due to the flat adsorption geometry, these peaks are not present in the s-polarization spectrum of the B K-edge, which has no significant peaks before the threshold. Worth noticing is the distance between the two principal peaks of the p-polarization, wrongly predicted by the theory. To investigate the underlying reasons for disagreement with the experiment, we have performed other simulations of the B 1s spectrum of the free TPB, employing different computational schemes both in the DFT and in the Time Dependent DFT (TDDFT) frameworks. Since all calculations confirm the same nature of the two peaks we are confident about the proposed assignment of the measured B 1s spectral features; the observed discrepancies have to be ascribed to the limited amount of final state correlation effects that are included in computational approaches, which deserve future investigation. Passing to the O K-edge spectra, there is an analogue situation. The p-polarization presents two transitions, at 533.8 and 536.7 eV, to π^* type orbitals that the calculation identifies with transitions to orbitals delocalized over the boroxine ring and all the phenyl rings with significant $2p_z$ contribution from carbon and boron atoms and a minor measure from the oxygen atoms. The s-polarization spectrum is almost featureless before the ionization threshold as a consequence of the flat geometry. Moreover, it is possible to notice that the first peak of the O K-edge NEXAFS has a width far larger that the boron analogue. In order to understand this aspect, it is necessary to take into account also

37

the interaction with the substrate, including a slab of gold atoms in the simulation. The overall effect on the simulated spectra is small, reflecting the weak interaction of the metal with the molecular film. The differences regarding the boron NEXAFS are limited to small intensity redistribution among the closely spaced transitions around the main excitation to π^* type orbitals. More interestingly, the oxygen NEXAFS is more influenced by the substrate. Empty states result generally more disperse in energy and, more interestingly, there is a new low energy spectral line calculated at 533.2 eV, just below the main transition line. The corresponding transitions involve a final state with strong Au atomic orbitals contributions and is able to explain the broadening of the first principal transition line of the O K-edge signal. Figure 6 evidences a shoulder in the low energy tail of the main transition, that could be due to this interface state, whose calculated density is depicted in the left panel of the figure. Even if it is not possible to resolve that singular spectroscopic feature, the presence of the broadening, with this possible substrate-induced explanation, requests a deeper investigation. The key importance of this interface state resides in the fact that an electron promoted to this orbital can further delocalize in the metallic substrate, revealing thus a channel for electron transfer between substrate and molecule, and in particular the oxygen atom of the boroxine. The investigation in this direction has been performed with the RESPES technique on the O K-edge, able to investigate this kind of charge dynamics in the femtosecond range. For clearness, we have attributed names to the arrival orbitals as follows: LUMO is the first of the two main features of the NEXAFS spectrum, LUMO+1 is the second feature whereas IMO (Interface Molecular Orbital) is the state with the strong contribution from Au atoms, which we are interested in. The RESPES detects, as shown in figure 7, the energy distribution of the outcoming electrons as a function of the photon energy during a scan across a photoemission edge (O K-edge in this case). For energies high above the photoemission edge (photon energy > 538 eV) the Auger has a kinetic energy not varying any more for changes in the photon energy and reflecting the state of the molecule: a negative ion with a core-hole decaying via normal Auger
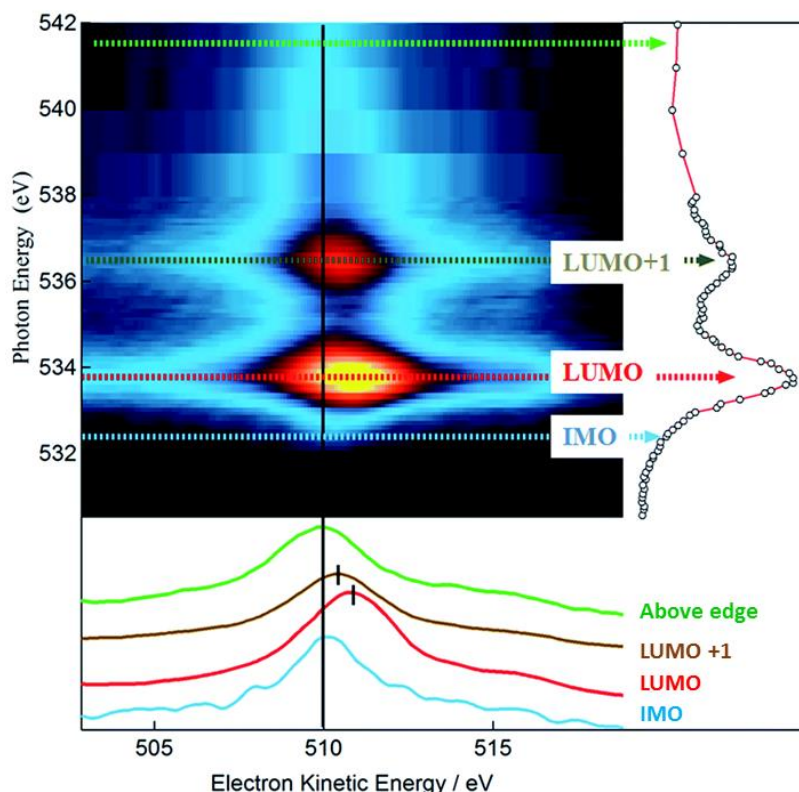

Figure 7: RESPES map of the TPB layer on the Au(111) surface. The image has been obtained after subtraction of the pre-edge and calibration of the energy scale to NEXAFS peaks, reported on the right of the figure and measured separately acquiring, after every scan in kinetic energy, a single point in partial electron yield. image adapted from ref 9.

decay to a double negative ion with two holes in valence band. In correspondence to the LUMO+1 or LUMO the situation is changed. The photon excites a transition to a molecular orbital (and not to the vacuum as in the previous case), and the molecule is in a neutral overall state with a core-hole, decaying through Auger (both participator and spectator, but we are looking at the spectator shifts) into a singly charged negative ion with a vacancy in the valence levels. The Auger peak shows a clear spectator shift of 0.9 eV as highlighted by the inset in the RESPES figure. The excitation to IMO (photon energy 532.3 eV) leads to a situation similar to the spectrum above the edge. This result demonstrates that the electron promoted to the IMO is allowed to delocalize to the substrate before the de-excitation takes place, so that the decay process is the same as for excitations above the edge when the electron is ejected in the vacuum. This result depicts the presence of an interesting channel for ultra-fast electron delocalization between the boroxine system and the substrate.

2.6 FINAL OVERVIEW ON PBA

The on-surface synthesis of boroxinated molecules from boronic precursors represents a valuable route to the formation of complex organo-metallic interfaces. The specific case we present, the synthesis of TBA, allowed to characterize the boroxination process and to describe the electronic properties of the boroxine-Au interface. We have gained a deeper understanding of the electronic structure of the system thanks to a theoretical inquiry well supported by experimental data, leading to the attribution of the NEXAFS peaks to specific and well-defined transitions between orbitals. More importantly, we have discovered that there is an ultra-fast charge delocalization channel at the boroxine-Au interface, localized on the Au atoms. This information is of crucial importance for the study of boroxine based systems because it opens to their possible use as charge transport mediators between electrodes and guest molecules adsorbed on top.

2.7 1-NAPHTYLBORONIC ACID (NBA) ON AU(111)

The interesting findings on the triphenylboroxine (TPB) raises the question on the generality of the condensation reaction among different boronic acids. In particular, it has to be kept in mind that a reaction performed on a surface in UHV condition is competing with desorption of the reactants. In our case, we are forming bigger molecules, starting from smaller precursors, that can be supposed to desorb at lower temperatures than the product. So, any effect that can enlarge the thermal barrier for the reaction can prevent completely the formation of the products on the surface. The steric effect can play this role on the reactant molecules. For that reason, we decided to investigate the behavior of a different monomer, with a bigger carbon backbone. From a phenyl ring we passed to a naphthyl one employing the 1-
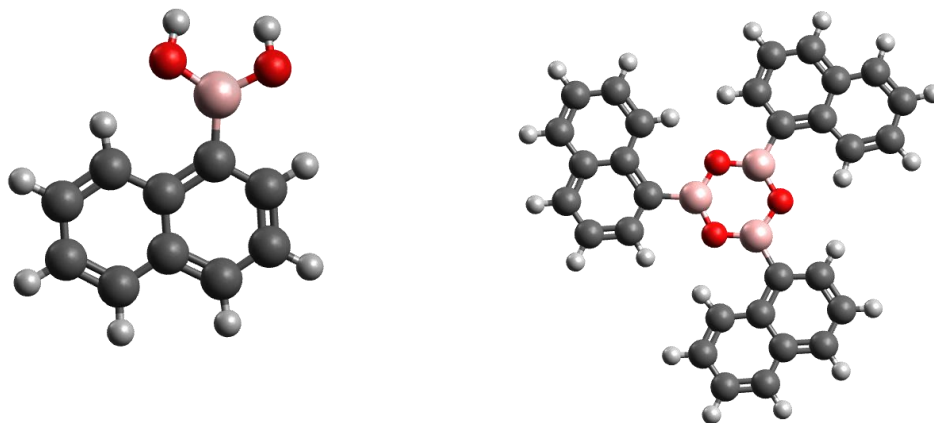
Figure 8: On the left the model of the 1-naphtylboronic acid (NBA), on the right a model of the possible condensed trimer, the trinaphthylboroxine (TNB)

naphtylboronic acid, reported in figure 8. In a general perspective, enlarging the aromatic parts pushes the system to adsorb into the visible region and makes these materials interesting for applications where this optical absorption is a key property. In this perspective, the boronic functionality can serve to link different aromatic molecules in a precise and reproducible way.

2.8 EXPERIMENTAL SECTION NBA ON AU(111)

The experimental conditions adopted for studying the NBA were similar to the PBA ones. The gold substrate was cleaned before use with sputtering and annealing cycles and the presence of contaminants was checked by XPS. The deposition of 1-naphtalenboronic acid (Sigma Aldrich, 97% of purity) has been achieved from a crucible heated to 330 K connected to the chamber through a gate valve. The sample has been held at room temperature to obtain the monolayer in the ANCHOR chamber, while the multilayer has been obtained depositing at 200 K. In the OSMOS STM chamber the monolayer was obtained depositing on the sample held at 330 K.

2.9 RESULTS OF NBA ON AU(111)

The main question to answer during the study of the NBA molecule alone concerns the influence of the different carbon backbone on the assembly. For such a purpose an STM investigation has been performed on the molecule deposited on the Au(111) substrate. Interestingly, there are three distinct phases that
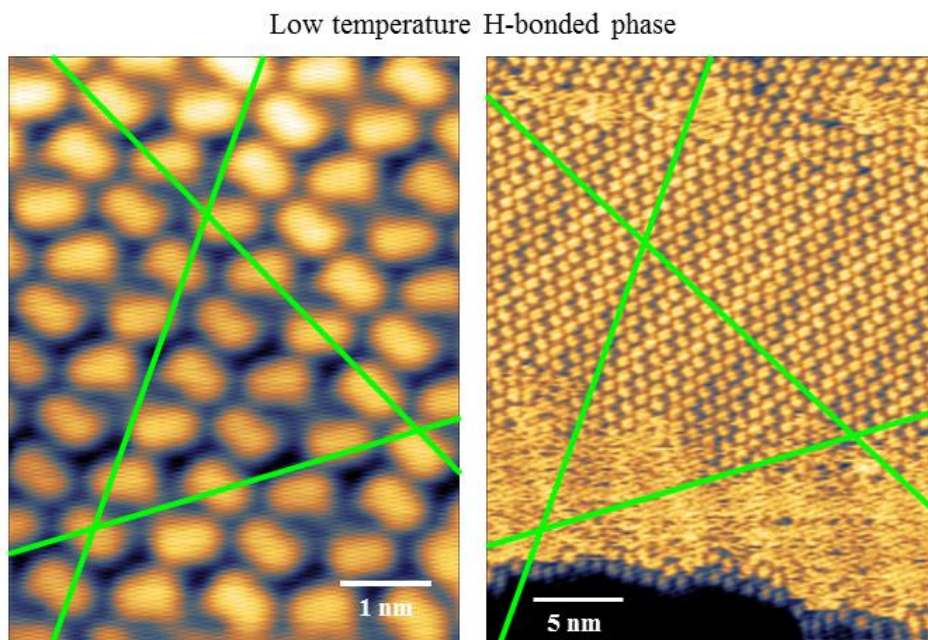
Low temperature H-bonded phase

Figure 9: STM image of the low temperature phase. The green lines report the symmetry directions of the Au(111) surface. The acquisition parameters for the first image have been 1.25 V and 0.21 nA, whereas for the second -0.97 V and 0.24 nA

Intermediate temperature phase
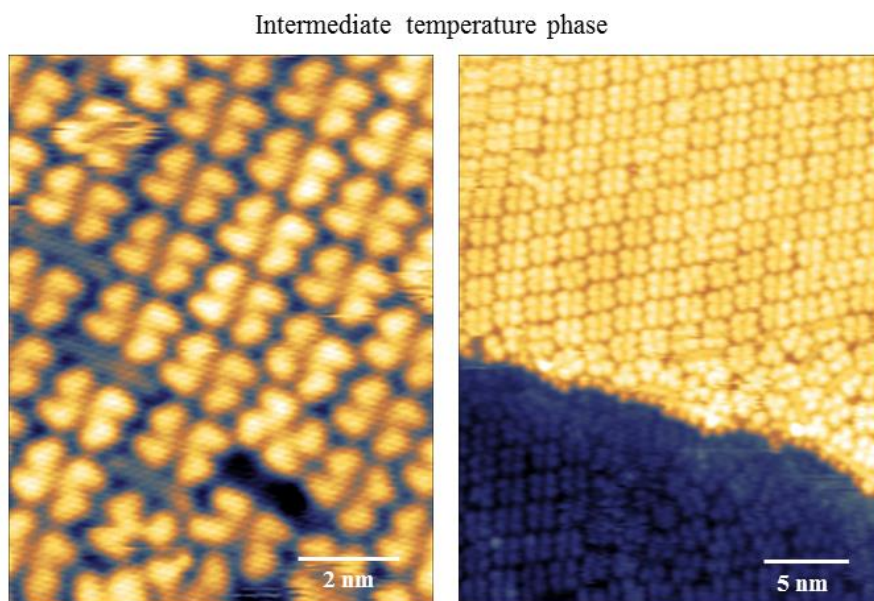
Figure 10: STM image of the intermediate phase obtained depositing PBA at 270 K. The molecules do not align along the symmetry direction of the substrate. Both images have been acquired with a bias of 0.94 V and a current of 0.22 nA.

Covalently bonded phase
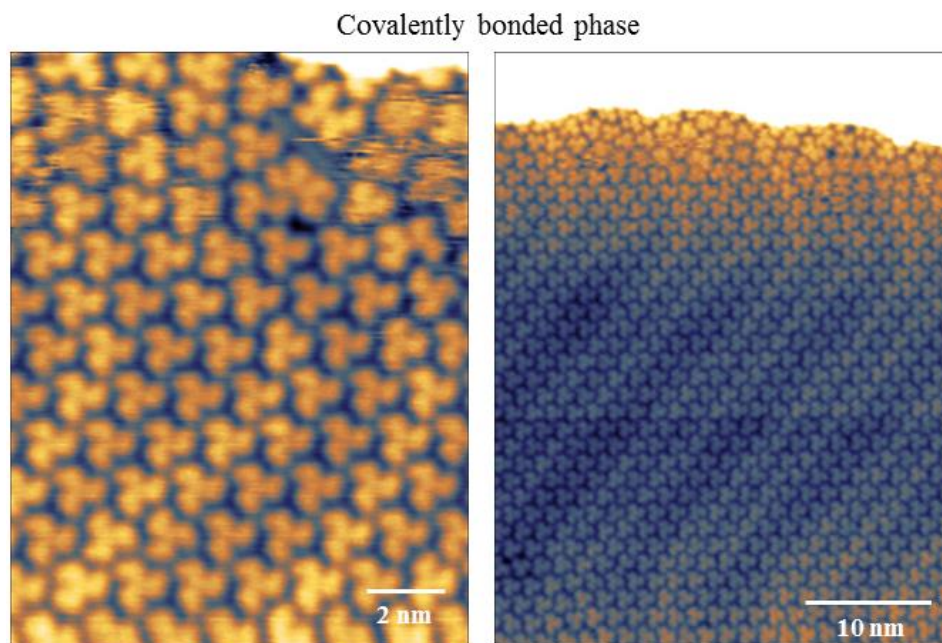
Figure 11: STM image of the triphenyl boroxine, formed after the condensation reaction of the NBA molecules. The first image has been collected with a bias of 1.4 V and a current of 0.21 nA, the second one 1.40 V and 0.2 nA

the molecular layer forms on the substrate, and their occurrence is showing a clear temperature dependence. The deposition at low temperatures (255 K) led to the formation of loosely linked tetramers interacting via H-bonds reported in figure 9. This is the only phase that align in the symmetry direction of the substrate beneath. Instead, deposition at room temperature has produced a different phase, figure 10, where the molecules are arranged in tetramers of different shape with respect to the previous one, in particular most of the surface is covered by tetramers that occasionally are split in dimers, whereas there are no single molecules. It is not trivial to state if there is only the H-bonding in this phase, or if there is a covalent bond holding together the dimers. Deposition at sample temperatures above 330 K led to the formation of trimers, named trinaphthyl boroxine (TNB) in the same fashion as triphenyl boroxine (TPB), as reported by figure 11. We have followed the formation of monolayers by STM as a function of temperature. We have observed two H-bonded phases at lover temperature, and a boroxinated phase at higher T. Interestingly, the boroxination reaction cannot be obtained by heating, starting from H-bonded phases and a general de-wetting of the substrate is observed. Tentatively we suggest that this phenomenon is due to H-bond constraints that hold the molecules in position not suitable for the boroxination reaction. After each deposition it has been necessary to cool the sample again to 140 K with liquid nitrogen to prevent the quick diffusion on the surface and this indicates the high mobility of the various species. The condensed trimers order along the herring bone pattern of the gold beneath. From the spectroscopic point of view, the TNB has shown a quite similar behavior to the smaller TPB. The monolayer has been obtained with a deposition at a temperature of the substrate of 320 K. The peak positions of the monolayer lie in the same position as for the TPB. The spectroscopic data, together with the STM images have made us confident to state that the boroxination reaction has taken place on the surface. Thanks to the study of TNB, it is possible to point out that XPS seems to be an appropriate and
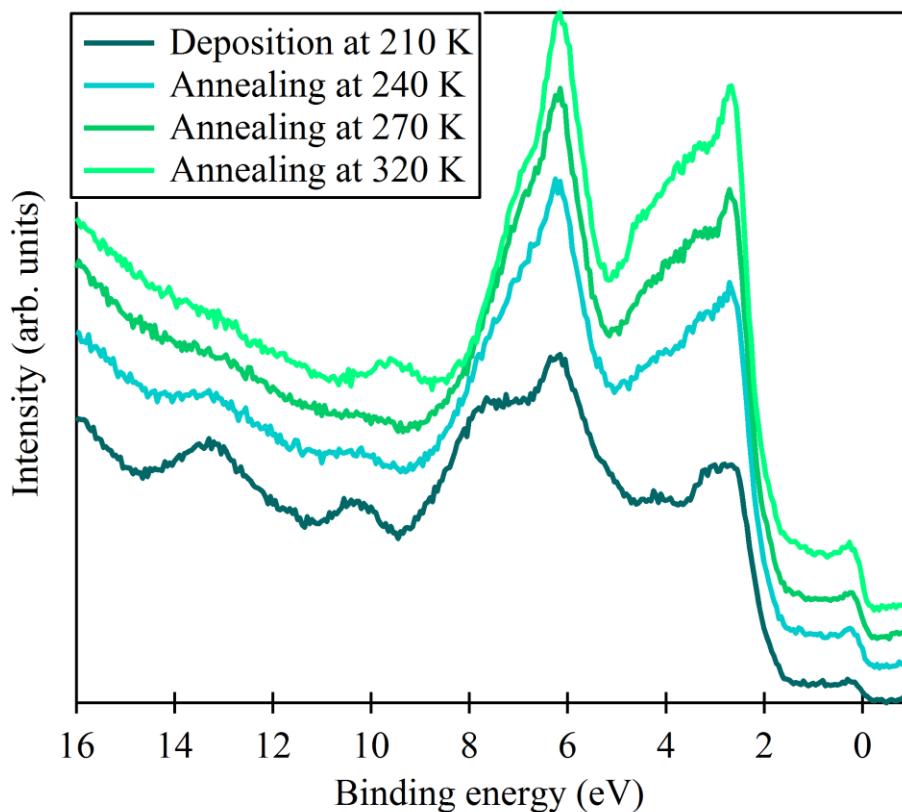
Figure 12: UPS NBA, the dark blue line represents the thick film, which has been annealed to the temperatures reported in the legend. The light green line is the spectrum of a boroxinated layer with its typical peak around 10 eV. The spectra have been taken employing the He(II) spectral line with a pass energy of 10 eV.
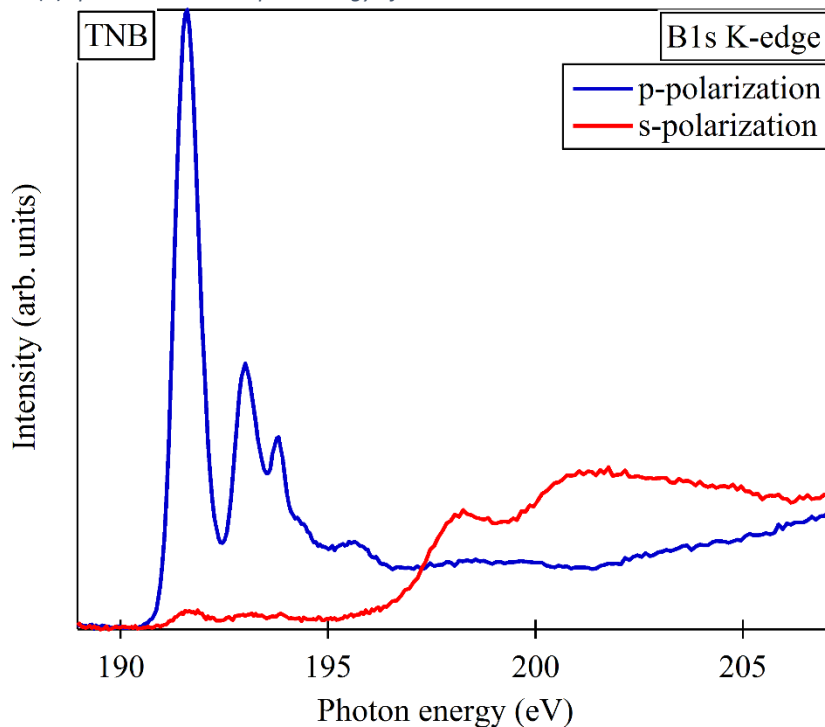

Figure 13: NEXAFS of the trimers of NBA on Au(111). The experimental NEXAFS signal have been acquired in partial electron yield, with a cutoff at 150 eV. The overall resolution is 100 meV.

quite general tool for investigating the presence of boroxine. On the other hand, this technique has

demonstrated not to be able to detect clear differences between the two low temperature H-bonded phases imaged by STM. In contrast, UPS has been able to follow the evolution of the spectrum as a function of annealing temperature, and it has been possible to detect clear changes in the valence band. From the shape of the spectrum of the system obtained after the deposition, the signal is exhibiting a characteristic peak, that will be seen also in the next system, at a binding energy slightly less than 10 eV. UPS provides a better insight in the changes on the surface, even if it is of little help in determining the nature of the bonds, especially in absence of a theoretical simulation. All the employed techniques STM, XPS and UPS came to the agreement that at 320 K there are condensed trimers on the surface, indicating a certain generality of this condensation reaction. The interpretation of NEXAFS spectra of the TNB, figure 13, has been made by comparison with the PBA one taking advantage of the similarity between the two systems. The dichroism between the p and s polarization confirms a flat deposition geometry.

2.10 BOROXENE: A NOVEL 2D MATERIAL?

The study of boroxine based 2D systems has evidenced the problem of scarce in-plane electron delocalization of these materials. Theoretical inquiry has attributed it to the low aromaticity of boroxine compared to the carbon backbone that contains (carbon based) aromatic rings.[40,41] On the other hand, with the PBA study we have demonstrated the existence of a possible charge transfer channel connecting the oxygen atoms of boroxine to the gold beneath. In this context, we have decided to investigate the behavior of the tetrahydroxidiboron (THDB), depicted in figure 14. This simple molecule contains no carbon atoms and the spacing
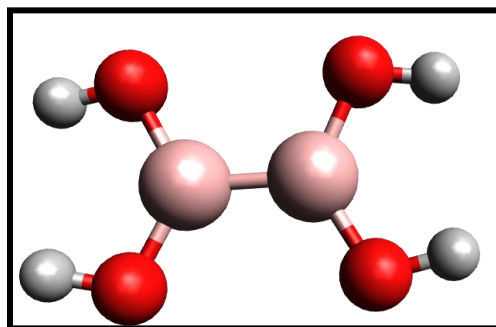

Figure 14: Tetrahydroxidiboron molecule

between the two boronic groups is only a boron-boron single bond, or it can be said that THDB is composed by two linked boronic functionalities. The condensation reaction of this molecule leads to the formation of a boron monoxide (BO) layer. The BO, unstable as a molecule, exists as a polymeric bulk material, $(BO)_x$ and has already been investigated for its structure.[43–47] There are no doubts that the B-B bond is conserved[48] but the exact structure is still matter of debate. Theoretical inquiry, well supported by Nuclear Magnetic Resonance (NMR) performed in solid state, has revealed that many energetically equivalent structures exist with different BOB angles, but very similar bonding distances.[49] However it has to be taken in mind that NMR has evidenced the absence of BO_3 subunits. The synthetic routes reported in literature toward the $(BO)_x$ comprehend the condensation reaction between THDB molecules, hydrolysis of B_2Cl_4 or $B_2(NMe_2)_4$, or high temperature reaction of B_2O_3 with elemental boron. Moreover, the theoretical approach of Zhang et al. proposes a new path with boronyl group containing molecules.[50] We propose here an alternative synthetic path of BO material, limited to the 2D case. We intended to form a phenyl-free, surface confined, 2D covalent framework having the electronic properties of the afore mentioned boroxine systems. In other words, we will describe here a protocol we defined for the synthesis on surface of an extended network of boroxine rings. The main goal of this study is to verify the possibility of taking advantage of the tunability in morphology typical of boronic COFs and of the electronic

properties of electron delocalization toward the substrate that we have found for PBA. The choice of the substrate is also a key issue. We have decided for Au(111) not only for consistency with the previous data, but also for its low interaction level, thus leaving the THDB to organize undisturbed as much as possible. Moreover, for comparison, we have also employed Cu(111) to have a comparison with a more reactive surface.

2.11 EXPERIMENTAL SECTION

The Au(111) was cleaned by multiple cycles of sputtering and annealing. The THDB was purchased from Tokyo Chemical industries, with purity of 95%. It has been deposited from a crucible heated to 340 K and, in the same fashion as the previous PBA, the sample was held at ambient temperature for the monolayer and cooled at 230 K for adsorbing more layers on the metal.

2.12 RESULTS OF THDB ON AU(111)

The XPS technique demonstrated once again its ability of revealing the occurrence of the condensation reaction, as reported in figure 15. We have proceeded as in the PBA case measuring the thick film obtained by depositing on a cold sample (200 K) and the monolayer obtained after a deposition in the range of 300 - 450 K (reaching the saturation limit). The comparison of the two data sets in this case cannot take advantage of the presence of an element not involved in any chemical reaction as the carbon in the PBA (or better Triphenyl boroxine, which is the state the system was probed in). The shift of O1s towards lower binding energies is large, 1.5 eV, and probably it includes the chemical shift and the mirror image effect. This value should be compared with the absolute change in energy of the O1s of TPB (triphenylboroxine,
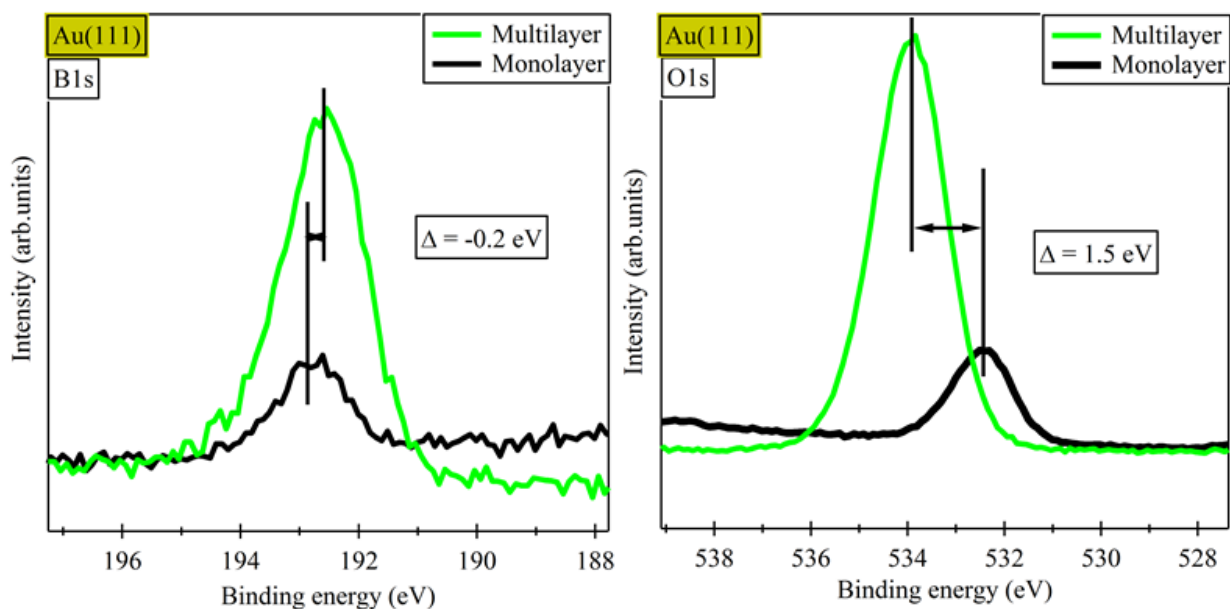

Figure 15: XPS analysis of the THDB films on the Au(111) surface. The multilayer is in green and the black line in both B1s and O1s is the spectrum of the monolayer coverage. Both signals are referred to the same bottom scale. The multilayer is composed by unreacted THDB molecules, whereas the monolayer is constituted by the boroxene, and the reaction releases three molecules of water, which are removed by the vacuum pumping. The spectra have been taken with a laboratory X-ray source with Al Kα monochromatized light, with a pass energy of 20 eV. The peak position has been calibrated with the substrate Au4f$_{7/2}$ at 84 eV.

the PBA-based film of trimers weakly interacting between them and with the substrate) in its analogue XPS experiment, which was of 0.83 eV, a largely lower value. The B1s peak confirms the larger shifts present on the THDB with respect to the PBA, moving by 0.2 eV toward higher binding energies (opposite direction than oxygen). In this case the difference with PBA is even more striking, because the B1s peaks in this molecule was shifting in the opposite direction before the charge image correction, with a difference of 0.8 eV between the shifts of the two molecules. Furthermore, the difference between the two systems created from THDB and PBA, is highlighted by difference in the absolute positions of the monolayer peaks. The B1s positions are 191.23 eV and 192.81 eV for PBA and THDB respectively. This significant difference can be understood by invoking the different environment of the boron atoms in the two cases. In the film created from the condensation reaction of THBD the B-B bonds are still present while the TPB has a B-C bond with an aromatic carbon involved. There is also a minor change in the binding energies of the O1s peaks, 532.22 eV in the PBA system and 532.41 eV in the THDB based film. It has to be considered that major differences are present already at the multilayer coverage, indicating that the unreacted molecules are substantially different for the two systems. On the other hand, the change in the relative intensities between the B1s and O1s shows the occurrence of the reaction and resembles the result on the PBA film. The formation of a network has been confirmed by STM images, reported in figure 16.
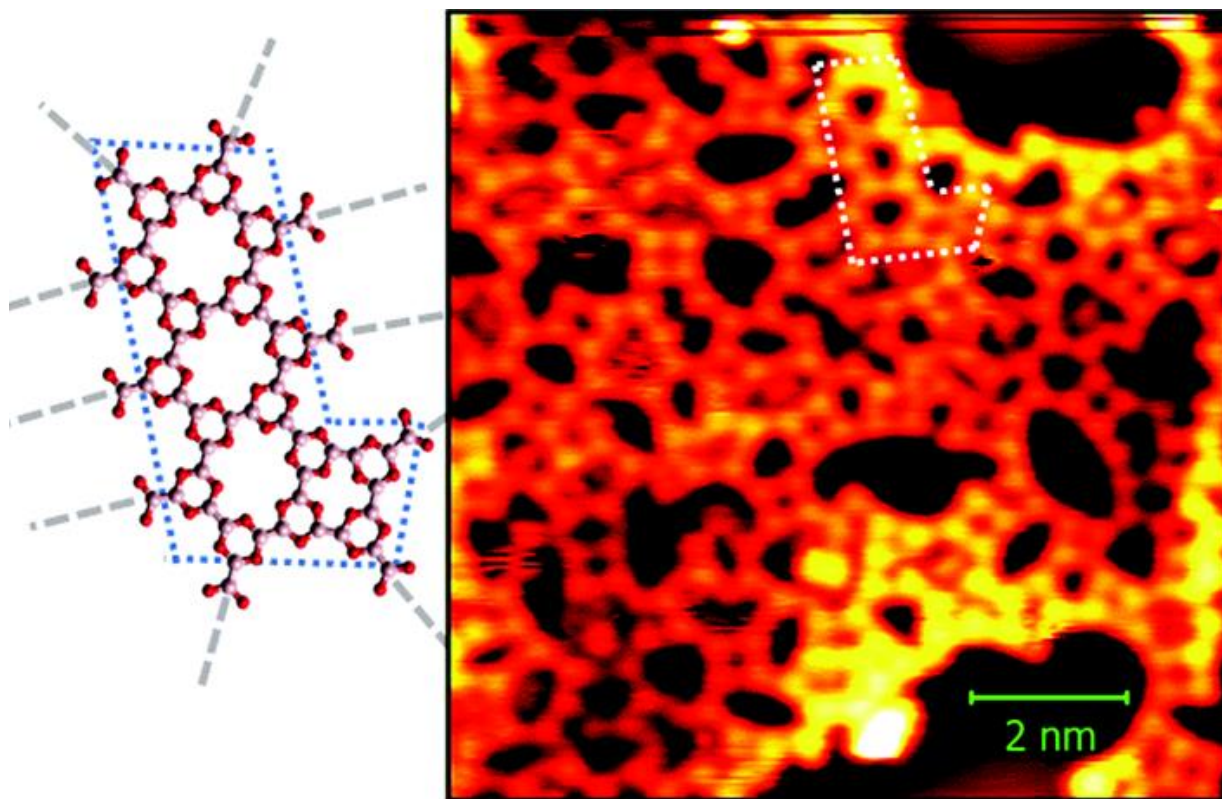

Figure 16: STM image of boroxene. The overall disorder resembles a vitreous material, every dot is a boroxine ring, in the inset on the left part. (Tsample = 77 K, V = 1 V, I = 1.5 nA). adapted from ref 10

The overall picture of the system obtained from STM consists in a framework of bright spots linked to form various geometrical shapes. Since there is evidence of a condensation reaction, we attribute the bright spots to the boroxine rings that are linked on the surface. The connection pattern of these
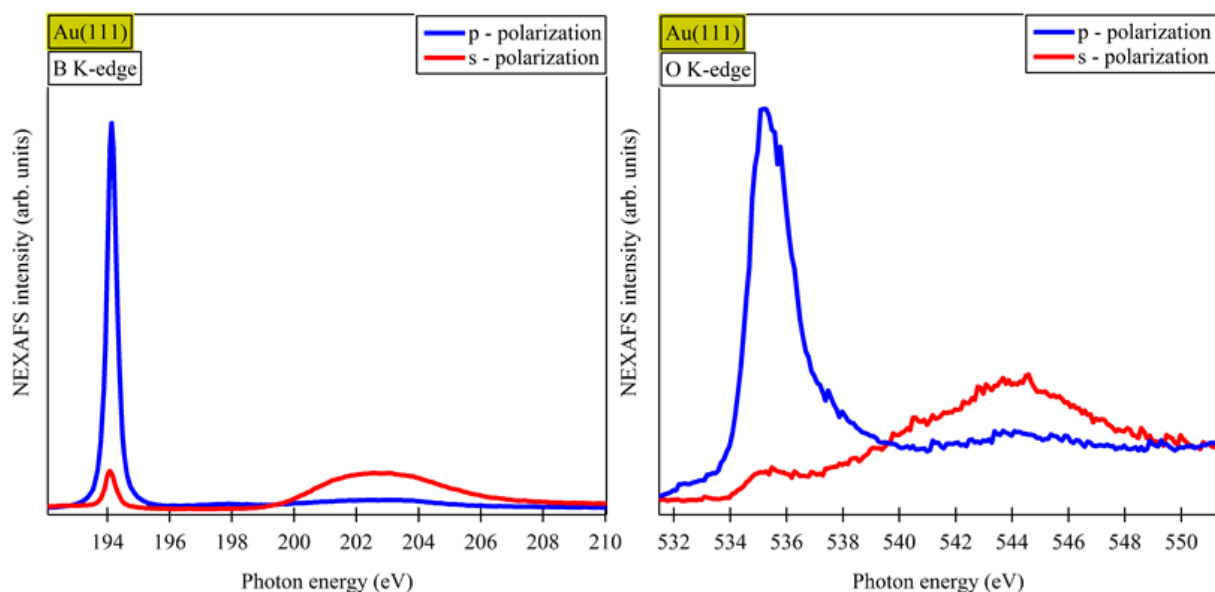
Figure 17: NEXAFS spectra of the boroxene. Dichroism can be seen for both the edges. The boron signal shows a very intense and narrow peak in the p-polarization, indicating an energetic equivalence of the boron in different geometries on the surface. The oxygen p-polarization shows again a shoulder at low photon energies. The spectra have been acquired in Auger yield, for boron at 163 eV of kinetic energy, while for oxygen at 507 eV. In both cases the pass energy of the analyzer was set to 50 eV.

boroxines is irregular: there is a proliferation of different connection geometries and nanopores with no long-range order. In fact, the larger scale appearance resembles 2D vitreous silica films.[51] Among the recurrent connection geometries, there are the 6-fold and the 4-fold boroxine patterns, even if they are not predominant. In addition to the XPS information of changing B/O ratio, the covalent nature of the film is evidenced by the thermal stability up to 450 K before the start of desorption. It is probably this covalent nature to impose a certain rigidity to the film; indeed, the STM images have been acquired at relatively higher temperature (70 K). The general flatness of the boroxine network is confirmed by the partly dichroic NEXAFS spectra, both in O K-edge and B K-edge, figure 17. In p-polarization both thresholds show an intense peak due to a transition to a π^* orbital with an almost featureless part at higher photon energies. Vice versa, the s-polarization shows only a small contribution of the first transition to the π^* unoccupied orbital, followed by broad structure at higher energies. Despite the evident dichroic behavior, it should be noticed that it is not as high as in the TPB experiment. The explanation could be that not all the boroxine rings of the boroxene film stand flat on the surface, or there is a systematic small tilt angle between the boroxines and the substrate surface. Another qualitative explanation for this reduced dichroism could be that, especially in absence of a theoretical calculation to attribute transitions to peaks and shapes to orbitals, a hybridization of the MOs due to interaction with the substrate may cause a reduced dichroism for the first peak even for a perfectly flat boroxene film. The comparison of the NEXAFS peak positions between TPB and boroxene evidence again how the systems differ. Starting from the main features of O K-edge, the TPB presents two intense transitions in the p-polarization at 533.8 eV and 536.7 eV photon energy, while boroxene has only one peak at 535.3 eV. An analogous situation can be found for B K-edge spectra. The TPB presents two peaks (192.1 and 194.2 eV) that in the THDB based film reduce to one single feature at 194.2 eV. The strong difference between the films (the reduction of the peak number and the change in position) can be ascribed to the absence, in THDB, of the carbon atom bonded

to boron. Indeed, the DFT calculations revealed that both the peaks in the O and B edges of TPB are transitions to unoccupied orbitals that, in LCAO orbital view, have a strong composition of $C2p_z$ atomic orbitals. Moreover, the oxygen K-edge NEXAFS signal presents a broader feature at approximatily 533 eV photon energy. This feature can be interpreted as a proof of the existence of the ultrafast delocalization channel for charges, as it was for the PBA boroxine system. Besides the comparison with prototypical
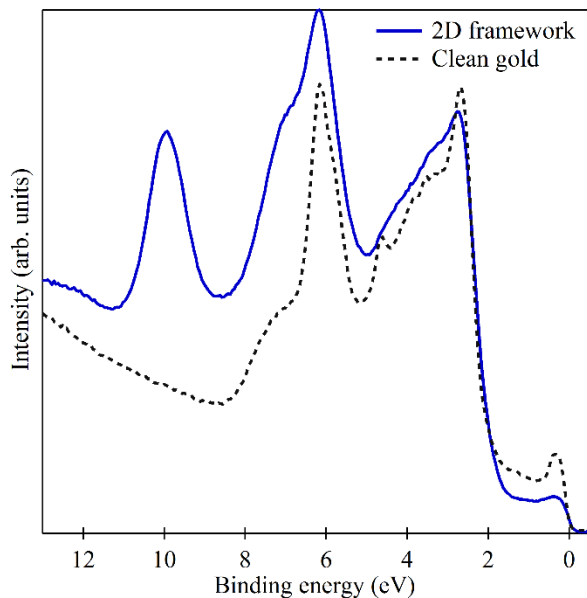

Figure 18: Valence band of the boroxine film compared with the clean gold substrate. The spectra have been taken with non-monochromatized helium discharge lamp, employing the He(II) spectral line, the pass energy was set to 10 eV. adapted from ref 10.
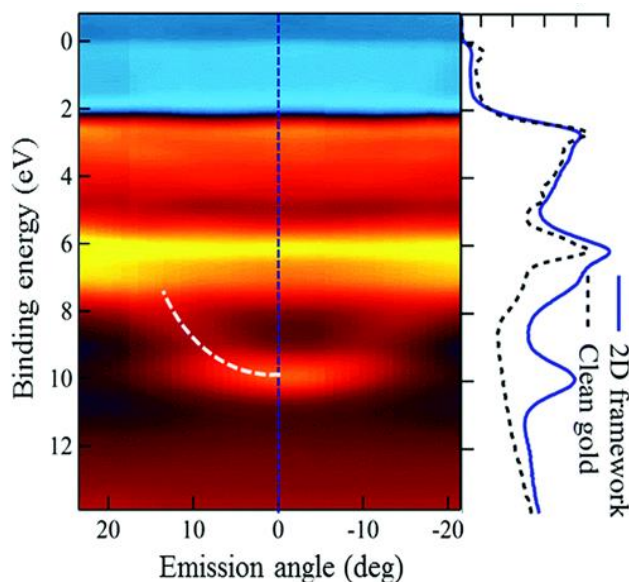
Figure 19: Angular Resolved ultra-violet Photoemission Spectroscopy map of boroxene, the white line evidences the band dispersion. The map has been normalized for signal above 12 eV of binding energy to take into account the different overall intensities at different angles. On the right, two scans, one of the molecular film taken at normal emission (corresponding to 0° angle in the map) and clean gold signal. The spectra have been taken with non-monochromatized helium discharge lamp employing the He(II) spectral line, the pass energy was set to 10 eV. adapted from ref 10.

systems, the NEXAFS of boroxene is very interesting for the very sharp peak in the B K-edge spectrum acquired in p-polarization. In particular, while STM reveals a non-homogeneous morphology, resembling a vitreous like situation, NEXAFS instead is characterized by a single and narrow resonance at around 194 eV. This indicates that the boron atoms, in whatever geometry on the surface, can be considered to be in a similar chemical environment. To have a better understanding of the system we have also acquired valence band spectra, reported in figure 18. We have chosen the peak at 10 eV from the Fermi level for monitoring the presence of boroxine, for its distance from the features of clean gold. Interestingly, this peak shows an angular dispersion despite the defects seen in the STM images, as reported in figure 19 and evidenced by the white line. Indeed, there are other peaks at lower binding energies that show dispersion, but they lie in a region where there is a strong signal coming from the substrate (and also these peaks present band dispersion making the disentanglement the different contributions difficult). By analogy with graphene where also a characteristic peak at 10 eV from Fermi is present in UPS spectrum indicating the presence of a 2D valence band, we have called this novel material "boroxene". In order to clarify the nature of the orbital at 10 eV from the Fermi level, we have also measured the valence band in
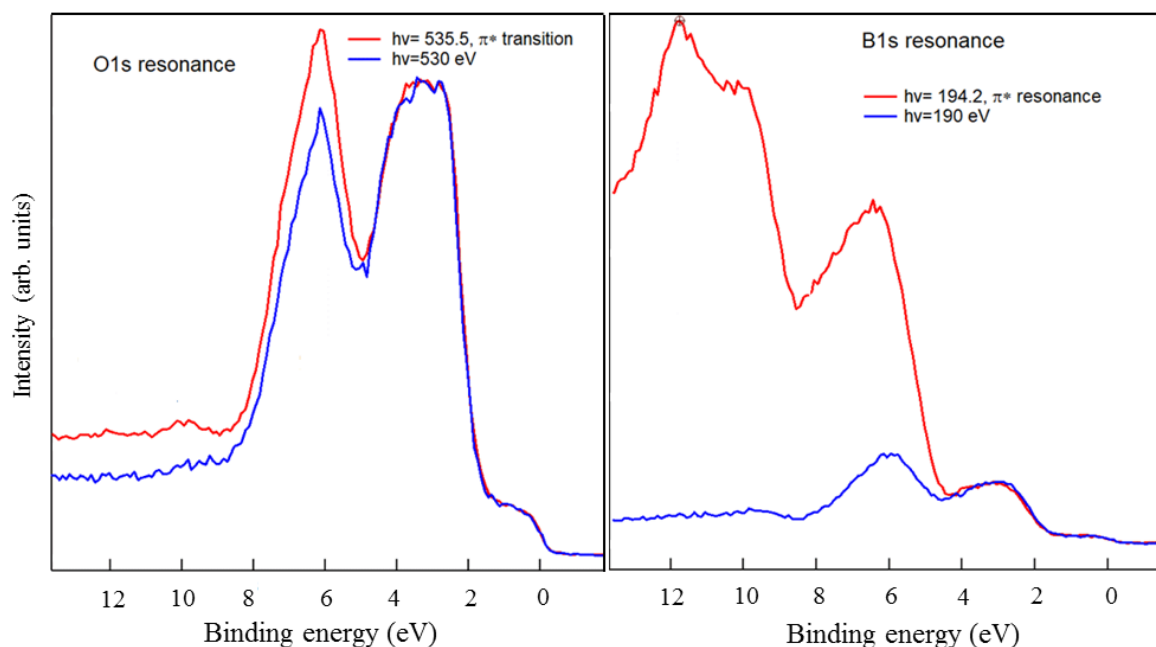

Figure 20: Valence band measured at resonance, red line, compared with valence band off resonance, blue line. At low binding energies, the spectra are equal because there is no molecular orbital, only features from gold. The overall resolution of the spectra is of 0.2 eV. taken from ref 10

resonant conditions, with the photon energy of the two strong π^* transitions of the NEXAFS, 194.2 eV for boron and 535.5 eV for oxygen (in practice two lines of the RESPES map, taken exactly on the main resonant features, reported in figure 13). The comparison with the valence band taken off resonance highlights the peak at 6 eV masked by the substrate features. Moreover, it is possible to state that the peak involved in the dispersion has a contribution from both the boron and the oxygen atoms. It has to be considered that the band dispersion indicates the presence of delocalized electronic states, which are of key importance for the in-plane electron transport.

2.13 IMPROVEMENT OF BOROXENE MORPHOLOGY

A more careful look at the single ARUPS map reveals that there are two components for the monitored peak. In particular, the feature showing dispersion is split into two components, one is changing in energy at least up to 8 eV, the other one lies almost unchanged at 10 eV. A possible explanation is that only the locally ordered portions of the framework possess delocalized states and contribute to the component that shows dispersion, whereas the defective rest of the network contributes to the second, non-dispersive, component of the peak. We have proposed an ideal structure for boroxene, where the boroxine rings are arranged in bigger hexagons. This structure is consistent with the usual bonding angles of boron in sp^2 configuration (120°) and the boroxine-based COFs reported in literature even if the absence of a carbon-based backbone and the presence of different geometries evidence the need of a theoretical calculation. In this perspective, it gains importance to study how to improve the morphology of the film. It is known that in solution environment the morphology is improved by the presence of water.[39] It is due to the fact that boroxine formation, the fundamental reaction that forms the framework, is a reversible reaction and in presence of water the boroxine rings are in equilibrium with the boronic acid molecules. In these conditions the framework formation has the possibility to correct defects and thus to reach a structure closer to the ideal one. In our conditions UHV prevents the equilibrium to be
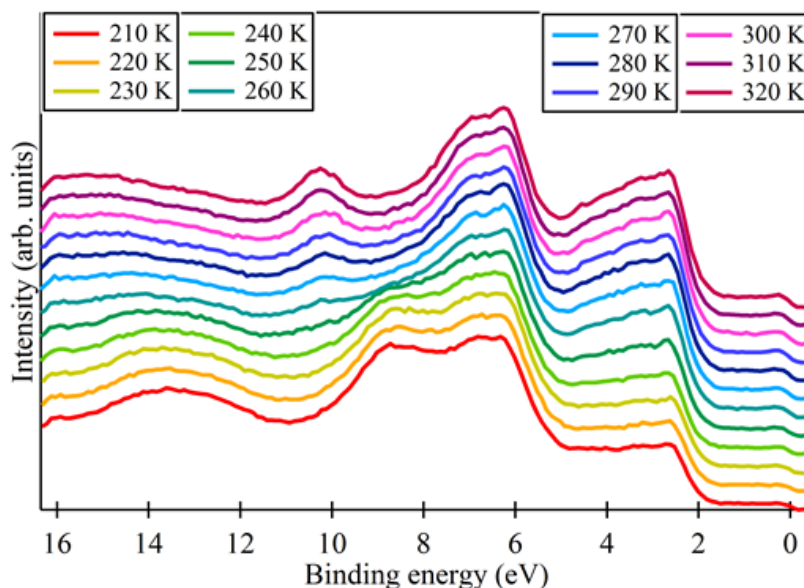

Figure 20: Temperature study of the film of THDB. First changes start at 250 -260 K, and then evolves in boroxene. The increase in temperature has been slow, 2-3 K/min and the temperature has been left almost constant during the acquisition of the spectra, taken with the He discharge lamp, using the He (II) non-monochromatized spectral line. The pass energy has been set to 10 eV.

reached and the film presents a proliferation of defects. A post processing performed dosing water in the experimental chamber up to a pressure of $5*10^{-5}$ mbar has led to only marginal improvements. In particular, at lower values of water pressure, there is no appreciable change, while an only slightly higher
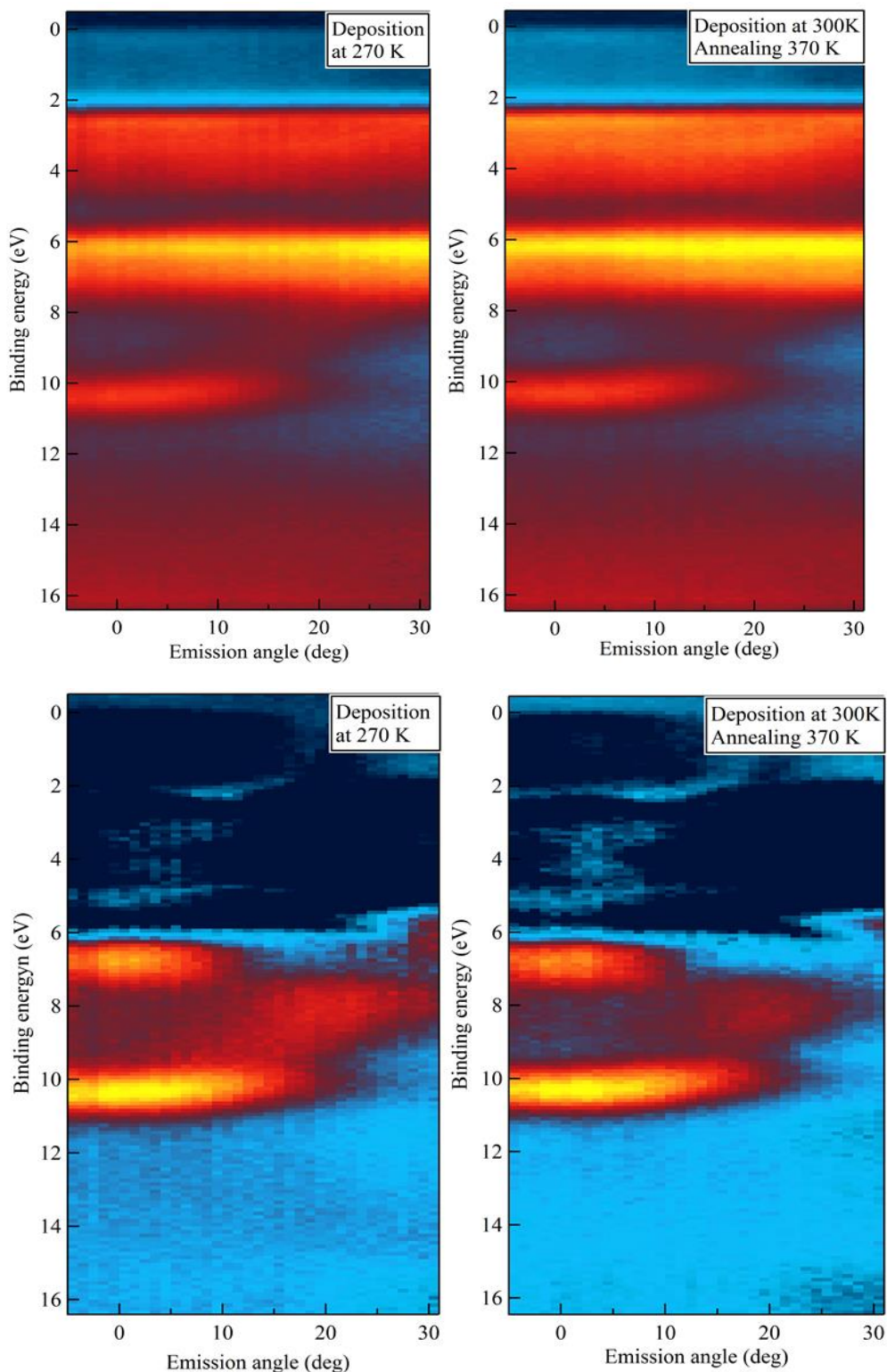
Figure 21: the upper two ARUPS maps compare the film grown on a sample at 170 K with a room temperature grown one. The maps are normalized to the signal above 12 eV. The lower maps are obtained subtracting from the upper ones the signal of the gold substrate. To make possible the comparison, they have been equalized on intensities of the peak around 10 eV.

concentration of water promotes the desorption of the film, pointing out the elevate instability of boroxene in presence of water. Provided the difficulty of changing the morphology of the framework with

a post-production treatment, we have explored the effect of slowing down the reaction. The temperature at which the condensation reaction is taking place has been identified by depositing a multilayer (there was no interest in making an extremely thick film, because all the layers except the first few are regarded as irrelevant for this experiment, since they desorb at lower temperature than the boroxine formation takes place) on the cold sample, 180 K, and monitoring the valence band while increasing the temperature. The results are reported in figure 20. The film deposited at this temperature does not show any feature at 10 eV from the Fermi level indicating that the condensation reaction has not occurred yet. The first changes are registered at 220 K where desorption of the over-layer takes place leaving a monolayer coverage, or slightly higher. Between 250 K and 260 K the typical peak at 10 eV from the Fermi level starts growing ad from 270-280 K it is present and not changing any more. This result implies that the condensation reaction is taking place at these temperatures. The subsequent step toward a better morphology has been a slow deposition on a sample held at 270 K. Interestingly, the dispersion of the peak at 10 eV of binding energy is affected by this different growth method showing a more defined shape in the 2D plot when grown at low temperature. This result can be observed comparing the ARUPS maps, as in the top part of figure 21, but to highlight better the difference it is possible to subtract the gold signal from the maps after invoking the low level of interaction of this surface, as reported in the bottom part of the figure 21. The effect of improving morphology due to low temperature deposition persists upon annealing at 300 K, but a thermal treatment at 340 K or higher, restores the situation of lower dispersion of the films grown at room temperature. The thermal instability of the change in the dispersion points out that probably the film undergoes a damaging that is simply more evident in the better grown framework. On the other hand, it is also necessary to point out that there is a small difference in the binding energy of the dispersing peak of the 270 K film with respect to the room temperature one. Further STM measurements will be necessary to fully understand the morphologic differences in the two cases.

2.14 Boroxene on Cu(111)

We studied the behavior of the tetrahydroxydiboron molecules also on a more reactive substrate such as copper. The aim of this investigation is to explore the strong interaction regime and its influence on the covalent framework formation. Moreover, we expect to find an electronic structure rather different from the one of the film grown on gold. We have proceeded in the same fashion as with the previous golden substrate. We have started with XPS measurements, figure 22, of the multilayer and the monolayer to gain evidence of the reaction. The results resemble THDB on gold: the peak positions are similar and the shifts between the two coverages are in the same direction. For multilayer this result was expected as the layers contributing to the signal are distant from the surface and do not experience the influence of the substrate in a strong way: the B1s peak lies at 192.5 eV and O1s at 533.9 eV, whereas on gold the positions
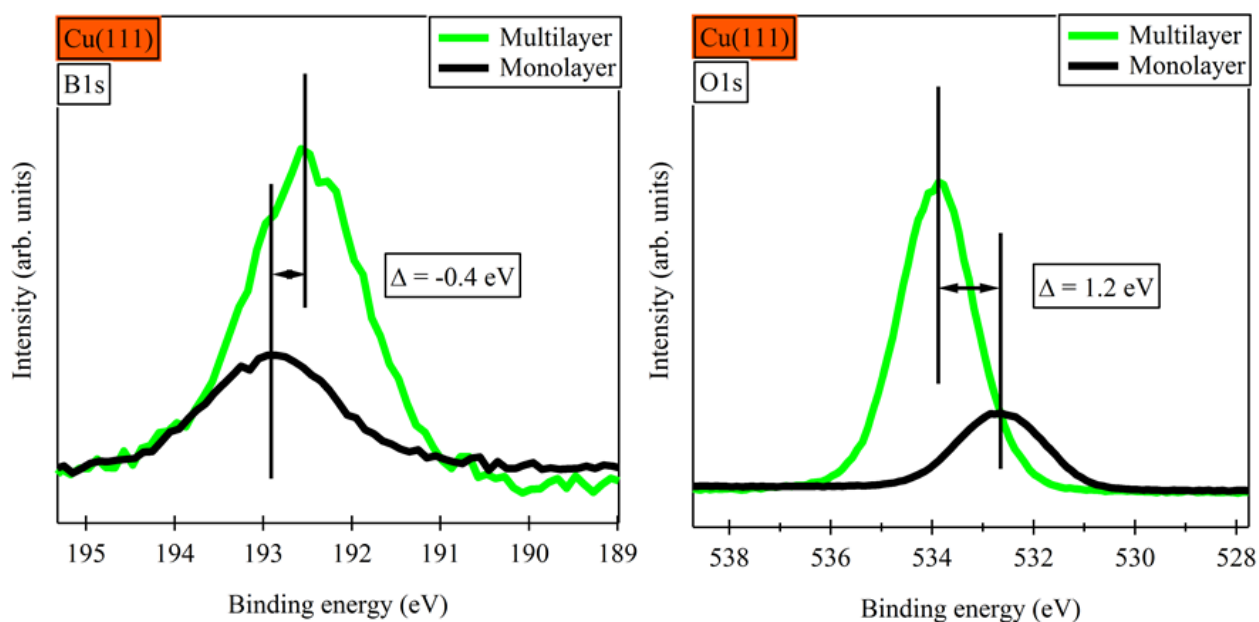

Figure 22: XPS of the multilayer, black line, of THDB and monolayer of boroxene, green. The peak positions and the shifts resemble the situation on gold. The peak position has been calibrated with the substrate $Cu2p_{3/2}$ at 932.8 eV. The spectra have been taken with laboratory X-ray source with Al Kα monochromatized light, with a pass energy of 20 eV.

are 192.6 and 533.9 eV. Less obvious, and less exact, are the correspondences measured at monolayer coverage. The B1s peak has a binding energy of 192.9 eV (192.8 eV on gold) and O1s 533.7 eV (gold: 532.5 eV) resulting in a larger shift between the two coverages on boron, -0.4 eV, and a less pronounced one for oxygen, 1.2 eV, but the sum of the two shifts remains only slightly changed. The results of the XPS measurement suggest the occurrence of the condensation reaction in a similar way as on the Au(111) surface. The first substantial differences between the two substrates emerge in figure 23 where the NEXAFS spectra are presented. The overall appearance of the spectra remains unchanged, but they are markedly less dichroic. The explanation can reside in a different geometry on the surface of the film (the NEXAFS technique is not able to state if all the molecules have the same, not flat orientation, or if there are some molecules in a different orientation among other flat molecules), even if boroxinated, and the boroxine should have a planar shape. Another explanation can rely on the fact that the highly interacting
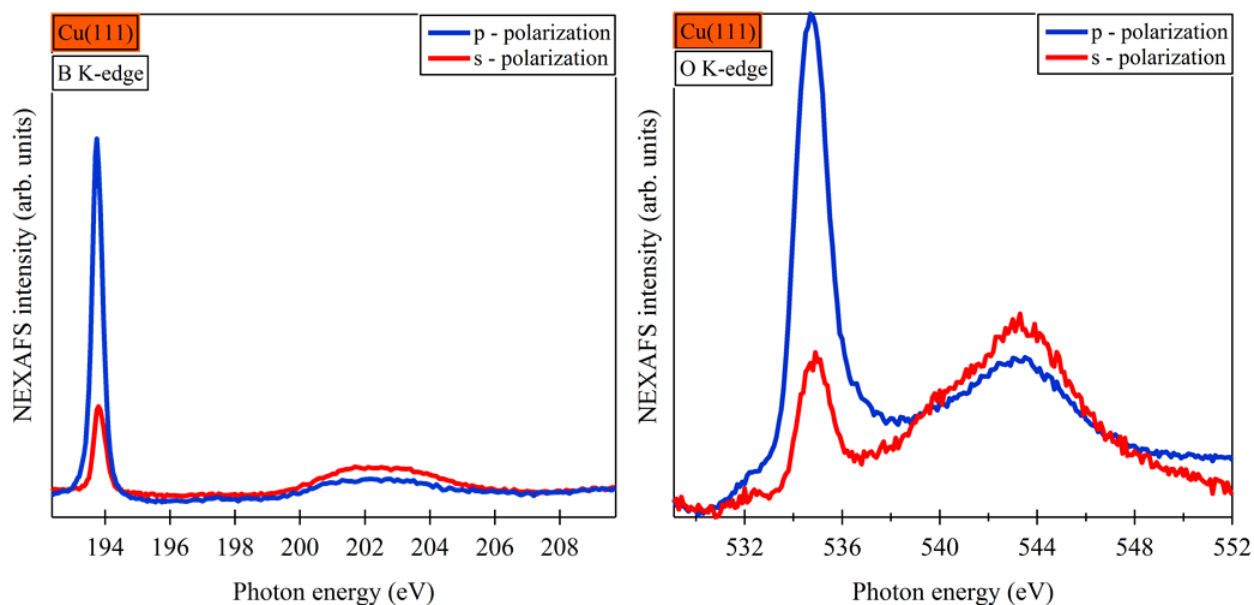
Figure 23: NEXAFS spectra of the film of THDB molecules on Cu(111). The oxygen p-polarization shows again a shoulder at low photon energies. The spectra have been acquired in Auger yield, for boron at 163 eV of kinetic energy, while for oxygen at 507 eV. In both cases the pass energy of the analyzer was set to 50 eV.

copper surface may induce major changes in the geometry of the orbitals of the molecule, and orbitals with a π^* or σ^* symmetry on the low interacting gold can be distorted. Moreover, a deeper analysis of the overlayer has revealed the presence of a small amount of chlorine contaminant, which was absent on
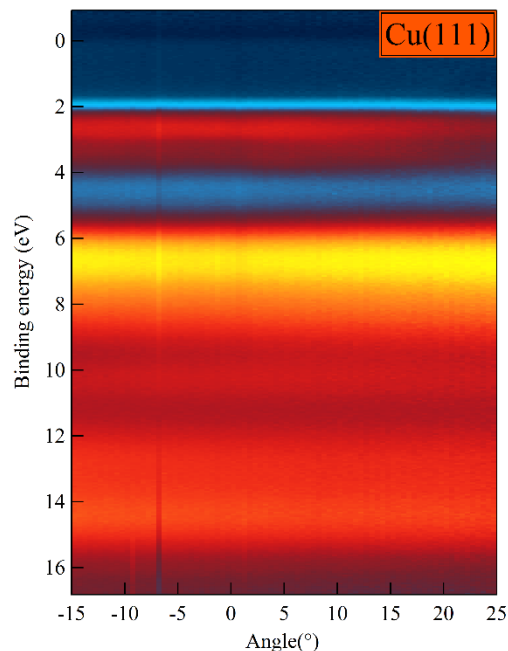

Figure 24: ARUPS map of the borixinated framework on Cu(111). The spectra have been taken with helium discharge lamp, not monochromatized, employing the He(II) spectral line, the pass energy was set to 10 eV.

Au(111). The simplest explanation is that the powder of the molecule itself contains the residues of the synthesis of THDB, which comprehends the diboron tetrachloride. On the unreactive gold substrate this

54

compound does not adsorb, while copper is interacting enough with this molecule to allow the adsorption. These differences in the substrate, and maybe also the presence of contaminants, have an effect on the valence band. The peak at 10 eV of binding energy is less intense, while a broad feature at 6.5 eV is more intense. For this last case, a comparison with the gold case it is not possible, because in this region the signal from the substrate superimposes on the molecular one. The most relevant difference resides in the valence band dispersion, which is absent in this case. This information makes somehow the study of THDB on this substrate less appealing with respect to the gold one. On the other hand, it can be worth to understand the reason of the lack of the delocalized states that disperse in the same fashion as boroxene on Au(111). From our data it seems reasonable to exclude the occurrence of different reactions than the boroxine formation, and the presence of contaminants, even if unwanted, is low. An explanation to this phenomenon can involve the high copper reactivity, which enhances the local nature of the molecular orbitals, thus lowering the delocalization of states.

2.15 CONCLUSION

We have worked on three boronic systems that allowed us to have a deeper insight in the two-dimensional boroxine-based systems supported on metallic substrates. As far as we know, this is the first extended spectroscopic study of the boroxine-gold interface. The obtained results indicate the presence of interesting electronic properties that add to the, already reported, morphological properties of the boroxine based frameworks. The investigation on the vertical charge transfer has proven the existence of an ultra-fast electron delocalization channel to the substrate. We have also prepared a promising material, the boroxene, that is a possible candidate to overcome the in-plane charge transport limitations of this class of materials. As future perspective, two different lines can be followed. It will be interesting to study other boronic acids, such as 1-anthracenboronic acid and its structural isomers, 2-/9-anthracenboronic acid and phenanthrene-based similar derivatives, to perform a more systematic work on the geometrical effects on the boroxination reaction. Moreover, passing to 1-tetracenboronic acid, would allow to reach the adsorption in the visible region to monitor the electron dynamics by means of pump and probe spectroscopy. Finally, further efforts to improve the morphology of the boroxene can be tried. For that purpose, new substrates could be tested. Moreover, it would be interesting to prepare samples *ex situ* taking advantage of a solvent that keeps for a longer time the reaction conditions reversible.

BIBLIOGRAPHY:

1. WATT, F., BETTIOL, A. A., VAN KAN, J. A., TEO, E. J. & BREESE, M. B. H. ION BEAM LITHOGRAPHY AND NANOFABRICATION: A REVIEW. *Int. J. Nanosci.* **04,** 269–286 (2005).

2. Zardetto, V., Brown, T. M., Reale, A. & Di Carlo, A. Substrates for flexible electronics: A practical investigation on the electrical, film flexibility, optical, temperature, and solvent resistance properties. *J. Polym. Sci. Part B Polym. Phys.* **49,** 638–648 (2011).

3. Song, D. *et al.* High-Resolution Transfer Printing of Graphene Lines for Fully Printed, Flexible Electronics. *ACS Nano* **11,** 7431–7439 (2017).

4. Yu, X. *et al.* Needle-shaped ultrathin piezoelectric microsystem for guided tissue targeting via mechanical sensing. *Nat. Biomed. Eng.* **2,** 165–172 (2018).

5. Rhyee, J.-S. *et al.* High-Mobility Transistors Based on Large-Area and Highly Crystalline CVD-Grown $MoSe_2$ Films on Insulating Substrates. *Adv. Mater.* **28,** 2316–2321 (2016).

6. van der Zande, A. M. *et al.* Grains and grain boundaries in highly crystalline monolayer molybdenum disulphide. *Nat. Mater.* **12,** 554–561 (2013).

7. Zhang, X., Zeng, Q. & Wang, C. On-surface single molecule synthesis chemistry: a promising bottom-up approach towards functional surfaces. *Nanoscale* **5,** 8269 (2013).

8. Hall, D. G. *Boronic acids : preparation and applications in organic synthesis, medicine and materials*. (Wiley-VCH, 2011).

9. Toffoli, D. *et al.* Electronic properties of the boroxine–gold interface: evidence of ultra-fast charge delocalization. *Chem. Sci.* **8,** 3789–3798 (2017).

10. Stredansky, M. *et al.* On-surface synthesis of a 2D boroxine framework: a route to a novel 2D material? *Chem. Commun.* **54,** 3971–3973 (2018).

11. *Boronic Acids*. (Wiley-VCH Verlag GmbH & Co. KGaA, 2011). doi:10.1002/9783527639328

12. Frankland, E. & Duppa, B. F. Vorläufige Notiz über Boräthyl. *Ann. der Chemie und Pharm.* **115,** 319–322 (1860).

13. Michaelis, A. & Becker, P. Ueber Monophenylborchlorid und die Valenz des Bors. *Berichte der Dtsch. Chem. Gesellschaft* **13,** 58–61 (1880).

14. Khotinsky, E. & Melamed, M. Die Wirkung der magnesiumorganischen Verbindungen auf die Borsäureester. *Berichte der Dtsch. Chem. Gesellschaft* **42,** 3090–3096 (1909).

15. Nishiyabu, R., Kubo, Y., James, T. D. & Fossey, J. S. Boronic acid building blocks: tools for sensing and separation. *Chem. Commun.* **47,** 1106 (2011).

16. Bosch, L. I., Fyles, T. M. & James, T. D. Binary and ternary phenylboronic acid complexes with saccharides and Lewis bases. *Tetrahedron* **60,** 11175–11190 (2004).

17. Tossell, J. A. Boric acid, "carbonic" acid, and N-containing oxyacids in aqueous solution: Ab initio studies of structure, pKa, NMR shifts, and isotopic fractionations. *Geochim. Cosmochim. Acta* **69,**

5647–5658 (2005).

18. Schnürch, M., Holzweber, M., Mihovilovic, M. D. & Stanetty, P. A facile and green synthetic route to boronic acidesters utilizing mechanochemistry. *Green Chem.* **9,** 139–145 (2007).

19. Miyaura, N. & Suzuki, A. Stereoselective synthesis of arylated (E)-alkenes by the reaction of alk-1-enylboranes with aryl halides in the presence of palladium catalyst. *J. Chem. Soc.{,} Chem. Commun.* 866–867 (1979). doi:10.1039/C39790000866

20. KUIVILA, H. G., KEOUGH, A. H. & SOBOCZENSKI, E. J. Areneboronates from diols and polyols1. *J. Org. Chem.* **19,** 780–783 (1954).

21. Yoon, J. & Czarnik, A. W. Fluorescent chemosensors of carbohydrates. A means of chemically communicating the binding of polyols in water based on chelation-enhanced quenching. *J. Am. Chem. Soc.* **114,** 5874–5875 (1992).

22. Adams, J. Potential for proteasome inhibition in the treatment of cancer. *Drug Discov. Today* **8,** 307–315 (2003).

23. Yang, W. *et al.* Diboronic acids as fluorescent probes for cells expressing sialyl lewis X. *Bioorg. Med. Chem. Lett.* **12,** 2175–2177 (2002).

24. Cooper, C. R., Spencer, N. & James, T. D. Selective fluorescence detection of fluoride using boronic acids. *Chem. Commun.* **0,** 1365–1366 (1998).

25. Galbraith, E., Fyles, T. M., Marken, F., Davidson, M. G. & James, T. D. Fluorescent Boron Bis(phenolate) with Association Response to Chloride and Dissociation Response to Fluoride. *Inorg. Chem.* **47,** 6236–6244 (2008).

26. Katif, N. *et al.* Boronic acid-facilitated α-hydroxy-carboxylate anion transfer at liquid/liquid electrode systems: the EICrev mechanism. *J. Solid State Electrochem.* **13,** 1475–1482 (2009).

27. Niu, W., O'Sullivan, C., Rambo, B. M., Smith, M. D. & Lavigne, J. J. Self-repairing polymers: poly(dioxaborolane)s containing trigonal planar boron. *Chem. Commun.* **0,** 4342 (2005).

28. Guan, Y. & Zhang, Y. Boronic acid-containing hydrogels: synthesis and their applications. *Chem. Soc. Rev.* **42,** 8106 (2013).

29. Feng, X., Ding, X. & Jiang, D. Covalent organic frameworks. *Chemical Society Reviews* **41,** 6010–6022 (2012).

30. Cote, A. P. *et al.* Porous , Crystalline , Covalent Organic Frameworks. *Science (80-.).* **310,** 1166–1171 (2005).

31. Korich, A. L. & Iovine, P. M. Boroxine chemistry and applications: A perspective. *Dalt. Trans.* **39,** 1423–1431 (2010).

32. Perttu, E. K., Arnold, M. & Iovine, P. M. The synthesis and characterization of phenylacetylene tripodal compounds containing boroxine cores. *Tetrahedron Lett.* **46,** 8753–8756 (2005).

33. De, P., Gondi, S. R., Roy, D. & Sumerlin, B. S. Boronic Acid-Terminated Polymers: Synthesis by RAFT and Subsequent Supramolecular and Dynamic Covalent Self-Assembly. *Macromolecules* **42,** 5614–5621 (2009).

34. Tokunaga, Y., Ueno, H., Shimomura, Y. & Seo, T. Formation of Boroxine: Its Stability and

Thermodynamic Parameters in Solution. *Heterocycles* **57,** 787 (2002).

35.   Tokunaga, Y., Ito, T., Sugawara, H. & Nakata, R. Dynamic covalent chemistry of a boronylammonium ion and a crown ether: formation of a C3-symmetric [4]rotaxane. *Tetrahedron Lett.* **49,** 3449–3452 (2008).

36.   Nath, K. G. *et al.* Crystal engineering in two dimensions: An approach to molecular nanopatterning. *J. Phys. Chem. C* **111,** 16996–17007 (2007).

37.   El Garah, M., Macleod, J. M. & Rosei, F. Surface Science Covalently bonded networks through surface-con fi ned polymerization. *Surf. Sci.* **613,** 6–14 (2013).

38.   Plas, J., Ivasenko, O., Martsinovich, N., Lackinger, M. & De Feyter, S. Nanopatterning of a covalent organic framework host–guest system. *Chem. Commun.* **52,** 68–71 (2016).

39.   Dienstmaier, J. F. *et al.* Synthesis of well-ordered COF monolayers: Surface growth of nanocrystalline precursors versus direct on-surface polycondensation. *ACS Nano* **5,** 9737–9745 (2011).

40.   Wang, R.-N., Zhang, X., Wang, S.-F., Fu, G. & Wang, J. Flatbands in 2D boroxine-linked covalent organic frameworks. *Phys. Chem. Chem. Phys.* **18,** 1258–1264 (2016).

41.   Gutzler, R. Band-structure engineering in conjugated 2D polymers. *Phys. Chem. Chem. Phys.* **18,** 29092–29100 (2016).

42.   Ourdjini, O. *et al.* Substrate-mediated ordering and defect analysis of a surface covalent organic framework. *Phys. Rev. B* **84,** 125421 (2011).

43.   Kanda, F. A., King, A. J., Russell, V. A. & Katz, W. PREPARATION OF BORON MONOXIDE AT HIGH TEMPERATURES. *J. Am. Chem. Soc.* **78,** 1509–1510 (1956).

44.   Nicholls, D. 1225. The reduction of boric oxide to boron monoxide. *J. Chem. Soc.* **0,** 6644 (1965).

45.   Zintl, E., Morawietz, W. & Gastinger, E. Bormonoxyd. *Zeitschrift für Anorg. und Allg. Chemie* **245,** 8–11 (1940).

46.   Holliday, A. K. & Massey, A. G. Boron Subhalides and Related Compounds with Boron-Boron Bonds. *Chem. Rev.* **62,** 303–318 (1962).

47.   Wartik, T. & Apple, E. F. A NEW MODIFICATION OF BORON MONOXIDE. *J. Am. Chem. Soc.* **77,** 6400–6401 (1955).

48.   Brotherton, R. J., McCloskey, A. L. & Manasevit, H. M. New Syntheses of Diboron Tetrafluoride. *Inorg. Chem.* **2,** 41–43 (1963).

49.   Claeyssens, F., Allan, N. L., Norman, N. C. & Russell, C. A. Design of three-dimensional solid-state boron oxide networks: *Ab initio* calculations using density functional theory. *Phys. Rev. B* **82,** 094119 (2010).

50.   Zhang, Z., Pu, L., Li, Q. & King, R. B. Pathways to the Polymerization of Boron Monoxide Dimer To Give Low-Density Porous Materials Containing Six-Membered Boroxine Rings. *Inorg. Chem.* **54,** 2910–2915 (2015).

51.   Lichtenstein, L. *et al.* The Atomic Structure of a Metal-Supported Vitreous Thin Silica Film. *Angew. Chemie Int. Ed.* **51,** 404–407 (2012).

3.1 INTRODUCTION

Polymeric carbon nitride (CN) materials have attracted a lot of attention in recent years for the many fields of their applications, ranging from photocatalysis to fuel cells[1–3], as catalyst supports[4,5] or redox catalysts.[6] The main advantages they offer comprehend good thermal stability[7] and a peculiar set of electronic and optical properties.[8] It has also to be taken into account that they can be synthesized from inexpensive and earth-abundant precursors. Moreover, another great potential of these polymeric, or "soft", materials resides in their chemical tunability in terms of optoelectronic properties and nature of the active sites.[9] The analogy between these materials and graphene has brought them to be considered as a storage material. In this perspective, the CN has been studied as lithium battery anode. It has been calculated that it should have a much higher Li capacity than the graphitic carbon.[10] From the electronic point of view, CN materials are commonly considered as semiconductors with a band gap between the π $-\pi^*$ bands of 2.5-2.8 eV, corresponding to the adsorption in the blue region of the visible spectrum.[11] This leads to a yellow/brown color of CNs. If the polymer is exposed to higher temperatures during the synthesis procedure, than the structure gets distorted and an additional transition n - π^* is allowed, with a redshift in the adsorption spectrum.[11] Moreover, the electronic properties of these materials have attracted the interest for possible photocatalytic applications, in particular photocatalytic water splitting and CO_2 fixation[12], which are now the major fields of investigation for these novel materials. Carbon nitrides have already shown a catalytic activity for the water splitting reaction, even though at the present stage the efficiency remains lower than that obtained with inorganic photocatalysts.[1,13] Moreover, the activity for H_2 evolution has been often tested with a sacrificial electron donor,[13] which undergoes the oxidation reaction instead of water. Within these considerations, a strong interest for improving the CN water splitting activity is investing the research community. In addition to the water splitting reaction catalysis, the carbon nitride has also been studied for its mechanical, chemical and thermal resilience and has risen the interest in different fields of catalysis: the possible applications involve roles either as active catalyst or as support for other active catalysts.[8] Going more in the detail about CN composition, it has to be stressed that we are not discussing about a specific material but rather about a family of materials, having similar structure and stoichiometry. Firstly, these materials do not contain only C and N, but they have also an H content. In the first studies on this topic, CN has been modeled as a planar assembly of condensed s-triazine or s-heptazine units via tertiary amines, as reported in figure 1a and 1b, respectively. Only in few cases it has been reported a fully condensed s-triazine based material, with a limit formula of C_3N_4,[14] in most of the cases common synthetic procedures yield amorphous or semi-crystalline materials resembling melon an heptazine-based linear polymer with a limit formula of C_2N_3H (Fig 1c).[15,16,14] Standard synthetic protocols start with a precursor molecule (cyanamide, dicyanamide, melamine, urea) that upon heating to approximately 720 K undergoes a condensation reaction, with the release of NH_3.[2] In a common reaction pot, the cyanimide firstly forms melamine (2,4,6-triamino-*s*-triazine, Fig. 1d), which is transformed through consecutive condensations to melem (1,3,4,6,7,9,9b-heptaazaphenalene-2,5,8-triamine, Fig. 1e) that, in turns, finally polymerizes into larger structures with the limiting composition of

C_2N_3H. At higher temperatures, carbon containing fragments are released and it is not possible to completely get rid of H defects and obtain a fully condensed material (C_3N_4).[17,18] The amorphous state and low solubility of these materials prevent a thorough characterization in terms of local structure and composition; however, in some case it has been possible to isolate some graphitic crystalline phases and determine their structures: a 2D H-bonded array of zig-zag melon chains[19] and a fully covalent graphitic-like heptazine based network (polyheptazine imide, PHI).[20] In both cases, the heptazine is the structural unit, with a secondary amino group (-NH-) acting as linker between adjacent units. However, in both cases, a clear description of the chemical properties of these crystalline polymers is prevented by the fact that the heptazine units are involved in intermolecular H-bonding interactions, occurring between adjacent melon chains or between the heterocycles forming the triangular voids of the PHI structure and possible trapped melamine molecules. As a matter of fact, no photo activity towards H_2 evolution has been reported for these crystalline phases compared to amorphous phases. In addition to the thermal synthesis, another pathway to obtain carbon nitride material has been found. In particular, it is possible to employ the ionothermal synthesis to form Poly(triazineimide) with incorporated lithium chloride to stabilize the structure.[21,22] The structure of this material reveals a repetition of the melamine unit connected via -NH- bridges. As mentioned above, CNs are commonly considered as semiconductors, and analogously to the photochemical splitting of water with transition metal oxides, an exciton-assisted mechanism is usually proposed, where the separation and migration of the exciton charge carriers (electron and hole) allow the excited electron to take part in the reduction reaction and the hole to the
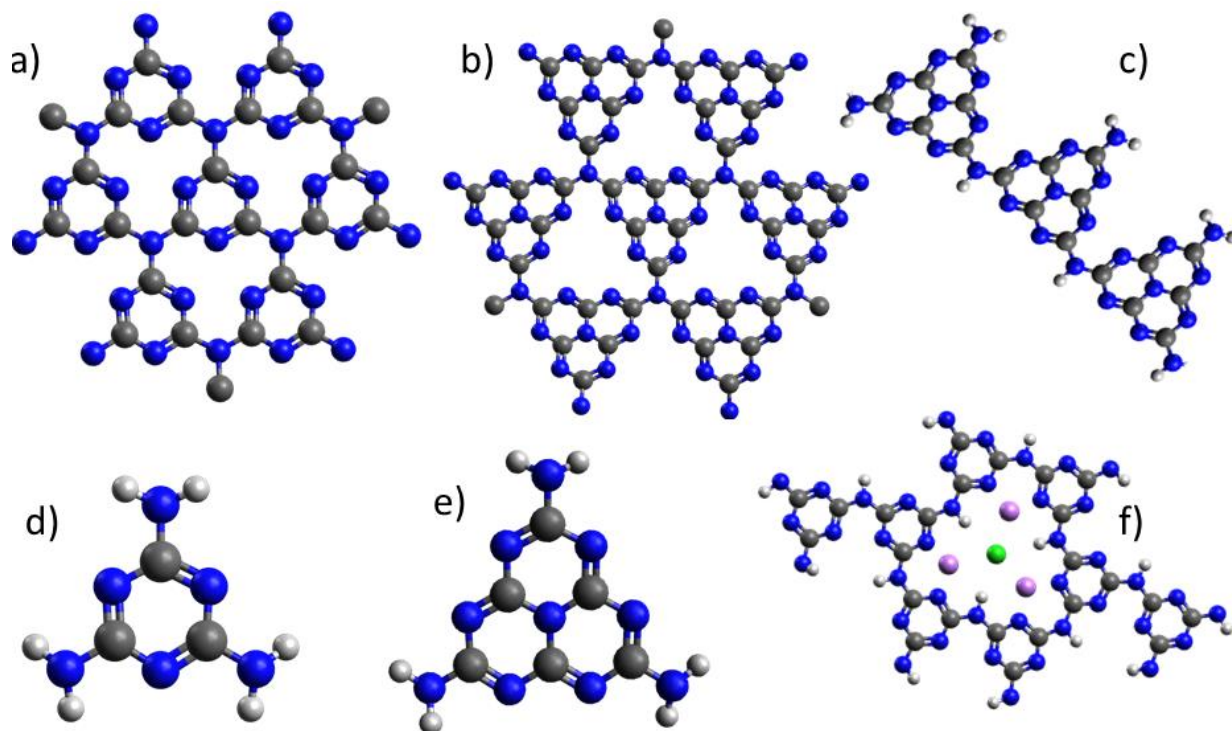

Figure 1: models of the carbon nitride compounds presented in the text. a) graphitic C_3N_4 based on triazine repetitive unit connected via tertiary amino groups. b) the other proposed form for the graphitic C_3N_4 based on heptazinic repetitive unit connected in the same fashion. c) melon, linear polymer based on the heptazine unit connected through -NH- linkers. Each unit also preserves a primary amino group (-NH2). Second line, d) melamine molecule, in the center with letter e) the melem molecule and on the right, f), poly(triazine)-imide (PTI), the occupancy of the Li^+ sites is of 1/3. Blue spheres represent nitrogen atoms, the grey ones the carbon atoms and the white spheres are hydrogen atoms. The green balls in the PTI are Cl^- and the pink ones the Li^+ ions

oxidation one. In this context, the negligible photoactivity shown by crystalline phases of melon or PHI is explained by the limited availability of active sites, such as polymer terminations and defects. Indeed, intermolecular H-bonding interactions would prevent H-bonding of water molecules at the reducing sites, which have been possibly identified with the bridging -NH- or peripheral amino groups -NH_2.[23] However, this description of the photo-catalysis mechanism seems unlikely for CN materials, due to the prediction of high values for both exciton dissociation energies[24–27] and polaron stabilization energies.[28,] Recently, another mechanism has been suggested, which predicts the nitrogen atoms inside the heteroaromatic rings to be the active sites instead.[27,29] In this scheme, a so called proton-coupled electron transfer (PCET)[30] is taking place. In detail, a photoexcitation of the heterocycle can lead to an electron transfer from a water molecule H-bonded to the aromatic nitrogen resulting in filling of the vacancy in the HOMO heterocycle. This process is followed by a proton transfer in the same direction with the result, that two radicals are formed, the OH· radical and the hypervalent heterocyclic radical (the heterocycle with the addition of a e⁻ and H⁺). Two heterocyclic radicals can then recombine together in an exothermic dark reaction to form a H_2 molecule.[27] Despite the impact that H-bonding interactions can have in the photo-catalytic performances of CN materials, there are still no detailed spectroscopic information on the H-mediated interactions between the functional groups themselves or with the water molecule, as well as for the polymer and for its building blocks (melamine and melem). In this context, we have decided to focus our investigation on these small CN model compounds, and their intermolecular and water-molecule interactions. Working with small molecular species, allows us to operate in the UHV conditions and with in situ prepared samples. The interpretation of the experimental data has been supported by DFT calculations.

3.2 EXPERIMENTAL CONDITIONS

Melamine and melem molecules have been studied in gas-phase and in form of thin films. In the melamine case, the study is more comprehensive and involves the use of two different surfaces, Au(111) and Cu(111). The melamine/Cu(111) interface has been furtherly used for studying the melamine/water H-bonding interaction. For melem, preliminary investigations have been done only for samples grown on Au(111). For both molecules, the gas phase measurements have been acquired at the GasPhase beamline of the ELETTRA synchrotron.[31] The calibration of NEXAFS and XPS has been performed measuring the CO_2 and N_2 spectral lines for the C1s and N1s spectra, respectively. The C 1s and N 1s spectra were measured with photon energies of 382 eV and 495 eV and energy resolutions of 140 and 220 meV, respectively. The NEXAFS measurement has been done in total ion yield with a photon energy resolution set to 200 meV. As for films grown on Au(111), the XPS and NEXAFS measurements have been performed at the PM4 beamline of the BESSY II synchrotron facility,[32] with a Scienta SES-100 hemispherical analyzer. The N 1s and C 1s spectra were measured at normal emission with photon energy of 500 eV and an overall energy resolution of 230 meV. The energy scale was calibrated by aligning the Au $4f_{7/2}$ peak to the binding energy of 84.0 eV. The N K-edge spectra were acquired in Auger yield mode by using a fixed energy window of about 20 eV centered at the kinetic energy of 372 eV. The spectra were collected with the electric field polarization of the light parallel (s-polarization) and almost perpendicular (p-polarization) to the surface plane. The spectra were calibrated by using the Au 4f line measured with both first and second order of

the last photon energy of the NEXAFS spectrum. The UPS has been taken at the Surface Physics laboratory of Uppsala University. The melamine has been purchased from Sigma Aldrich with a purity of 99%%, while the melem has been purchased from Synthon-Lab with a purity of ca. 90%. Before deposition, both molecules have been carefully degassed, in particular the melem which was highly contaminated by unreacted melamine. The molecule has been deposited from a crucible on a single crystal cleaned by sputtering and annealing cycles. The experiments using melamine on Cu(111) have been performed on the ANCHOR end-station of the ALOISA beamline of the ELETTRA synchrotron facility.[33] Also in this case the molecule has been evaporated from a crucible. The water has been cleaned by pump and freeze cycles before dosing form a leak valve in the chamber. The theoretical calculations were performed by the group of prof. B. Brena from the Uppsala university. We used ab initio calculations based on plane-wave[34] DFT.[35,36] The static ions and valence electrons were handled by the projected augmented wave (PAW) method[37] as implemented in the VASP code.[37,38] We represented the exchange and correlation interactions through the generalized gradient approximation (GGA) with PBE functional.

3.3 MELAMINE: RESULTS

In order to investigate the effect of H-bonding in the CNs, we have explored the effect of this weak bond for the precursors of the polymer. In particular, the melamine molecule appears to be a good starting reference for the final materials, since it contains already the aromatic nitrogen atoms and the amino termination. Moreover, in the case of melamine a detail investigation of the N containing functional groups has been possible thanks to the its high volatility, allowing gas phase measurements, fundamental for identifying the spectroscopic fingerprints of the non-interacting system. The aromatic nitrogens are structurally present in the ideal structure of the graphitic CN. On the other hand, the amino groups are also present in real carbon nitride as defects and do possibly play a role in their catalytic properties. The only lacking species in melamine present in CN are the tertiary nitrogen atoms (NC_3), that link the subunits in the ideal form of the polymer. This kind of nitrogen will need a separate inquiry. To have a full picture of the H-bonding between the melamine molecules, we have performed a combined gas phase and solid state spectroscopic investigation. We have chosen, as substrate, the Au(111) surface, which is known from literature to promote a flat adsorption geometry with a self-assembly into honeycomb structures determined by intermolecular NH••N=C hydrogen bonds.[39–41] We studied the system by means of XPS and NEXAFS. It should be noticed that even if the formal oxidation state of an element remains unchanged upon the formation of a hydrogen bond, the core level can experience a significant shift in binding energy.[42,43] The XPS spectra reported in figure 2 show the N1s signal taken in three different conditions: gas phase, 1.2 monolayers and 6 monolayers. The bottom scale refers to the solid-state measurement and has its zero set to the Fermi level of the gold while the top scale refers to the gas phase experiment and its zero is the vacuum level. While in the gas phase two distinct peaks are present, on the surface the energy difference between them is reduced resulting in one broad feature. The distance between the non-equivalent nitrogen atoms is reduced from 1.5 eV for the gas phase to less than 1 eV for the films grown on the surface. In all cases, at higher binding energy there is the amino ($-NH_2$) peak, while at lower energy there is the contribution from the nitrogen atoms inside the triazine aromatic ring (=N-), as confirmed by the theory (see later, Fig. 3). The graphical aligning of the =N- peaks between the gas phase

and the 6 layers spectra has been imposed manually, so at a first glance there may seem to be no change in the triazine nitrogen position. Considering the 1.2 layers coverage, it has been possible to evaluate the
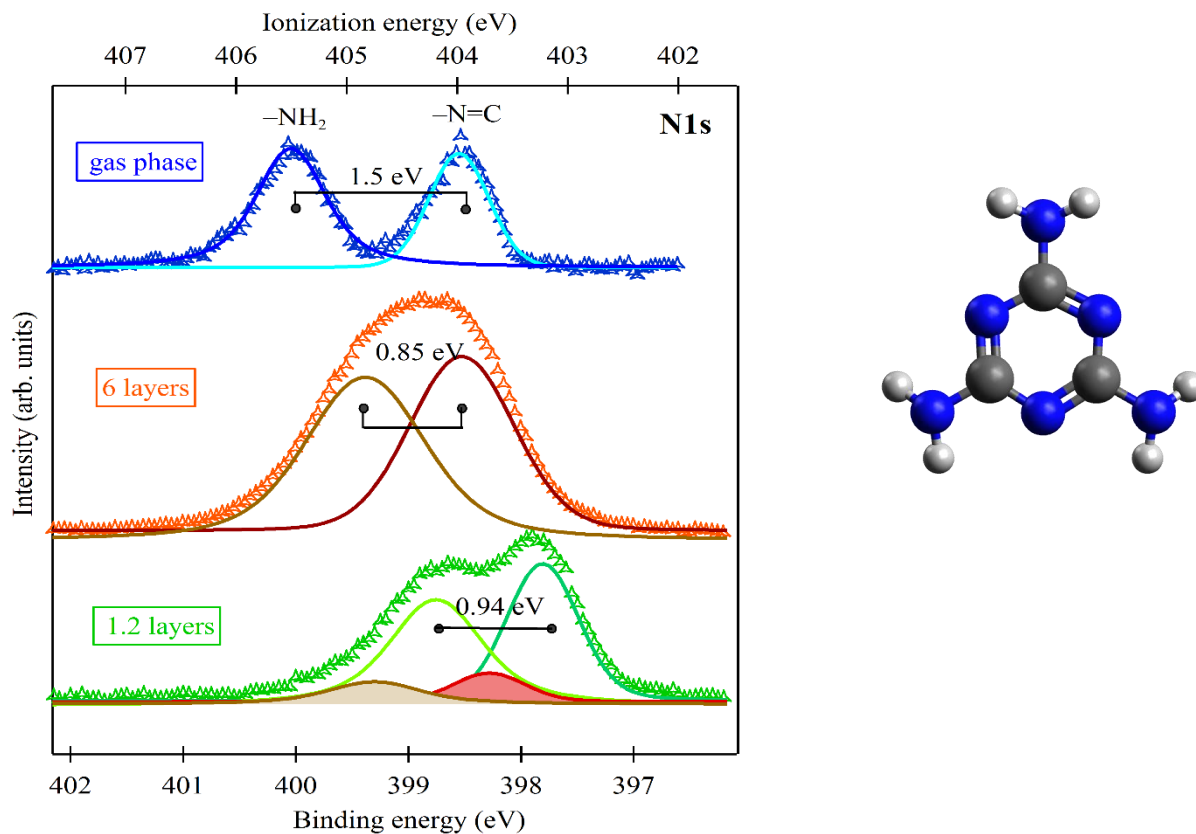

Figure 2: XPS spectra of melamine. The energy scale on top refers only to the gas phase experiment. The N 1s spectra were measured with photon energies of 495 eV and energy resolutions of 220 meV. The measurement on Au(111) has been acquired with a photon energy of 500 eV and an overall resolution of 230 meV.

contribution from the second layer, represented by filled curves on the graph. The shift toward higher binding energy of the signal from the second layer molecules can be explained with the image charge effects, that is a function of the distance from the substrate. From the STM results in literature, it is possible to deduce the presence of a weak interaction between the amino group, acting as a hydrogen donor in the H-bond, and the triazine nitrogen, acting as an acceptor. The presence of this interaction can explain the chemical shift between the solid-state measurement and the gas phase ones. A better understanding of the system can be achieved through theoretical simulations. The theoretical modeling, performed by the group of prof. B. Brena from the Uppsala University, foresees a substantial change in the binding energy of the amino group, while the triazine nitrogen undergoes only a slight shift. The results are summarized in figure 3, showing the simulated XPS spectra of the isolated molecule, the dimer, the trimer and the hexagonal structure. The peaks have been aligned and normalized with respect to the N=C peak. The latter resembling the honeycomb domains observed for monolayer coverage of melamine on Au(111).[39–41] In the monomer, where there are no H-bonds, the spectra show two peaks quite distant (1.67 eV), similarly to the gas phase spectrum. The vicinity of a second molecule determines the occurrence of a double H-bonding interaction and a new feature appears between the signal of the non-interacting functional groups. The new feature corresponds to the 1 s level of amino N atoms involved in
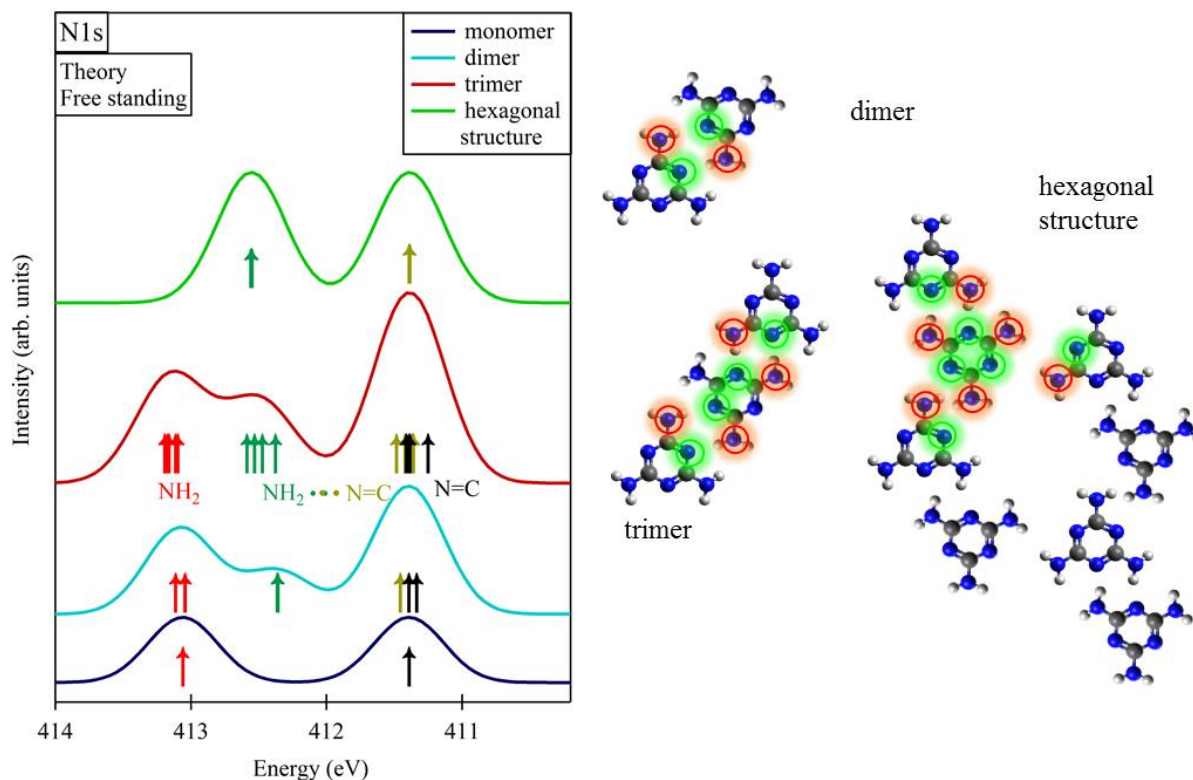
Figure 3: theoretical simulation of different situation of melamine molecules. The monomer can be interpreted as the model for the gas phase experiment, while the hexagonal H-bonding structure on Au(111) can be seen as the simulation of the monolayer coverage. The intermediate steps show the gradual influence of the H-bonding on the peak positions. On the left a model of the H-bonded network is depicted. Green circles highlight the acceptors of the H-bonding while red circles the donors.

the H-bonds, while the triazine counterparts remain almost unperturbed. This new feature, obviously, is more intense in the trimer and it is the only amino-related feature surviving in the periodic hexagonal structure, where all amino groups are involved in the H-bonding networks. In particular, the distance between the two nitrogen peaks is reduced by 0.51 eV due to the hydrogen bond formation, not far from the experimental result of 0.66 eV (multilayer) and 0.57 eV (monolayer). The presence of the substrate affects only slightly the position of the peaks in the spectrum (not reported), reflecting the fact that the lateral interaction between the molecules prevails on the interaction with the substrate. In all the models, after optimization, the H-bonding distance, measured between the H-acceptor nitrogen and hydrogen atom, results in the range of 2.0 - 2.2 Å. To further investigate the effects of intermolecular hydrogen bonding on the electronic properties of the melamine molecule we measured the N K edge NEXAFS spectra on both gas phase and films on Au(111). The experimental spectra are reported in figures 4 and 5. In figure 4 are reported the NEXAFS spectra of gas phase and different melamine coverage on Au(111) substrate. The next figure reports the comparison between experiment and theory in gas phase and on a 6 layers film. The gas phase signal presents three distinct features in the π* region labeled A, B, C in the figure. The spectra acquired in the solid-state measurements show a pronounced dichroism between the two polarizations, that indicates a flat adsorption geometry, confirming previously reported STM data.[39,40] Interestingly, in the adsorbed molecules, the spectral profiles are quite different from the gaseous melamine. While peaks A and C are still recognizable, peak B seems to be shifted to lower energies and

appears as a shoulder of peak A. A clear understanding of the changes observed in the solid state spectra
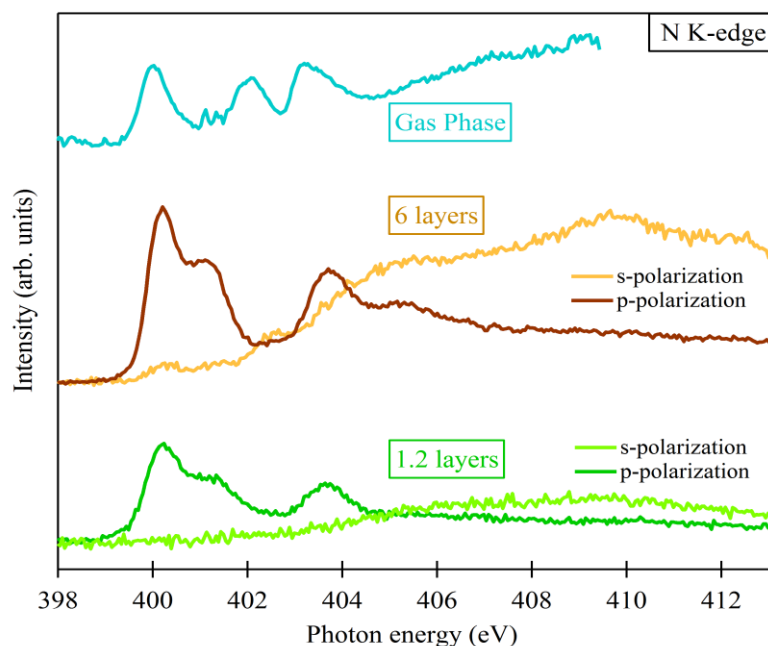

Figure 4: Comparison between the NEXAFS spectra of melamine in the gas phase and on Au(111) at monolayer and multilayer coverage. The gas phase signal has been acquired in total ion yield, with a resolution of 200 meV. The calibration of the spectrum has been performed with N_2.. The solid-state measurement has been performed in Auger yield, acquiring counts in a window large 20 eV around 372 eV corresponding to the KVV Auger of nitrogen.
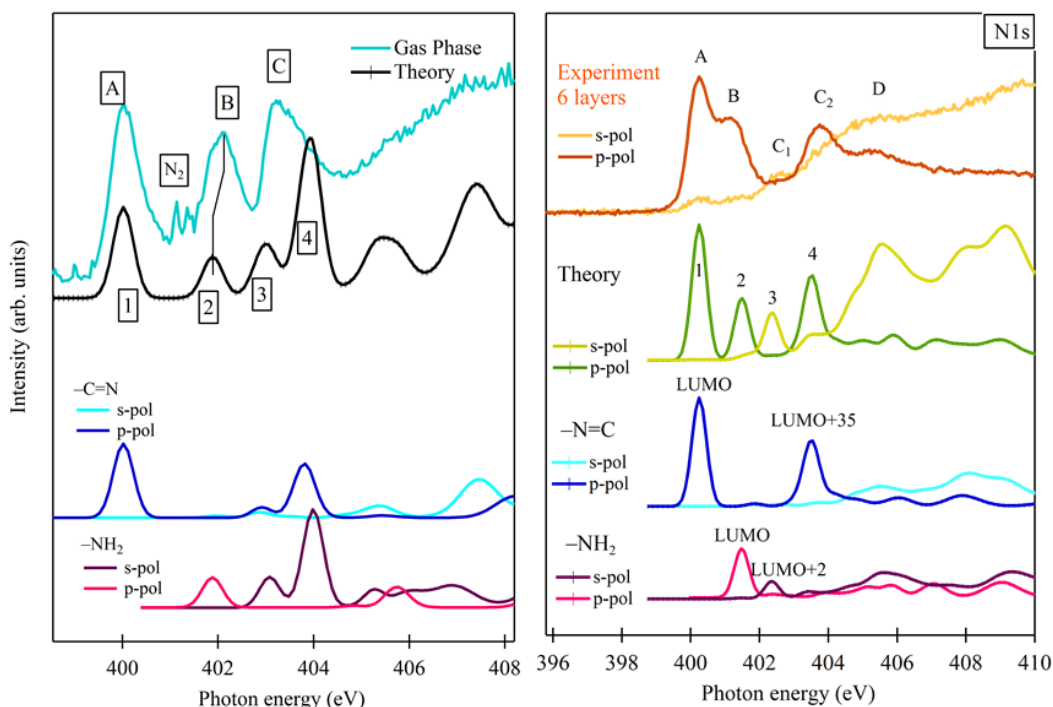
Figure 5: N K-edge NEXAFS analysis of the melamine. In the left panel the gas phase experiment and simulation spectra have been reported. The total simulated spectrum (black curve) is divided into contributions from the triazinic (dark blue the p-component and light bluet the s-pol) and aminic pink s polarization and purple p-pol) nitrogen atoms. The NEXAFS of the film deposited on Au(111) is reported on the right. The experimental curve, obtained measuring the thick film, is compared to the simulation (green traces) divided in contribution from the z-direction (p-polarization) and xy-plane (s-polarization) from the two types of nitrogen. In each graph the first peak of the simulation is aligned to the first experimental feature.
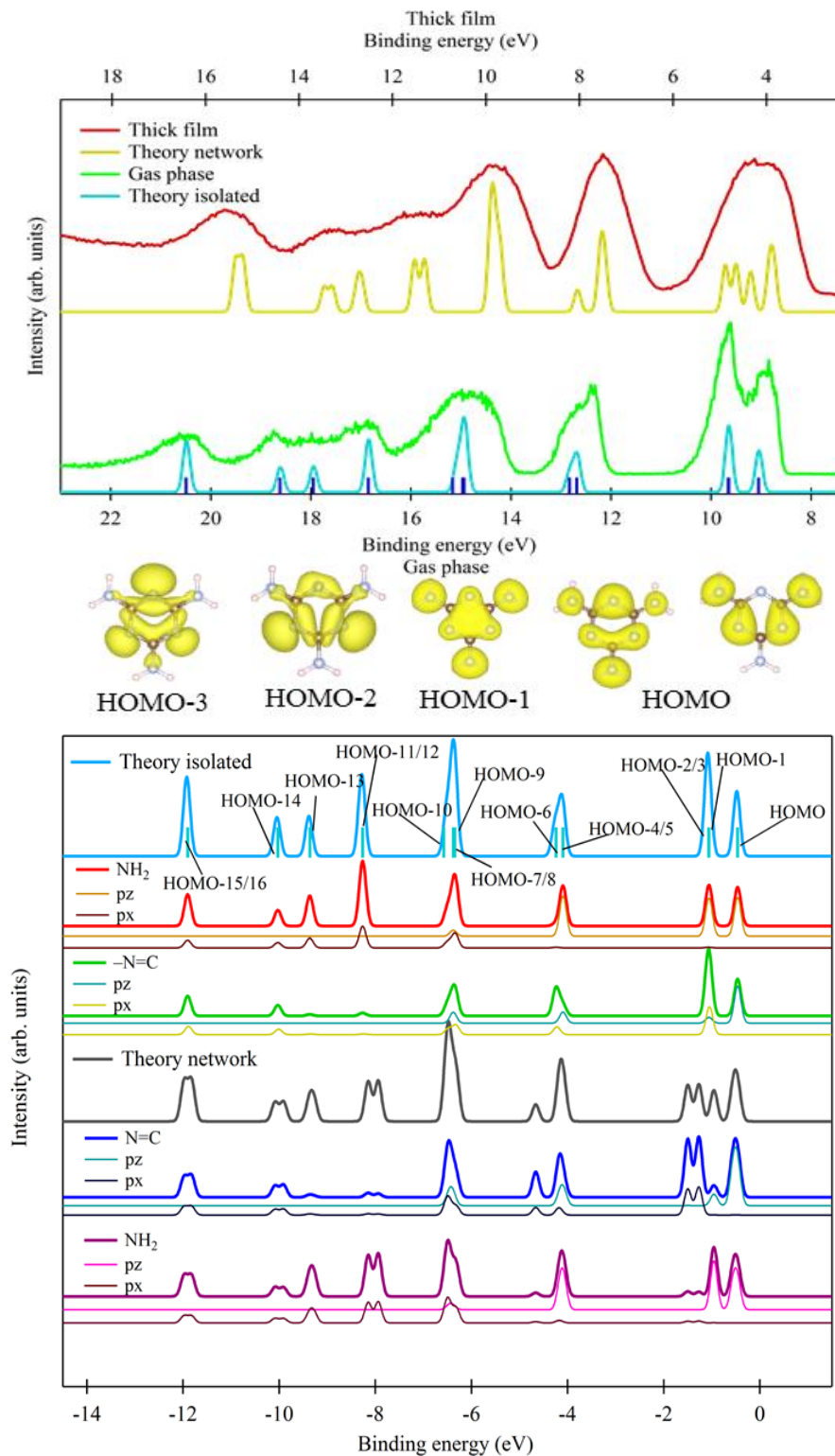
65

Figure 6: Top panel reports the UPS spectra of melamine in gas the phase and from a thick film adsorbed on Au(111). The first one has been measured with synchrotron radiation of 40 eV. The second one has been acquired with the He(II) line of a He discharge lamp (hv = 40.8 eV). The x scale on the top of the figure in the top panel is the binding energy of the thick film measurement. The bottom scale is the energy scale of the gas phase experiment. The experimental curves are compared with TDOS of the isolated molecules and of a hexagonal layer of melamine. The theoretical simulation is analyzed in the bottom panel, where the contributions from the different nitrogen atoms and atomic orbitals are shown.

has been possible thanks to theoretical simulations of the spectra. In gas phase, peak A is a transition from

the triazine N1s level to the LUMO, while peak B is a transition to the same orbital from the amino N1s level, reflecting an energy distance similar to that observed in the XPS. The origin of peak C is more complicated and corresponds to the overlap of three distinct transitions. The first two of them start from the triazine N1s and promote the electron to empty orbitals of π* (LUMO+6 and +10) σ* (LUMO+5) symmetry, while the last transition involves an electron moving from the amino N1s toward σ* orbitals (LUMO+2 and +4), the latter essentially localized on the amino groups terminations. Concerning the solid-state measurements, the theoretical investigation has been performed on a four-molecule model with H-bonding between them. The simulation reveals that the first two main peaks, A and B, have the same origin as for gas phase, with the second peak corresponding to the transition from the amino N 1s to the LUMO shifted to lower photon energy, due to the lower energy of the starting core level, confirming the findings of the XPS analysis. The third peak C-2 results from the overlap of many transitions from a triazine nitrogen to different π* orbitals having similar symmetry to LUMO+10 of gaseous melamine. To complete the picture, the theory foresees a peak in s-polarization at 402.4 eV, that may correspond to the peak labeled as C-1 in the spectrum taken in s-polarization. This feature is due to a transition from the amino N 1s level to an orbital similar to LUMO+2 of gaseous melamine but with strongly distorted geometry (the lobe extending on the N-H involved in the H-bond is missing). Moreover, the transition to LUMO+4 observed in the gas phase spectrum is completely quenched in the solid state spectra. In addition to the XPS and NEXAFS, we have also explored the valence band of melamine by means of UPS, figure 6. In analogy to the other techniques, we have acquired spectra for gaseous melamine, as well as for a thick film grown on Au(111). The spectra are compared with theoretical TDOS of the isolated molecule and for a hexagonal layer of melamine. A first glance at the experimental spectra suggests a high similarity between the thick film and the gas phase. The theoretical calculations are in good accordance with both of them. However, the theory shows some subtle differences between monomer and H-bonded network. In particular, the two bands between 0 and -2 eV in the isolated case become 4 peaks in the hexagonal layer. Similarly, the bands at -4 eV clearly split in two bands in the network. Although less pronounced, also bands at -8, -10 and -12 eV undergo a kind of splitting when involved in H-bonds interactions. In the bottom graph of Figure 6 the theoretical curves are decomposed in the contributions coming from the orbitals (pz, px, py) of each N atom. In this way, the analysis of the valence band can elucidate the effects induced by the H-bonds, in a similar fashion to the XPS investigation. Starting from the isolated molecule, one can see that the HOMO is double degenerate with π symmetry and mainly localized on the nitrogen atoms of both types, aminic and triazinic. The following HOMO-1 orbitals have still π symmetry. The quasi degenerate HOMO-2/HOMO-3 have σ character and they contain the triazine N lone pair. The latter is also contributing to HOMO-6. When looking at the PDOS of the H-bonded network, we can see that all orbitals that comprehend the lone pairs of triazine nitrogen atoms undergo a certain splitting and it is important to notice that these orbitals have a σ symmetry and are those involved in the H-bonding interaction (they accept the H atom). On the other hand, π orbitals, like HOMO, HOMO-1 or HOMO-4/5, do not present such an effect of splitting. The sigma bands involving the amino terminations (the H donor) also experience a kind of splitting similar to that of the bands containing the triazine lone pairs. All these results obtained in this first spectroscopic characterization of H-bonding in melamine molecules indicate that there are significant fingerprints of this weak interaction that can be easily followed by XPS, NEXAFS and possibly UPS spectroscopies.

.

3.4 TOWARDS MIMICKING PHOTOCATALYTIC REACTION: WATER-MELAMINE INTERACTION

In order to explore the potential photocatalytic properties of melamine towards the water-splitting reaction, we investigated the electronic properties of the water/melamine interface, by dosing water molecules on top of melamine films. It should be highlighted that both the melamine-melamine and melamine-water H-bonds are very important, since the first step of the photocatalytic reaction is an electron transfer from the H-bonded water to the aromatic ring, whose electronic properties and, in turns photoactivity, can be affected by the intermolecular interactions. Confirming this view, the p-CN shows much higher catalytic properties in amorphous state with respect to the crystalline phases where the active sites are locked in intramolecular H-bonds, and supposedly are less available to bind water molecules. To reduce the number of locked nitrogen sites, we have chosen Cu(111) as a substrate, where
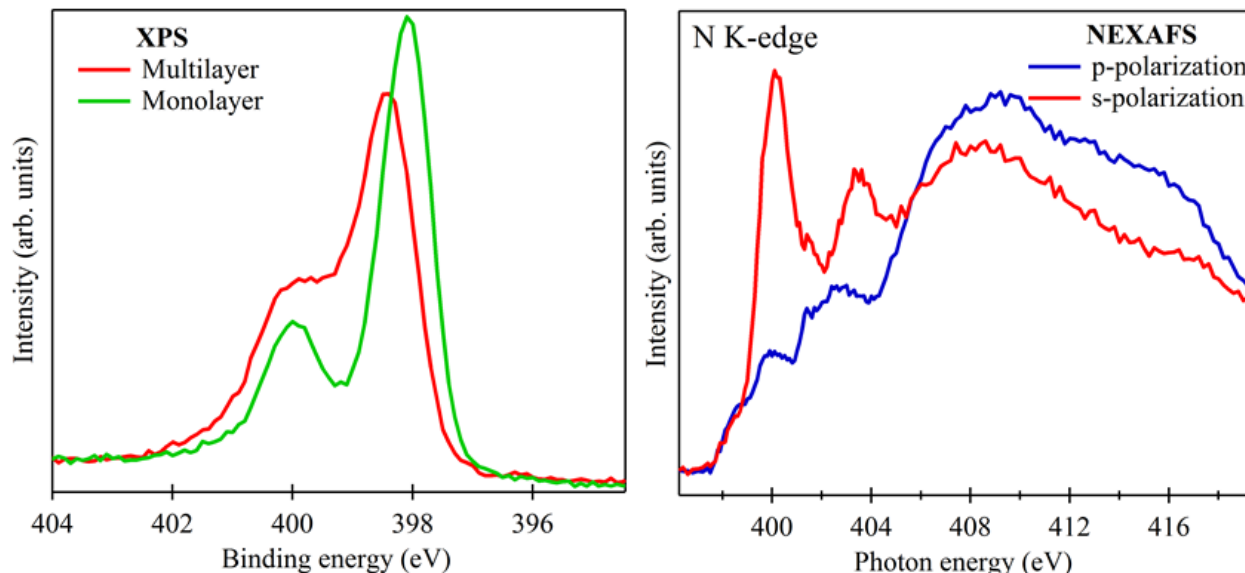
Figure 7: characterization of melamine on Cu(111). On the left, XPS of the thick film and of the monolayer. The measure has been taken with an overall resolution of 200 meV, with a photon energy of 650 eV. On the right, NEXAFS spectrum of the monolayer. The spectrum has been acquired in Auger yield with a window of 10 eV centered on 381 eV.6.

melamine is known to adsorb almost perpendicular to the surface.[44] Under these conditions, the outer nitrogen sites, both amino and triazine N, are free to possibly link water molecules. Preliminary characterization of the system has been made by XPS and NEXAFS techniques. Spectra related to the organic film without water are reported in figure 7. The N1s XPS spectrum shows a comparison between a multilayer (possibly a bilayer) grown at RT and the monolayer obtained by annealing the thicker film at the sublimation temperature of the molecule (390 K). The NEXAFS corresponding to the monolayer shows a valuable dichroism, confirming an adsorption geometry with the molecular plane almost perpendicular to the surface. The N1s XPS signal of the monolayer sample presents two rather broad peaks distant 1.8 eV from each other. It is not trivial to attribute the peaks to the different nitrogen atoms, since the standing up adsorption geometry breaks the equivalence between the three amino groups, as well as

between the aromatic nitrogen atoms. The result is similar to the one reported by Lin *et al.* where also attributions of peak positions have been clarified.[44] According to this reference, the amino terminations in contact with the surface are partially dehydrogenated, and thus contributing together with the triazine N to the peak at lower BE. On the other hand, the free amino group pointing towards the vacuum side contributes to the peak at higher BE.
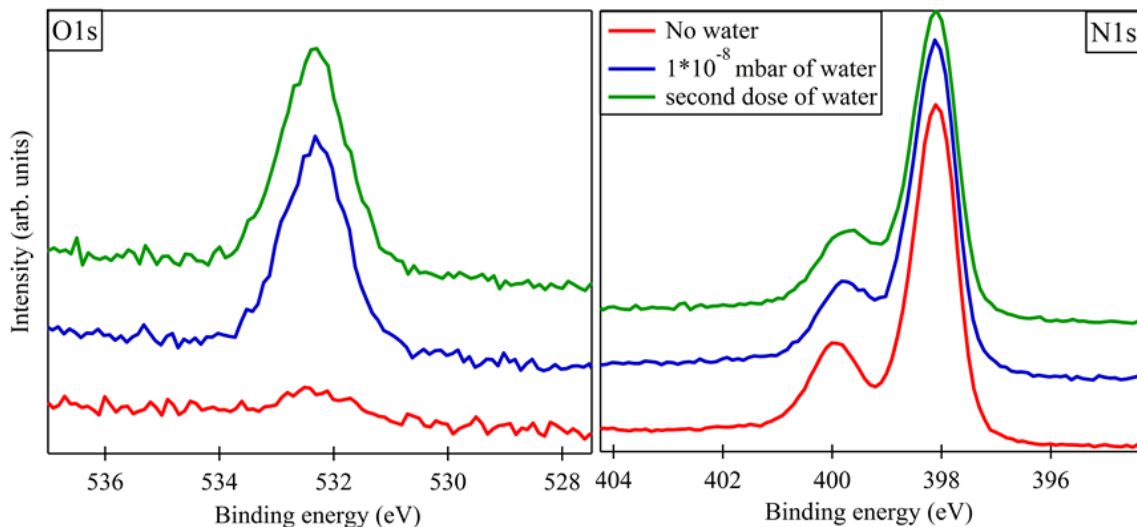

Figure 8: XPS of the melamine and water system. The measure has been taken with an overall resolution of 200 meV, with a photon energy of 650 eV.

The water deposition has been done dosing water in small amounts in the chamber with the sample kept at 170 K. The XPS analysis of this experiment is reported in figure 8, showing both the O1s and the N1s signals. The addition of water on the molecular film (testified by the appearance of the O1s peak) causes a slight shift to lower BE (ca. 0.2 eV) of the peak at 400 eV that, as mentioned before, has been associated with the amino group pointing towards the vacuum side. Such a shift can be interpreted as the formation of a hydrogen bonding between the amino termination and the water molecules. The first dose of water (roughly 30 s at 10^{-8} mbar, 0.3 L, with a base pressure of 10^{-10} mbar) leads to saturation of the surface, since a second dose at the same conditions did not affect the spectrum. The water film on the melamine layer is stable only at low temperatures and starts to desorb at 200 K. Interestingly, the shift of the amino N signal is toward the same direction as for the H-bonded network on Au(111) with respect the gas phase. In the H-bonded network, the amino group was the donor while the aromatic nitrogen was the acceptor.
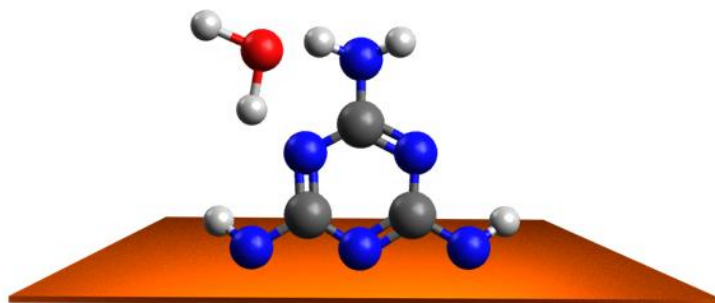

Figure 9: proposed model for the Cu(111)/melamine/water system. The amino group is acting as H donor, while the triazinnic nitrogen is acting as H acceptor interacting with a water molecule.

Even if more data in support are strongly requested, it is possible to advance the hypothesis that the two nitrogen atoms play the same role also in the presence of water. In particular, the aromatic nitrogen could be the acceptor of the H atom of water, while the amino one acts as the H-donor. A possible interaction geometry is reported in figure 9.

To obtain a deeper insight in the melamine and water system, it is necessary to perform a theoretical investigation. In conclusion, the work on melamine indicates the presence of a measurable effect of water molecules on the molecular film depicting the influence of the H-bonds. The importance of this results is to provide a spectroscopic benchmark of the "static" interaction between the melamine and water, with the possibility to explore the system under ultraviolet radiation, as its *operando* conditions. Since the formation of the H-bond has been proposed to be the first step of the photocatalytic water splitting reaction with carbon nitrides[45,46] and its precursors[27,29] and possesses specific spectroscopic fingerprints, water/melamine appears to be suitable references for investigation of the reaction.

3.5 MELEM

Parallel to the work on melamine, we have also performed some preliminary characterization of the melem molecule (1,3,4,6,7,9,9b-heptaazaphenalene-2,5,8-triamine), the other precursor or building block of carbon nitride polymers. The investigation is specular to that reported for the melamine molecule, as we have studied melem in gas phase and adsorbed on Au(111). At variance with melamine, STM investigation have been also performed for 1 ML of melem/Au(111). The spectroscopic results of these experiments are reported in figure 10 (XPS) 11 (UPS) and 12 (NEXAFS). Unfortunately, the gas phase
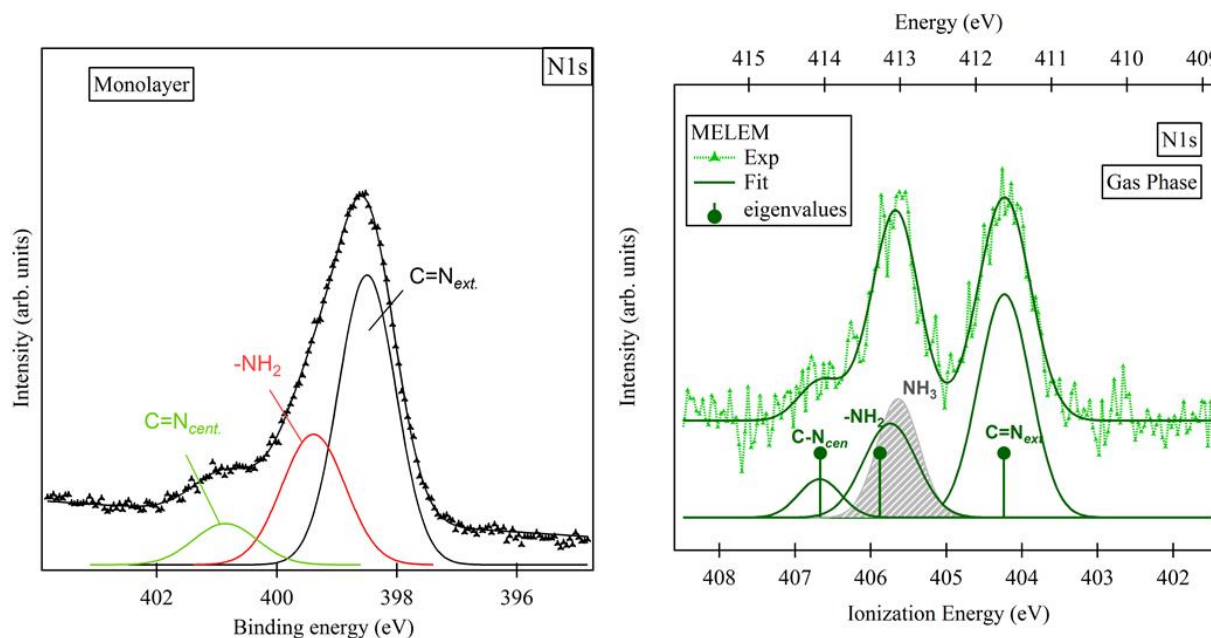

Figure 10: XPS of melem molecule. On the left the experiment on Au(111) covered with one layer of molecules. The peak has been deconvoluted to the contribution of the aromatic nitrogen present in the periphery of the molecule labeled as Next, whereas the nitrogen in the middle of the molecule has been labeled as Ncen. The same analysis has been performed for the gas phase data.

N 1s data (XPS and NEXAFS) are rather blurred by the strong contribution coming from ammonia. This is

70

due to the concomitance between the sublimation process and further condensation reactions between molecules in the crucible that release NH_3. On the other hand, the ammonia does not stick on gold at our experimental conditions (sample kept at room temperature during deposition). Gas phase core level
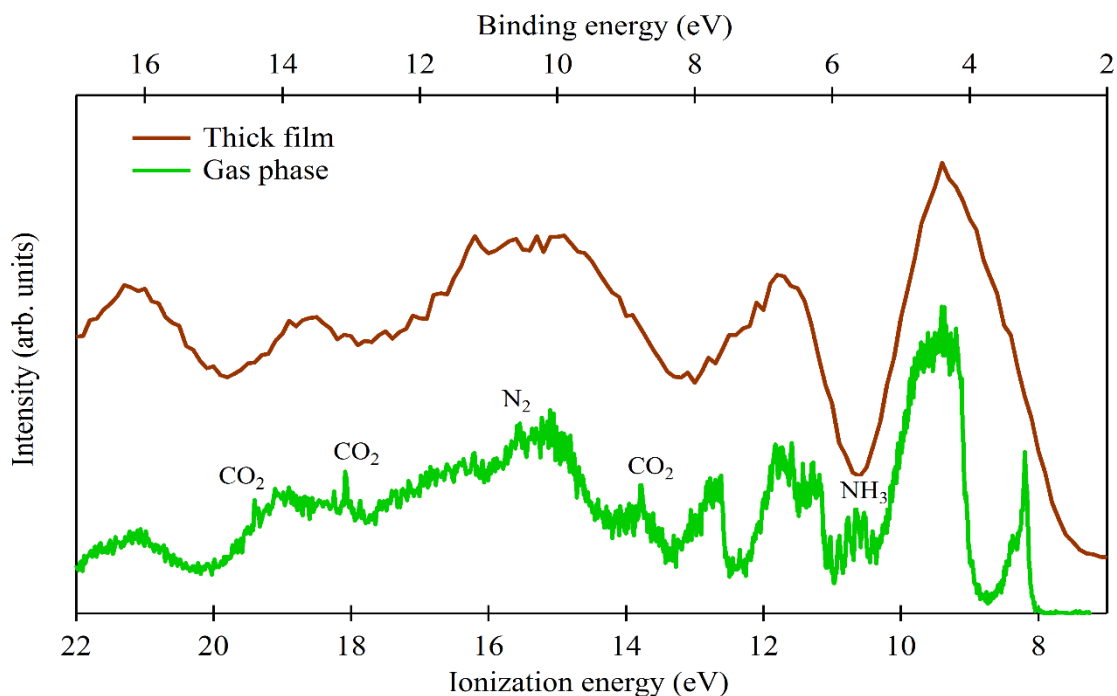

Figure 11: Valence band of the melem molecule. The thick film is referred to the top X scale, the binding energy, while the gas phase signal is reported with respect the ionization energy, in the bottom scale. The labels reporting the contaminations from other gases present in the chamber refer to the gas phase only.
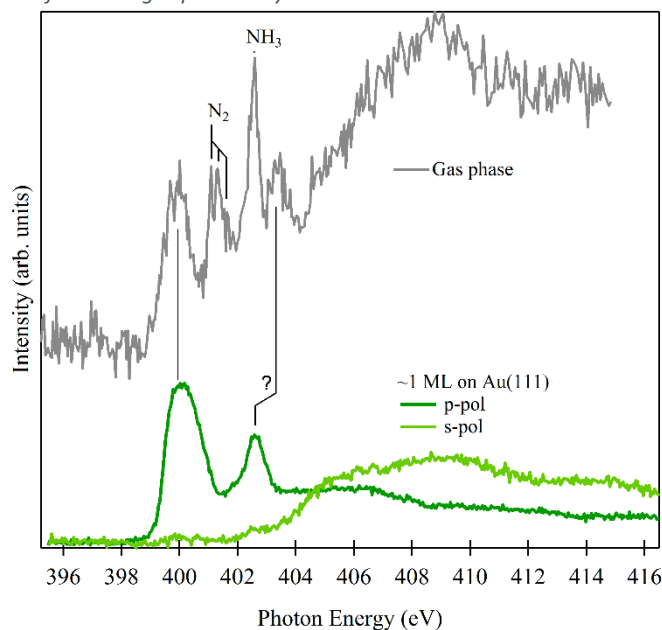
Figure 12: NEXAFS of melem, the gas phase measurement shows contributions from other species.

spectra (XPS, NEXAFS) are compared with those obtained for ca. 1 ML of Melem/Au(111), while the VB spectrum with that obtained for a thick film. By

disentangling the ammonia XPS signal (at 405.6 eV),[47] it has been possible to detect that also in this case
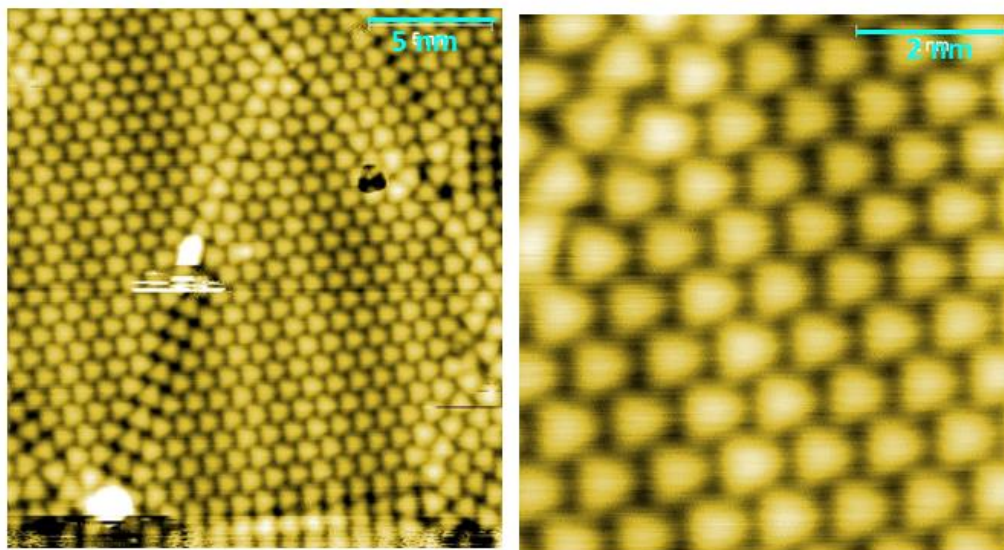

Figure 13: STM image of a monolayer of melem on Au(111). For the image on the left I= 40 pA and V=-2.0 V, and for the right image I= 40pA and V=-1.0V

intermolecular H-bonding interactions determine a decrease of ca. 0.7 eV between the amino and heptazine N 1s levels, relative to the non-interacting system. Unfortunately, the N K-edge NEXAFS spectrum is disturbed not only by the ammonia signal but also by the residual N_2 of the chamber preventing us to clearly distinguish differences between gas phase and the solid state spectrum. On the other hand, the dichroism of 1 ML sample confirms a flat adsorption geometry on Au(111) as shown by the reported STM images in accordance with previous STM investigation.[48]

To the core level spectroscopic investigation, we have added a valence band study, as reported in figure 11. Again, the gas phase experiment shows contaminations from ammonia, but also CO_2 and N_2 present in the chamber. For the sake of a better comparison between the two experiments, for the solid state, we have reported the thick film of the molecule on Au(111). The spectra show strong analogies, but for a deeper analysis, as in the case of melamine, a theoretical model is requested. In addition to the spectroscopic data, we have made also an STM investigation on melem/Au(111), see Fig. 12. The adsorption on Au(111) is flat confirming the NEXAFS analysis and the experiments reported in literature.[48] Contrary to melamine/Au(111), where molecules mainly self-assemble in honeycomb domains, in this case the melem molecules prefer to assemble in rows characterized by head-tail type H-bonds.

3.6 CONCLUSIONS

In conclusion, we have performed a combined multi-technique investigation to elucidate interesting properties of two carbon nitride precursor molecules. For the first one, melamine, a detailed characterization has been performed. The reported work shows a strong synergy between experimental data and the theoretical modeling allowing an important insight into properties of the molecule itself and into the characteristics induced by the presence of the H-bonding. The importance of this aspect becomes immediately clear if the photocatalytic water splitting mechanism is considered. In addition, we have tried

also to reproduce the catalytic conditions including water in the system. These promising results open the road for a deeper analysis in conditions more similar to the *operando* ones. For the second molecule, melem, we have performed a preliminary study only and further characterization will be necessary. The study is made more difficult by the intrinsic presence of some contaminants, like ammonia, during the gas phase experiments.

BIBLIOGRAPHY:

1.   Wang, X. *et al.* A metal-free polymeric photocatalyst for hydrogen production from water under visible light. *Nat. Mater.* **8,** 76–80 (2009).

2.   Su, F. *et al.* mpg-C$_3$N$_4$-Catalyzed Selective Oxidation of Alcohols Using O$_2$ and Visible Light. *J. Am. Chem. Soc.* **132,** 16299–16301 (2010).

3.   Schwinghammer, K. *et al.* Crystalline Carbon Nitride Nanosheets for Improved Visible-Light Hydrogen Evolution. *J. Am. Chem. Soc.* **136,** 1730–1733 (2014).

4.   Mansor, N. *et al.* Graphitic Carbon Nitride Supported Catalysts for Polymer Electrolyte Fuel Cells. *J. Phys. Chem. C* **118,** 6831–6838 (2014).

5.   Mansor, N. *et al.* Graphitic Carbon Nitride as a Catalyst Support in Fuel Cells and Electrolyzers. *Electrochim. Acta* **222,** 44–57 (2016).

6.   Di Noto, V., Negro, E., Vezzu, K., Bertasi, F. & Nawn, G. Origins, Developments, and Perspectives of Carbon Nitride-Based Electrocatalysts for Application in Low-Temperature FCs. *Interface Mag.* **24,** 59–64 (2015).

7.   Gillan*, E. G. Synthesis of Nitrogen-Rich Carbon Nitride Networks from an Energetic Molecular Azide Precursor. (2000). doi:10.1021/CM000570Y

8.   Miller, T. S. *et al.* Carbon nitrides: synthesis and characterization of a new class of functional materials. *Phys. Chem. Chem. Phys.* **19,** 15613–15638 (2017).

9.   Vyas, V. S., Lau, V. W. & Lotsch, B. V. Soft Photocatalysis: Organic Polymers for Solar Fuel Production. *Chem. Mater.* **28,** 5191–5204 (2016).

10.   Wu, M., Wang, Q., Sun, Q. & Jena, P. Functionalized Graphitic Carbon Nitride for Efficient Energy Storage. *J. Phys. Chem. C* **117,** 6055–6059 (2013).

11.   Jorge, A. B. *et al.* H$_2$ and O$_2$ Evolution from Water Half-Splitting Reactions by Graphitic Carbon Nitride Materials. *J. Phys. Chem. C* **117,** 7178–7185 (2013).

12.   Lin, J., Pan, Z. & Wang, X. Photochemical Reduction of CO$_2$ by Graphitic Carbon Nitride Polymers. *ACS Sustain. Chem. Eng.* **2,** 353–358 (2014).

13.   Ong, W.-J., Tan, L.-L., Ng, Y. H., Yong, S.-T. & Chai, S.-P. Graphitic Carbon Nitride (g-C$_3$N$_4$)-Based Photocatalysts for Artificial Photosynthesis and Environmental Remediation: Are We a Step Closer To Achieving Sustainability? *Chem. Rev.* **116,** 7159–7329 (2016).

14.   Algara-Siller, G. *et al.* Triazine-based graphitic carbon nitride: A two-dimensional semiconductor. *Angew. Chemie - Int. Ed.* **53,** 7450–7455 (2014).

15.   Kroke, E. & Schwarz, M. Novel group 14 nitrides. *Coord. Chem. Rev.* **248,** 493–532 (2004).

16.   Tyborski, T. *et al.* Crystal structure of polymeric carbon nitride and the determination of its process-temperature-induced modifications. *J. Phys. Condens. Matter* **25,** 395402 (2013).

17.   Franklin, E. C. THE AMMONO CARBONIC ACIDS. *J. Am. Chem. Soc.* **44,** 486–509 (1922).

18.   Lotsch, B. V & Schnick, W. From Triazines to Heptazines:? Novel Nonmetal Tricyanomelaminates as Precursors for Graphitic Carbon Nitride Materials. *Chem. Mater.* **18,** 1891–1900 (2006).

19.   Lotsch, B. V. *et al.* Unmasking Melon by a Complementary Approach Employing Electron Diffraction, Solid-State NMR Spectroscopy, and Theoretical Calculations—Structural Characterization of a Carbon Nitride Polymer. *Chem. - A Eur. J.* **13,** 4969–4980 (2007).

20.   Döblinger, M. *et al.* Structure elucidation of polyheptazine imide by electron diffraction—a templated 2D carbon nitride network. *Chem. Commun.* **0,** 1541 (2009).

21.   Wirnhier, E. *et al.* Poly(triazine imide) with Intercalation of Lithium and Chloride Ions [(C3N3)2(NHxLi1–x)3·LiCl]: A Crystalline 2D Carbon Nitride Network. *Chem. - A Eur. J.* **17,** 3213–3221 (2011).

22.   Mesch, M. B. *et al.* Solving the Hydrogen and Lithium Substructure of Poly(triazine imide)/LiCl Using NMR Crystallography. *Chem. - A Eur. J.* **22,** 16878–16890 (2016).

23.   Lau, V. W. *et al.* Low-Molecular-Weight Carbon Nitrides for Solar Hydrogen Evolution. *J. Am. Chem. Soc.* **137,** 1064–1072 (2015).

24.   Wei, W. & Jacob, T. Strong excitonic effects in the optical properties of graphitic carbon nitride g -C   3   N   4   from first principles. *Phys. Rev. B* **87,** 085202 (2013).

25.   Ilic, S., Zoric, M. R., Kadel, U. P., Huang, Y. & Glusac, K. D. Metal-Free Motifs for Solar Fuel Applications. *Annu. Rev. Phys. Chem.* **68,** 305–331 (2017).

26.   Merschjann, C. *et al.* Photophysics of polymeric carbon nitride: An optical quasimonomer. *Phys. Rev. B* **87,** 205204 (2013).

27.   Ehrmaier, J., Janicki, M. J., Sobolewski, A. L. & Domcke, W. Mechanism of photocatalytic water splitting with triazine-based carbon nitrides: insights from *ab initio* calculations for the triazine–water complex. *Phys. Chem. Chem. Phys.* **20,** 14420–14430 (2018).

28.   Meek, G. A., Baczewski, A. D., Little, D. J. & Levine, B. G. Polaronic Relaxation by Three-Electron Bond Formation in Graphitic Carbon Nitrides. *J. Phys. Chem. C* **118,** 4023–4032 (2014).

29.   Ehrmaier, J., Karsili, T. N. V., Sobolewski, A. L. & Domcke, W. Mechanism of Photocatalytic Water Splitting with Graphitic Carbon Nitride: Photochemistry of the Heptazine–Water Complex. *J. Phys. Chem. A* **121,** 4754–4764 (2017).

30.   Weinberg, D. R. *et al.* Proton-Coupled Electron Transfer. *Chem. Rev.* **112,** 4016–4093 (2012).

31.   Blyth, R. . *et al.* The high resolution Gas Phase Photoemission beamline, Elettra. *J. Electron Spectros. Relat. Phenomena* **101–103,** 959–964 (1999).

32.   Giangrisostomi, E., Ovsyannikov, R. & Sorgenfrei, F. LowDosePES: the low-dose photoelectron spectroscopy end-station at the PM4 beamline at BESSY II. *J. large-scale Res. Facil. JLSRF* **4,** A130 (2018).

33.   Floreano, L. *et al.* Performance of the grating-crystal monochromator of the ALOISA beamline at the Elettra Synchrotron. *Rev. Sci. Instrum.* **70,** 3855 (1999).

34.   Payne, M. C., Teter, M. P., Allan, D. C., Arias, T. A. & Joannopoulos, J. D. Iterative minimization

techniques for *ab initio* total-energy calculations: molecular dynamics and conjugate gradients. *Rev. Mod. Phys.* **64,** 1045–1097 (1992).

35.   Kohn, W. & Sham, L. J. Self-Consistent Equations Including Exchange and Correlation Effects. *Phys. Rev.* **140,** A1133–A1138 (1965).

36.   Jones, R. O. & Gunnarsson, O. The density functional formalism, its applications and prospects. *Rev. Mod. Phys.* **61,** 689–746 (1989).

37.   Kresse, G. & Hafner, J. *Ab initio* molecular dynamics for open-shell transition metals. *Phys. Rev. B* **48,** 13115–13118 (1993).

38.   Kresse, G. & Joubert, D. From ultrasoft pseudopotentials to the projector augmented-wave method. *Phys. Rev. B* **59,** 1758–1775 (1999).

39.   Silly, F. *et al.* Melamine Structures on the Au(111) Surface. *J. Phys. Chem. C* **112,** 11476–11480 (2008).

40.   Xu, W. *et al.* Cyanuric Acid and Melamine on Au(111): Structure and Energetics of Hydrogen-Bonded Networks. *Small* **3,** 854–858 (2007).

41.   P. A. Staniec, †, L. M. A. Perdigão, †, B. L. Rogers, †, N. R. Champness, ‡ and & P. H. Beton*, †. Honeycomb Networks and Chiral Superstructures Formed by Cyanuric Acid and Melamine on Au(111). (2006). doi:10.1021/JP064964+

42.   Cossaro, A. *et al.* Tailoring SAM-on-SAM Formation. *J. Phys. Chem. Lett.* **2,** 3124–3129 (2011).

43.   O'Shea, J. . *et al.* Hydrogen-bond induced surface core-level shift in pyridine carboxylic acids. *Surf. Sci.* **486,** 157–166 (2001).

44.   Lin, Y.-P. *et al.* Self-Assembled Melamine Monolayer on Cu(111). *J. Phys. Chem. C* **117,** 9895–9902 (2013).

45.   Wu, H.-Z., Liu, L.-M. & Zhao, S.-J. The effect of water on the structural, electronic and photocatalytic properties of graphitic carbon nitride. *Phys. Chem. Chem. Phys.* **16,** 3299 (2014).

46.   Wirth, J., Neumann, R., Antonietti, M. & Saalfrank, P. Adsorption and photocatalytic splitting of water on graphitic carbon nitride: a combined first principles and semiempirical study. *Phys. Chem. Chem. Phys.* **16,** 15917–15926 (2014).

47.   Bakke, A. A., Chen, H.-W. & Jolly, W. L. A table of absolute core-electron binding-energies for gaseous atoms and molecules. *J. Electron Spectros. Relat. Phenomena* **20,** 333–366 (1980).

48.   WANG, L., SHI, H.-X., WANG, W.-Y., SHI, H. & SHAO, X. Identifying the Hydrogen Bonding Patterns of Melamine and Melem Self-Assemblies on Au (111) Surface. *Acta Physico-Chimica Sin.* **33,** 393–398 (2017).

CHAPTER 4 COMPLEX SYSTEMS

4.1 INTRODUCTION

In the final part of this Phd thesis, we have explored the possible use of 2D molecular systems as templates for the formation of guest-host architectures on surfaces. Supramolecular chemistry on surface is a widely studied field.[1] Most of the works in literature are however focused on the study of the morphology of the systems. We present spectroscopy studies performed on complex architectures, aimed at evidencing the selectivity of the interactions we promoted between different components of the systems. We have studied two distinct architectures, exploring two interacting schemes of different nature. The first one is related to the study of boroxine based frameworks. In particular, we have considered the boroxine rings as possible Lewis acid sites on the surface and we have investigated their possible interaction with a Lewis base, namely an amino-terminated molecule. As it will be shown in the following paragraphs, we successfully promoted the formation of the amino-boroxine interaction scheme, opening to the intriguing perspective to adopt the boroxine rings of a 2D architecture as docking platform for amino-terminated guest molecules. In the second system presented in this chapter we have moved to a rather different system. In a previous work performed in our group, a regular nanoarray of crown ether molecules was obtained.[2] Here we have investigated the chemical state of the crown ethers, in particular we have verified if they preserve the affinity towards the alkali atoms they are known to have when used in solution.[3] By means of photoemission spectroscopy we show that the trapping of Na atoms is successfully obtained. This result not only demonstrates the possible adoption of crown molecules as active ion traps under UHV but, together with previous results on these systems, describes how finely the chemistry of a 2D system can be characterized at each formation step, from the functionalization of a metallic surface with sites suitable for anchoring a guest molecule, to the employment of the latter as active receptor of atomic species.

4.2 AMINE-BOROXINE RECOGNITION: INTRODUCTION

The monolayer of trinaphtylboroxine (TNB) we described in section 7 of chapter 2 is the system we selected to investigate the boroxine properties as Lewis acid.[4] As Lewis base, we have chosen an amine, which behaves as a base in its neutral state, differently from many other negatively charged bases, and can be therefore adopted under UHV and not only in solution. Moreover, according to the hard and soft acids and bases distinction,[5] the boronic acids and esters can be classified as hard acids, and the amine is a hard base, which would enhance the stability of the possible acid-base adduct.[6–8] Among the different amines, we have chosen 1-naphtalen methylamine (NMA), figure 1. First of all, we have preferred to operate with an aliphatic amine, for higher basicity with respect to an aromatic amine.[9] In addition, this compound has already been deeply investigated in our group, its assembly on the Au(111) surface has been described.[10] As boroxine-based Lewis acid, we have selected the TNB among the boroxine based
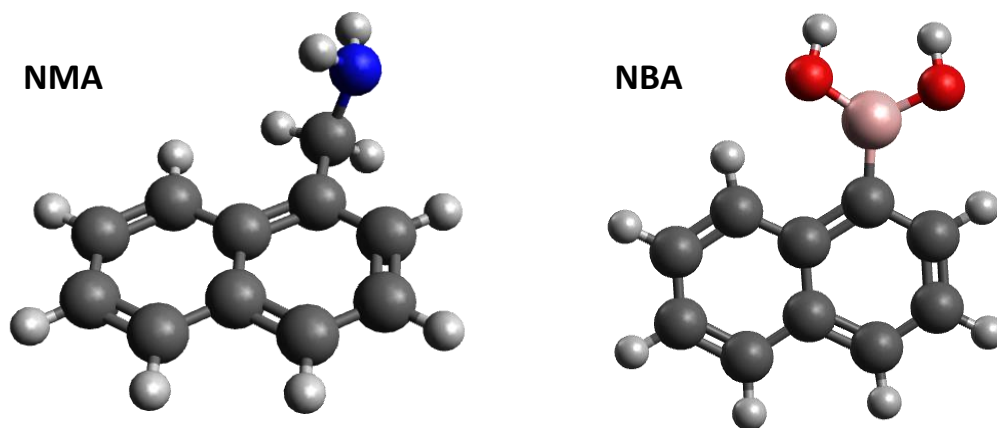
Figure 1: on the left is reported the 1-naphtalen methylamine (NMA), and on the left is represented the 1-naphtylboronic acid (NBA) which has been used to form condensed trimers, TNB (trinaphtyl boroxine) on the surface. Black spheres represent carbon atoms, the blue one the nitrogen atom, pink sphere stands for the boron, the red spheres for oxygen atoms and white spheres for hydrogen atoms

systems that have been already discussed in previous chapters. First of all, we considered that the formation of the acid-base adduct could induce a change in the bond geometry of the involved boron atom from trigonal planar to tetrahedral. A good starting point for the monitoring of the interaction would thus be a system of isolated molecules, free of constrains, rather than an extended polymer with a structure that may have some rigidity and apply resistance to this geometrical change. Both the NBA and PBA derived trimers we presented in chapter 2 represent in fact a boroxine platform on the surface, with well-defined spectroscopic properties. Since the NBA derivative, namely the TNB, is more thermally stable than the PBA one, we decided to start with it as prototype system for the study of the amino-boroxine interaction.

4.3 THE AMINE-BOROXINE RECOGNITION: RESULTS

We have deposited the NMA from a pyrex vial, since in vacuum it has a high vapor pressure at ambient temperature, on top of a TNB layer, formed as described in Chapter 2. By keeping the sample at room temperature, no sticking of the NMA was observed by XPS analysis. This is in agreement with what was discovered on the assembly of pure NMA on Au(111), where at room temperature only the saturation of the monolayer was obtained,[10] and the formation of a second layer was possible only at lower temperatures. Following these indications, we deposited the NMA on the TNB layer at 260 K. The XPS spectra are reported in figure 2. B1s, C1s, N1s and O1s signals are reported as taken: on the TNB film (black lines); on the NMA/NBA interface measured upon the NMA deposition (green line) and upon annealing of the sample at 320 K. By inspecting the boron signal first, B1s has a main peak at 191.3 eV, similarly to the condensed PBA case, and a minor component at higher energies, which is seen to increase with beam irradiation and has therefore to be related to possible damaging of the TNB. For this reason, the presented spectra have been taken immediately after moving the sample to analyze fresh spots at every stage. Upon NMA deposition, a shift of 0.3 eV toward lower binding energies is present, suggesting a change in chemical environment of boron atoms. The peak related to the damaging is not visible here and the overall intensity decreases, due to the attenuation of the signal by the NMA over-layer. Finally,

upon annealing above RT (320 K) the main component is found back to its initial position and intensity.
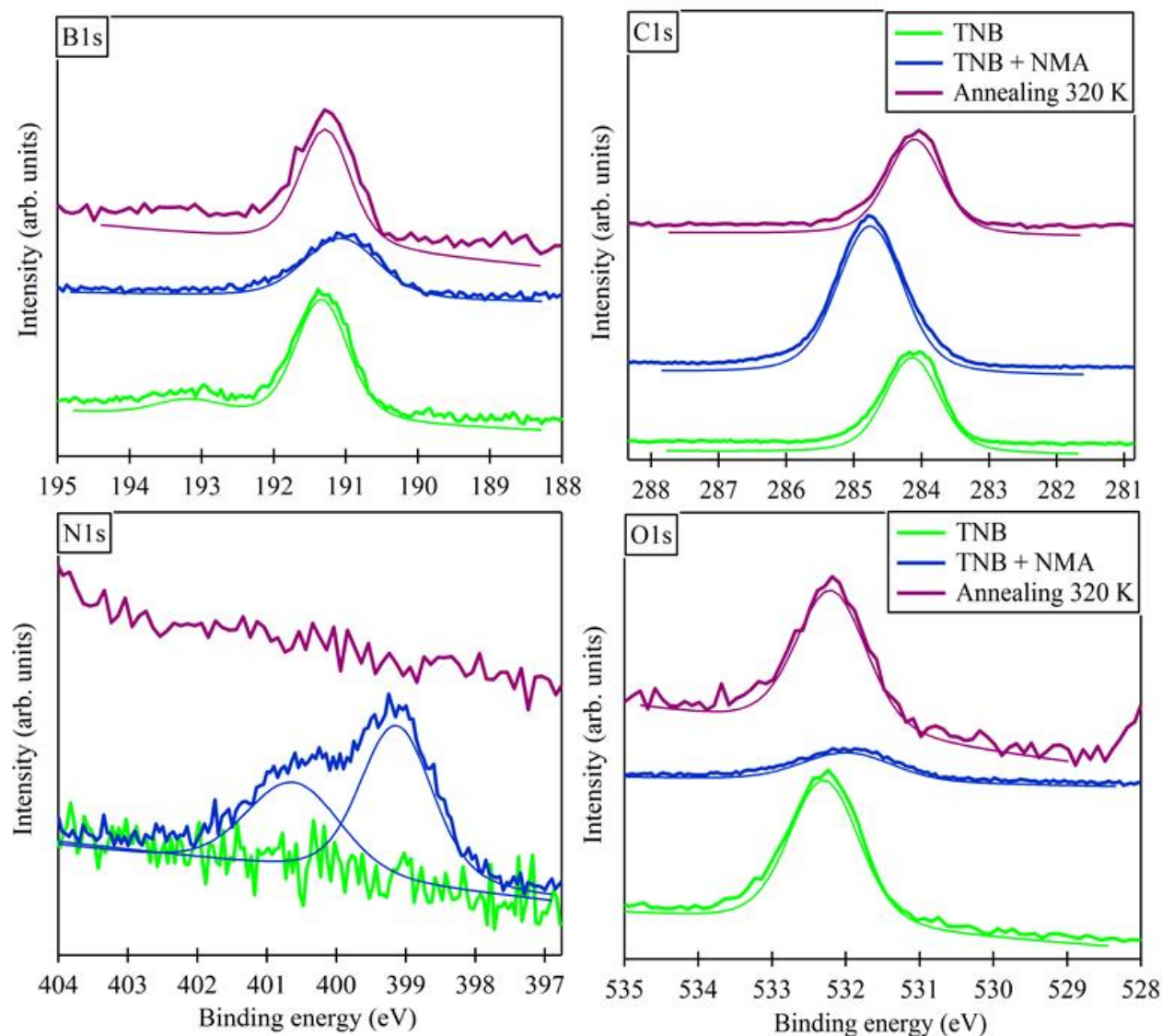

Figure 2: XPS spectra of the condensed NBA with MNA molecules on top, on Au(111). The C1s and N1s have been acquired with 515 eV of photon energy, while O1s has been taken with photons at 650 eV and B1s has been probed with a 300 eV light. The pass energy employed was 20 eV.

Proceeding with the C1s spectrum, the comparison before and after the NMA deposition reveals a large increase in the carbon concentration on the surface, due to the carbon content of NMA. The shift to higher BE can be attributed to the lower screening effect experienced by the electrons emitted by NMA molecules, that are at larger distance from the surface. The situation is restored upon annealing at 320 K, with the recovery of the pristine TNB spectrum. The N1s spectrum taken upon NMA deposition shows two different components. Again, the annealing to 320 K restores the situation before the NMA deposition, with no nitrogen signal. Finally, the O1s spectrum shows a shift in BE toward lower values of 0.3 eV, in the same fashion as B1s, occurring after the NMA deposition. The presence of two N1s components supports a model where part of NMA molecules are anchored on the boroxine rings through the amine termination (N1s at 400.6 eV) and part are adsorbed without a chemical involvement of their

functional group, maybe directly on the Au(111) surface. This is supported by the position of one of the nitrogen peaks at 399.2 eV, which is in good agreement with the reference of NMA on clean gold, and of the second component at 400.6 eV, a value compatible with a lone-pair interacting amine.[10] The shift to lower binding energies of both B1s and O1s agrees with an electron doping of the boroxine ring. The
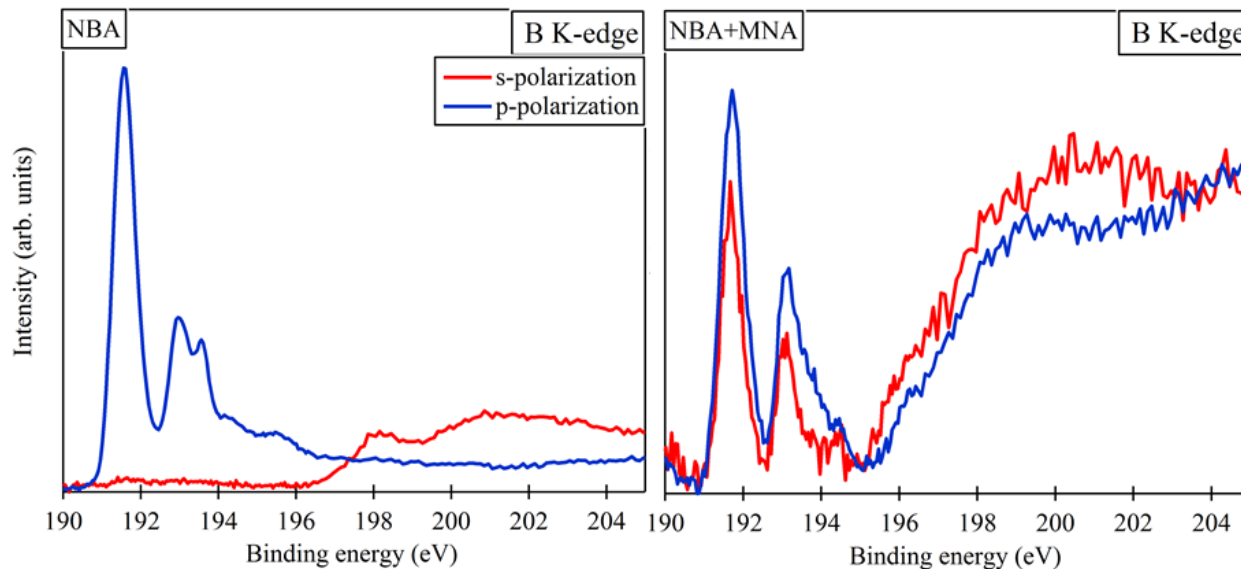

Figure 3: NEXAFS spectra of the NBA (left) after the boroxine formation reaction, showing a marked dichroism, and NBA with NMA molecules on top, presenting almost no dichroism. The spectra have been taken on the B Auger peak (183 eV) with pass energy of 50 eV of the electro analyzer.

overall behavior of the signals is therefore compatible with a formation of a bonding between the amine and the boroxine. It is not possible to state the exact point of anchoring of the amine on the boroxine ring, but from known behavior of the boroxine in other environments,[11] we propose that is the boron atom to play this role. The low temperature of desorption can be explained invoking the fact that the boronic acids are known to make not particularly strong complexes with Lewis bases.[12] A deeper investigation has been carried out with the NEXAFS spectroscopy on the B K-edge, reported in figure 3. As revealed by this characterization, in the TNB film the boroxine rings lie flat on the surface. The corresponding NEXAFS reveals a complete dichroism between the spectra acquired in the different polarizations. The situation is radically changed after the deposition of NMA. The dichroism is almost vanished, and the ratio between the first two peaks of the spectra is changed. The information retrieved from the NEXAFS is compatible with the model of a bond formation between boron and nitrogen. First of all, the boron is expected to adopt a tetrahedral geometry rather than trigonal planar, and a major change is seen in the dichroism. Moreover, as already evidenced by XPS, the bond is expected to be dative, with a certain electron donation from the nitrogen of the amino group (Lewis base) to boron (Lewis acid). The change in the NEXAFS peak ratio can be interpreted as a partial filling of the unoccupied orbitals localized on boron. On the other hand, it has to be said that this is a preliminary result and different interpretations for the morphologic change may be invoked. For instance, the NMA molecules may have intercalated in the boronic monolayer altering its geometry. Nevertheless, the change in the electronic properties of the system, revealed by both XPS and NEXAFS, indicate that a specific amino-boroxine interaction takes place and we propose a possible model of the interaction scheme in figure 4. In order to have a better insight in the system, further investigation is necessary. In particular, an STM study would be very helpful in
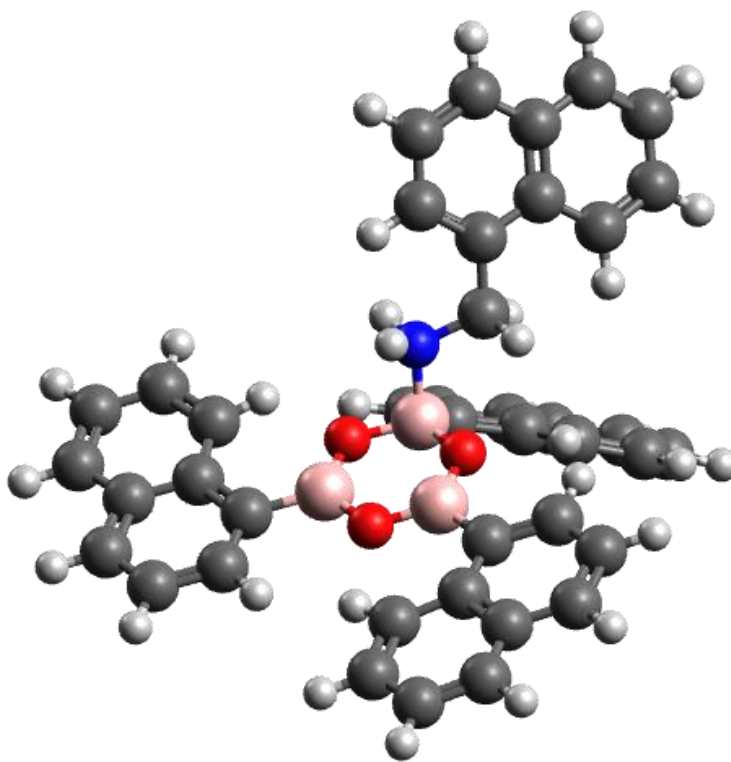
Figure 4: Proposed model for the interaction between the 1-naphtalen methylamine (NMA), and the trinaphthylboroxine, the trimer of the 1-naphtylboronic acid

determining the NMA-TNB morphology; a DFT calculation of the interacting system would support the scheme of figure 4 and confirm the charge donation occurring between the two molecules. In addition, it will be important to verify if the anchoring scheme we identified can be applied to other boroxine systems, like the boroxene or to change the amine molecule, using perhaps smaller molecules like ammonia to simplify the data analysis.

4.4 Crown Ether complex system

The second complex architecture studied in this thesis work extends an investigation already performed previously by the ANCHOR research group, exploring the possibility of using chemical functionalities to template a metallic surface.[2] In particular, it was proven that it is possible to employ a carboxylic acid to form an ordered and well-defined layer of a second, amino terminated molecule. The carboxylic functional
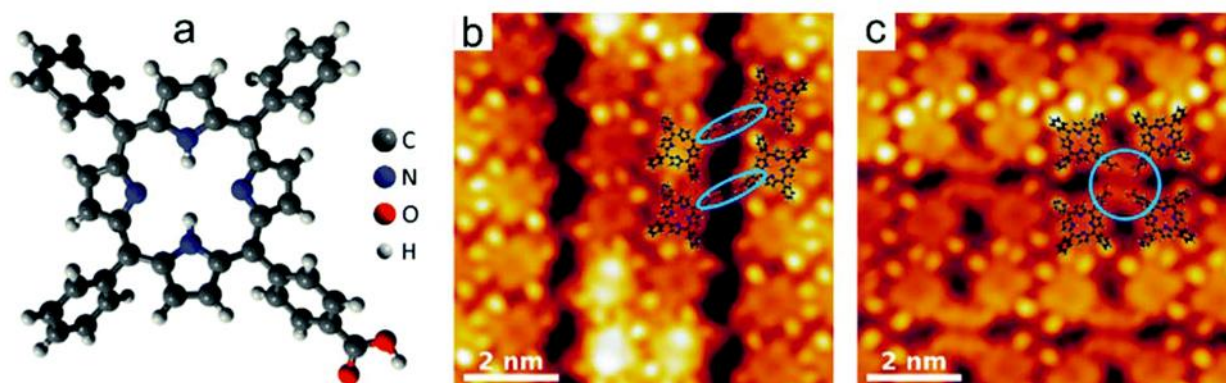

Figure 5: a) ball and stick model of 5-(4-carboxiphenyl)-10,15,20-(triphenyl) porphyrin (TPP), b) and c): deposition on Au(111) of TPP molecules leads to the formation of two distinct phases. The blue circles highlight the area of carboxylic decorated spot. The parameter of the STM images were: (b) V = −0.5 V, I = 1.0 nA. (c) V = −0.5 V, I = 0.5 nA. Image taken from ref 2.

group was carried by a porphyrin derivative, 5-(4-carboxyphenyl)-10,15,20-(triphenyl) porphyrin (TPP), reported in figure 5. This molecule assembles in an ordered structure on the surface, forming centers with four carboxylic terminations facing together, present in two different coexisting phases on surface (fig. 5b and 5c respectively). These centers act as anchoring sites for an amino terminated molecule deposited on top of such a system. As amino terminated molecule, a crown ether derivative was employed, the 1-(1,4,7,10,13-pentaossacyclopentadecan-2-il) methylamine, reported in figure 6. It is important to state that this second molecule does not form ordered assembly on the clean gold surface, yielding disordered
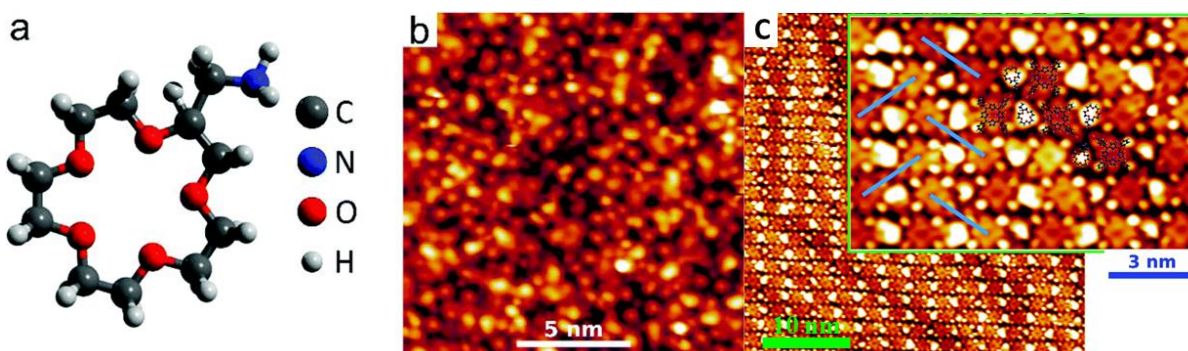

Figure 6: a) ball and stick representation of the 1-(1,4,7,10,13-pentaossacyclopentadecan-2-il) methylamine, the crown ether molecule employed in this experimental session, b) STM image of the Au(111) surface after a direct deposition of the crown ether showing an irregular phase. STM image parameters: (b) V = −0.2 V, I = 0.02 nA c) STM image of the crown ether deposited on the TPP array that imposes an ordered geometry, V = −0.2 V, I = 2.0 nA both. Image taken from ref 2.

films instead. On the contrary, when deposited on the carboxylic template, crown molecules are found to assemble in an ordered 2D array (fig. 6c), the growth being driven by the amino-carboxylic interaction between the crown amino termination and the carboxylic centers of the template. The use of a crown

ether enabled us to study the peculiar chemical behavior of these compounds, already known in solution environment, under ultra high vacuum conditions. The crown ethers were studied for the first time by Pedersen[13] in the sixties, and since then they have been widely adopted in many fields. They are known to establish strong interactions with metallic ions, and in particular with alkali ones, which make them interesting for many wet chemistry applications.[3] The interesting aspect of this neutral ligand – metal ion affinity is the shape-matching dependence typical of host-guest systems that allows to obtain a discrete selectivity toward different ions. They can be successfully employed in analytical chemistry in many fields such as solvent extraction, ion selective electrodes,[14] and chromatography where they can be used in the mobile or stationary phase.[15,16] This chromatographic use is not restricted to the metal ions, but the crown ethers can also provide chirality to the stationary phase of a chromatographic column in order to separate enantiomers of important biological compounds.[17] Another remarkable use of the crown ethers lies in the mimic of biological processes.[18] In particular, this class of macrocyclic molecules are often exploited for the creation of models for ion channels to elucidate the natural transport in cells as well as to understand the possible evolution of this crucial process in the early cellular forms.[19,20,21] Moreover, special attention has been given to the study of molecules containing crown ether and porphyrin macrocycles. Many molecules of this class have been synthesized, as reviewed by Even,[22] exploring a high number of different linking possibilities between the porphyrin and crown ether subunits. A lot of efforts have been spent in the study of these compounds in the catalysis, for instance epoxidation of styrene[23] and 1-dodecene,[24] or in the visible region sensing of anions and cations,[25] indicating a strong interest in the synergy between the porphyrins and crown ethers. Alternatively, crown ethers have been also employed in the preparation of nanostructured hybrid materials.[26] Combining this structural approach with the analytical field, Kuang et al. have designed an intriguing sensor based on gold nanoparticles modified by crown ether containing thiol molecules. The sensor relied on the ability of melamine molecules, the ones studied in the previous chapter, to interact simultaneously with more crown ethers linking thus the nanoparticles together.[27] The interaction between the crown ether and the amino group in its charged (ammonium ion) state has proven its utility in building complex nano-architectures on gold surfaces in solution as well. In particular, Arias et al. have functionalized with cystamine a gold electrode and subsequently anchored a crown ether functionalized C_{60} molecule.[28] A similar structure can be found in the work of Miura where the same kind of interaction has been exploited for the formation of monolayer and of multilayer structures of α-helix peptides on gold substrate.[29] Other works, instead of using the crowns as anchoring agent, were focused on the study of crown chemistry on the surface.[30,31] This means that another functional group was used to anchor the crown ether derivative to the surface, leaving the ether free of interaction from the substrate. All these works demonstrate the interest of the nano-fabrication community towards this class of compounds. The approaches reported in literature are different from ours. We have used a first molecule to act as templating agent and then the crown ether has been anchored via an amino-carboxylic interaction, instead of creating a direct bond between the substrate and the ether. The interposition of the carboxylic template not only drives the assembly of the crowns into a regular array but also possibly prevents their interaction with neighbors or with the substrate. In addition, we have adopted UHV working conditions, innovative for these compounds which are necessary for the study of the interaction disentangled from spurious effects induced by the presence of solvent molecules.[32] The objective of the work presented here is to establish if the chemical properties of the crown ethers are preserved in this system. In particular we have investigated the most interesting and exploited property of these compounds, i.e. their capability to trap metal ions. It has to be taken in mind that the deposition of an alkali metal on top of an organic layer can be also seen as a way for doping the film, in a way already

reported for phthalocyanines.[33] It has to be highlighted that our system has two possible sites for anchoring sodium. One in the crown ether that is studied, but also the porphyrin molecule used as a templating agent is a possible interaction site. From this point of view, it appears interesting to monitor which is the most favorable site for the metal atoms to be trapped.

4.5 EXPERIMENTAL

For this experiment we have employed the 5-(4-carboxyphenyl)-10,15,20-(triphenyl) porphyrin purchased from Porphychem, purity >98%. The deposition has been performed from a ceramic crucible heated to 570 K on a sample at room temperature, cleaned with sputtering and annealing cycles. The 1-(1,4,7,10,13-pentaossacyclopentadecan-2-il) methylamine, from Sigma Aldrich, purity >95%, liquid at ambient temperature, has been deposited from a glass tube, separated from the chamber from an all-metal valve. No heating was needed. Metallic sodium has been dosed on the sample from an alkali metal dispenser, from SAES Getter. The quantity of deposited sodium had to be checked after each deposition acquiring the Na 2p peak. In order to express in a convenient way the amount of the alkali metal on the surface, a sodium dose has been introduced depositing it on a clean gold surface and measuring the XPS signal of Na2p and Au4f. Taking into account only the surface component of the gold peak and the different cross-sections it has been possible to determine that a "Na dose" correspond to 1 Na atom per 60 ± 5 superficial atoms of gold, reported as θ_{Na} in the figures. For comparison with the remaining part of the system, the area covered by one TPP molecule has been extrapolated from an STM image. In good agreement with literature,[34] it corresponds roughly to 58 atoms of gold. The STM images have been acquired in collaboration with the group of prof. Comelli at Laboratorio TASC in Trieste.

4.6 RESULTS AND DISCUSSION

The characterization of the system started with the study of the porphyrin layer. We have deposited sodium on the TPP to have a reference without the crown ether. The XPS on the bare TPP layer, black curves in figure 7, shows the presence of two nitrogen peaks, as expected. The signal at higher binding energies corresponds to the iminic nitrogen (-NH-) while at lower binding energy is found the peak of the pyridinic nitrogen (=N-).[35] The C1s spectrum presents a single, rather broad peak with a shoulder at higher binding energy, as usually found for porphyrins.[36] The O1s presents a two peaks structure, that can be assigned to the carboxylic terminations of the template, involved in the autorecognition process.[37] The deposition of the sodium leads to considerable changes in the N1s region. The general trend is a shift of 0.7 eV of all the peaks toward higher binding energy (effect present also in the C1s spectra, evidenced by pink lines) and a change in reciprocal intensities of the nitrogen peaks at intermediate Na doses. On both the iminic and the pyridinic peaks it is evident that the broadening is originated by the presence of two distinct components, the pristine one and a high BE one. This behavior can be explained supposing that part of the porphyrins has been doped by Na atoms, causing a shift towards higher BEs of their photoemission lines. Our results are in accordance with literature data of deposition of potassium on

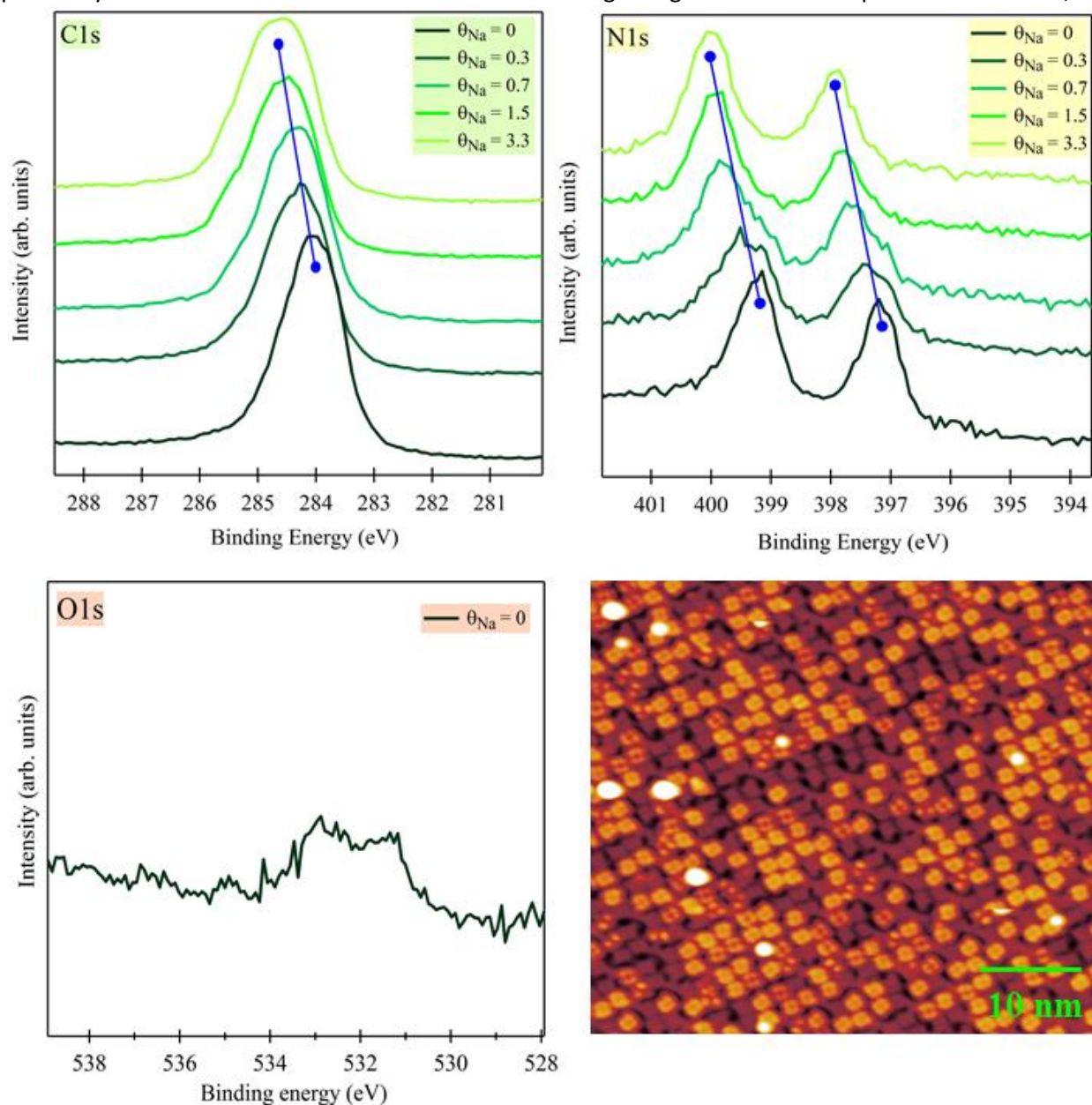phthalocyanines which leads to similar shifts in the binding energies.[38,39] As was explained in that case, an

Figure 7: XPS spectra of the TPP on Au(111) at growing quantity of Na, expressed respect to the Na dose, the θ_{Na} in the legends, corresponding to 1 atom of Na every 60 ± 5 surface atoms of gold. The C1s and N1s spectra have been taken with a photon of 500 eV of energy, whereas for the O1s an 650 eV beam has been used. The last image is the STM of the system, acquired with V_{smp} = 0.1V, I_a= 0.3 nA

electron from the alkali metal is delocalized on the hosting molecule filling of the LUMO and consequently lowering of the valence electronic states with respect to the Fermi level. Such a hypothesis is also supported by STM, which shows the presence of three types of TPP. The darker one can be regarded as a molecule not interacting with any Na atom, whereas the lighter ones are interacting with one Na and the bright spots are TPP molecules with two or more sodium atoms attached. It is important to stress out that, since the experimental chamber for XPS and for STM are different, it is not possible to make a correlation between the amounts of Na deposited in the two cases. We can suggest however that the change in the

iminic/pyridinic ratio we observe at the higher Na coverage can be related to the doubly doped porphyrins, whose nitrogen atoms may present a strongly different chemical behavior with respect to the pristine and singly doped molecules. This aspect is however beyond the aim of the present work. We see now instead how different the situation is when the Na is dosed on top of the complex crown-porphyrin system. Figure 8 reports the XPs and the STM image of this novel situation. Starting with N1s, there is a small peak at 401 eV that can be assigned to the amino termination of the crown ether anchored to the carboxylic centers.[40] The O1s region is characterized by an intense and large peak due to the five oxygen
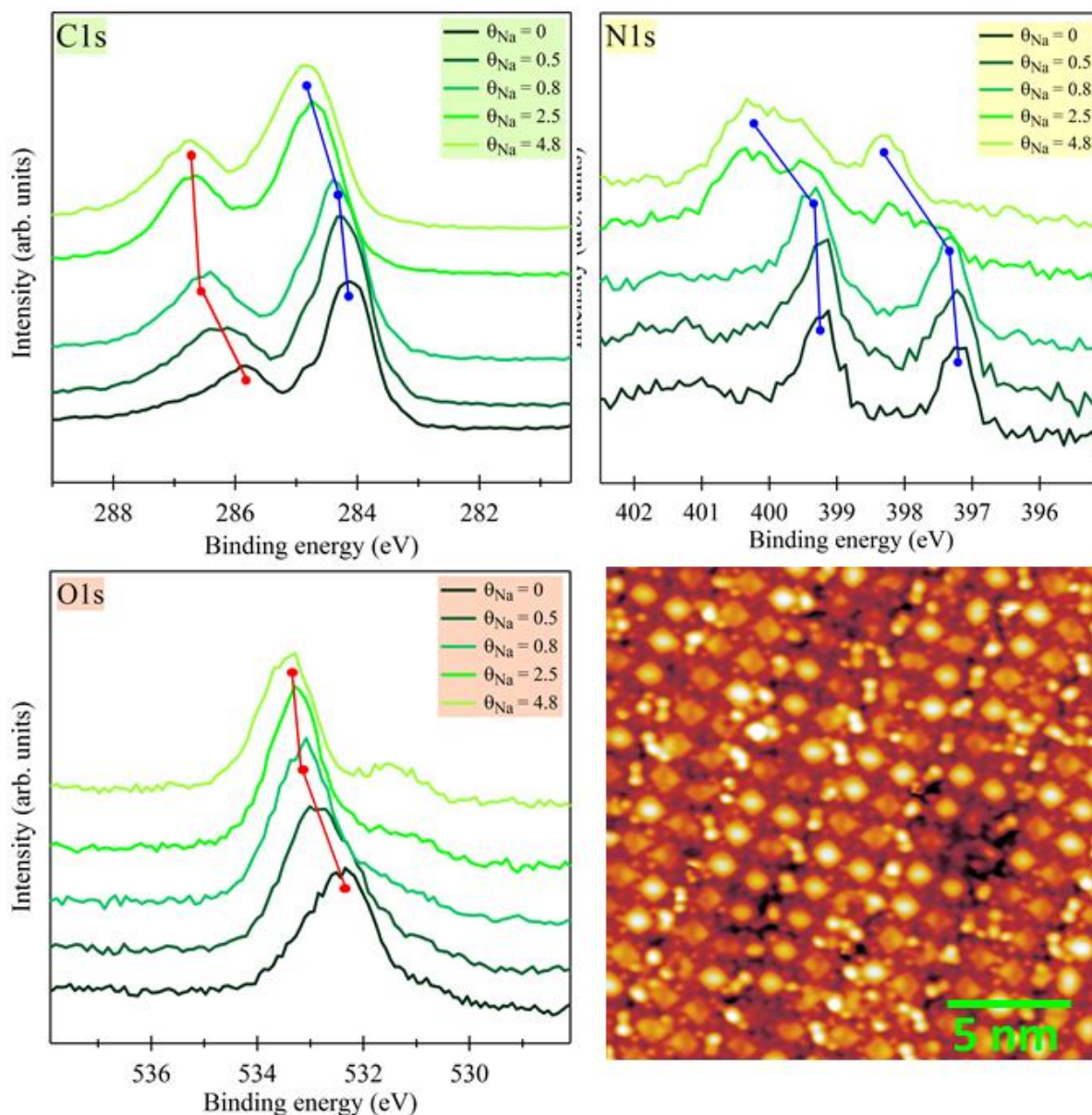
Figure 8: XPS spectra of the complex system of the porphyrin (5-(4-carboxyphenyl)-10,15,20-(triphenyl) porphyrin labeled as TPP), the crown ether (1-(1,4,7,10,13-pentaossacyclopentadecan-2-il) methylamine) and sodium. The STM image of such a system has been acquired with +0.1 V and 0.3 nA. As in the previous figure the sodium dose is reported in "sodium doses" labeled as θ_{Na}.

atoms present in the macrocycle, which covers the template peak discussed in figure 7. The broad signal

probably reflects an inequivalence of the oxygen atoms, induced by the interaction with the template and/or by the structural distortion the crown ether may undergo under UHV. A shoulder at lower energies (around 532 eV) is visible for high Na doses, corresponding to the underlying carboxylic centers as reported in figure 8, that are not affected by the doping. The C1s spectrum presents a significant contribution from both molecules, the TPP at lower binding energy and the crown at higher ones. The deposition of the sodium on top of this film revealed a very interesting behavior. The XPS spectra taken after deposition of small amounts of Na show changes in binding energy of the crown ether features only. In the oxygen spectrum, the peak is shifting toward a higher energy by 0.9 eV and presents a narrower profile. An analoguos situation can be seen in the C1s spectra where the first doses of alkali metal affect only the crown feature shifting it to higher energy of 0.9 eV. On the contrary, the N1s porphyrin components result unaffected by the Na presence and only a broadening/fading of the crown component at 401 eV is observed. The overall information that comes from the analysis of the XPS spectra suggests that an interaction between the sodium and the crown ethers takes place in the first stages of Na deposition, while the TPP template remains apparently unaffected. Finally, at higher loads of the alkali metal, the TPP features evolve as well. The C1s indicates that the TPP peak shifts of 0.7 eV toward higher binding energies, confirming the value obtained without the crown ether. An analogous situation is present in the N1s spectra. There is a shift toward higher binding energies comparable to the situation without the crown. In particular, at 2.5 Na dose, two N1s components coexist, corresponding to the doped and pristine TPP molecules respectively. The information that can be evicted from this dataset indicates a preference of the sodium to bind to the crown ethers instead of to the porphyrin. Indeed, the first changes in the spectra after sodium deposition are shown on the crown peaks, and, once the most of photoemission peaks of the crown has completed its transition toward a higher binding energy and can be regarded as Na saturated, the porphyrin starts changing showing the same behavior as in the absence of the second molecule. This scheme is confirmed by the STM image shown in lower panel of Figure 8. If compared with the image taken of the crown array before Na deposition, we notice that the appearance of the crown molecules has changed, being here bean-shaped rather than rounded. Whereas almost all of them appear modified, only part of the porphyrins underneath is made brighter by the Na intercalation. Again, this indicates the crown ethers as preferential trapping site for the alkali atoms. In conclusion, here we have demonstrated the possibility of employing a weak amino-carboxylic interaction to anchor molecules on surface and the subsequent use of these second layer to other interactions. Moreover, it has been demonstrated that the crown ethers retain their affinity toward the alkali metals that marks their properties and applications in solution. The experiments performed on this topic still need to be deepened. In particular, it is necessary to clarify the effect of the shape matching between the crown ether and sodium. For that reason, it would be interesting to change the alkali metal, using lithium or potassium to test the affinity as future perspective for this experimental line.

BIBLIOGRAPHY:

1.   Amabilino, D. B. & Royal Society of Chemistry (Great Britain). *Supramolecular chemistry at surfaces*.

2.   Feng, Z., Kladnik, G., Comelli, G., Dri, C. & Cossaro, A. Growth of regular nanometric molecular arrays on a functional 2D template based on a chemical guest–host approach. *Nanoscale* **10,** 2067–2072 (2018).

3.   Gokel, G. W., Leevy, W. M. & Weber, M. E. Crown ethers: Sensors for ions and molecular scaffolds for materials and biological models. *Chem. Rev.* **104,** 2723–2750 (2004).

4.   Farfán, N. & Contreras, R. Carbon-13 nuclear magnetic resonance spectroscopy as a method to determine relative acidity of boron Lewis acids in pyridine complexes. *J. Chem. Soc., Perkin Trans. 2* **0,** 771–773 (1987).

5.   Pearson, R. G. Hard and soft acids and bases. *J. Am. Chem. Soc.* **85,** 3533–3539 (1963).

6.   Dusemund, C., Sandanayake, K. R. A. S. & Shinkai, S. Selective fluoride recognition with ferroceneboronic acid. *J. Chem. Soc. Chem. Commun.* **0,** 333 (1995).

7.   James, T. D., Sandanayake, K. R. A. S. & Shinkai, S. Saccharide Sensing with Molecular Receptors Based on Boronic Acid. *Angew. Chemie Int. Ed. English* **35,** 1910–1922 (1996).

8.   Nicolas, M., Fabre, B., Marchand, G. & Simonet, J. New Boronic-Acid- and Boronate-Substituted Aromatic Compounds as Precursors of Fluoride-Responsive Conjugated Polymer Films. *European J. Org. Chem.* **2000,** 1703–1710 (2000).

9.   Dzidic, I. Relative gas-phase basicities of some amines, anilines, and pyridines. Application of some Broensted acids as reactants in chemical ionization mass spectrometry. *J. Am. Chem. Soc.* **94,** 8333–8335 (1972).

10.   Dri, C. *et al.* Chemistry of the Methylamine Termination at a Gold Surface: From Autorecognition to Condensation. *J. Phys. Chem. C* **120,** 6104–6115 (2016).

11.   Perttu, E. K., Arnold, M. & Iovine, P. M. The synthesis and characterization of phenylacetylene tripodal compounds containing boroxine cores. *Tetrahedron Lett.* **46,** 8753–8756 (2005).

12.   *Boronic Acids*. (Wiley-VCH Verlag GmbH & Co. KGaA, 2011). doi:10.1002/9783527639328

13.   Pedersen, C. J. Cyclic Polyethers and Their Complexes with Metal Salts. *J. Am. Chem. Soc.* **89,** 7017–7036 (1967).

14.   Takami, T., Son, J. W., Lee, J. K., Park, B. H. & Kawai, T. Separate detection of sodium and potassium ions with sub-micropipette probe. *Jpn. J. Appl. Phys.* **50,** (2011).

15.   Nakajima, M., Kimura, K. & Shono, T. Liquid Chromatography of Alkali and Alkaline Earth Metal Salts on Poly(benzo-15-crown-5)- and Bis(benzo-15-crown-5)-Modified Silicas. *Anal. Chem.* **55,** 463–467 (1983).

16.   Mohammadzadeh Kakhki, R. Application of crown ethers as stationary phase in the chromatographic methods. *J. Incl. Phenom. Macrocycl. Chem.* **75,** 11–22 (2013).

17. Gong, Y. H. & Lee, H. K. Enantiomeric separations in capillary electrochromatography with crown ether-capped beta-cyclodextrin-bonded silica particles as chiral stationary phase. *Helv. Chim. Acta* **85,** 3283–3293 (2002).

18. Gokel, G. W. & Carasel, I. A. Biologically active, synthetic ion transporters. *Chem. Soc. Rev.* **36,** 378–389 (2007).

19. Carmichael, V. E. *et al.* Biomimetic Ion Transport: A Functional Model of a Unimolecular Ion Channel. *J. Am. Chem. Soc.* **111,** 767–769 (1989).

20. Gokel, G. W. & Negin, S. Synthetic ion channels: From pores to biological applications. *Acc. Chem. Res.* **46,** 2824–2833 (2013).

21. Bulach, V., Mandon, D. & Weiss, R. The High-Yield Synthesis and Characterization of the First Porphyrin–Cyclam Dinucleating Ligand and Its Iron(III)/Copper(II) Complex. *Angew. Chemie Int. Ed. English* **30,** 572–575

22. Even, P. & Boitrel, B. Crown porphyrins. *Coord. Chem. Rev.* **250,** 519–541 (2006).

23. Jing-Song, Y., You-Fa, X., Xiao-Qi, Y., Ai-Xia, C. & Zhong-Wei, L. Epoxidation of styrene catalyzed by manganese (III) porphyrins supported on chloromethylated polystyrene resin bearing crown ether groups,. *Chin. Chem. Lett.* **14,** 303–309 (2010).

24. Banfi, S., Manfredi, A., Montanari, F., Pozzi, G. & Ursino, F. Mn (III) -tetraarylporphyrins bearing covalently bonded crown-ethers : synthesis and catalytic activity in 1 -dodecene epoxidation promoted by aqueous HOCl / OCl-. *J. Mol. Catal. A. Chem.* **113,** 369–377 (1996).

25. Iwata, S., Suzuki, M., Shirakawa, M. & Tanaka, K. Cation and Anion Recognition of Crown Ether-armed Metalloporphyrin. *Supramol. Chem.* **11,** 135–141 (1999).

26. Ruiz-Hitzky, E., Aranda, P., Darder, M. & Ogawa, M. Hybrid and biohybrid silicate based materials: molecular vs. block-assembling bottom–up processes. *Chem. Soc. Rev.* **40,** 801–828 (2011).

27. Kuang, H. *et al.* Crown ether assembly of gold nanoparticles: Melamine sensor. *Biosens. Bioelectron.* **26,** 2032–2037 (2011).

28. Francisco Arias, Luis A. Godínez, Stephen R. Wilson, Angel E. Kaifer and Luis Echegoyen, Interfacial Hydrogen Bonding. Self-Assembly of a Monolayer of a Fullerene–Crown Ether Derivative on Gold Surfaces Derivatized with an Ammonium-Terminated Alkanethiolate. (1996). doi:10.1021/JA960445G

29. and, Y. M., Kimura, S., Imanishi, Y. Umemura, J. Self-Assembly of α-Helix Peptide/Crown Ether Conjugate upon Complexation with Ammonium-Terminated Alkanethiolate. (1998). doi:10.1021/LA970989B

30. Simon Flink, Frank C. J. M. van Veggel and & Reinhoudt, D. N. Recognition of Cations by Self-Assembled Monolayers of Crown Ethers. (1999). doi:10.1021/JP990014V

31. Simon Flink, Bernard A. Boukamp, Albert van den Berg, Frank C. J. M. van Veggel and David N. Reinhoudt, Electrochemical Detection of Electrochemically Inactive Cations by Self-Assembled Monolayers of Crown Ethers. (1998). doi:10.1021/JA9734713

32. Chu, I. H., Zhang, H. & Dearden, D. V. Macrocyclic Chemistry in the Gas Phase: Intrinsic Cation Affinities and Complexation Rates for Alkali Metal Cation Complexes of Crown Ethers and

Glymes. *J. Am. Chem. Soc.* **115,** 5736–5744 (1993).

33. Calabrese, A., Floreano, L., Verdini, A., Mariani, C. & Betti, M. G. Filling empty states in a CuPc single layer on the Au(110) surface via electron injection. *Phys. Rev. B* **79,** 115446 (2009).

34. Auwärter, W. *et al.* Site-specific electronic and geometric interface structure of Co-tetraphenyl-porphyrin layers on Ag(111). *Phys. Rev. B* **81,** 245403 (2010).

35. Di Santo, G. *et al.* Conformational Adaptation and Electronic Structure of 2H-Tetraphenylporphyrin on Ag(111) during Fe Metalation. *J. Phys. Chem. C* **115,** 4155–4162 (2011).

36. Watcharinyanon, S. *et al.* Molecular orientation of thiol-derivatized tetraphenylporphyrin on gold studied by XPS and NEXAFS. *Surf. Sci.* **603,** 1026–1033 (2009).

37. Cossaro, A. *et al.* Tailoring SAM-on-SAM Formation. *J. Phys. Chem. Lett.* **2,** 3124–3129 (2011).

38. Schwieger, T., Peisert, H., Golden, M. S., Knupfer, M. & Fink, J. Electronic structure of the organic semiconductor copper phthalocyanine and K-CuPc studied using photoemission spectroscopy. *Phys. Rev. B* **66,** 155207 (2002).

39. Molodtsova, O. V., Zhilin, V. M., Vyalikh, D. V., Aristov, V. Y. & Knupfer, M. Electronic properties of potassium-doped CuPc. *J. Appl. Phys.* **98,** 093702 (2005).

40. Feng, Z., Kladnik, G., Comelli, G., Dri, C. & Cossaro, A. Growth of Regular Nanometric Molecular Arrays on a Functional 2D template Based on a Chemical Guest-Host Approach. *Nanoscale* (2018). doi:10.1039/C7NR08017D

CONCLUSIONS

In the present thesis, three classes of systems have been investigated, which rely on the formation *in situ* of complex interfaces on metal surfaces. The scientific issues we tackled open to the possible exploitation of the systems as prototypical material heterostructures to build novel electronic devices. The research protocols we adopted combine X-ray spectroscopy with both STM and DFT calculations and demonstrate that such multi-technique approach is required when the complexity of the studied system increases.

A relevant part of the research activity related to my work has been devoted to the study of the on-surface synthesis of boroxine systems. We have carried out a primarily spectroscopic investigation that allowed us to evidence the presence of ultra-fast charge delocalization at the boroxine-gold interface. Moreover, we have also synthesized a novel 2D material, consisting in boron and oxygen atoms only, that shows band dispersion. These results allow to gain a new perspective in the boroxine based systems for application in the nano-electronics field. In addition, the spectroscopic inquiry has proven to be efficient also in the approach to more complex systems. One of the boroxine molecules synthesized on the surface has been investigated as a possible anchoring point for an amine, taking advantage of the acid-base interaction. It has been possible to follow the change in geometry confirming the occurrence of the reaction. This continuation of the boronic work opens to the application of many other 2D selective assembly of molecules, making this class of materials even more interesting. For that purpose, it is possible to continue this work changing both the partners of interaction, the boronic acid precursor and the amine. One of the possible achievements is to take advantage of the 2D order characterizing the boroxine-based systems to anchor amino group containing molecules in precise position over a surface, in a reversible way. Similar to the complex architecture built on the TNB, we have also been able to apply our investigation tools to the second complex system presented. The interplay between the employed molecules, the porphyrin and the crown ether has been crucial in order to obtain an ordered molecular arrangement of the substrate. In this thesis, for the first time the interaction between an alkali metal and a crown ether in ultra high vacuum has been addressed. Once again, we found out X-ray analysis to be the suitable tool for monitoring the possible sodium adsorption sites and confirming the extraordinary affinity of the crown ethers toward the alkali metals that could be exploited in future for sensors or traps on a surface under controlled conditions. These important findings can be extended by further studies. A possible prosecution can involve the change of the alkali metal, in order to monitor the correlation of the selectivity and the shape matching between the macrocycle and the alkali metal. The melamine and melem systems are also characterized by the presence of weak interaction between the molecules deposited on the surface. Despite of this similarity with the previous scientific cases, the application target was completely different. We were not interested in building structures on a substrate, but we decided to take advantage offered by the UHV to study the behavior of molecules important in catalysis. In this case, we have studied the melamine and melem molecules, precursors of the 2D carbon nitride, an interesting photocatalyst for the water splitting reaction. We have been able to retrieve valuable information gaining a deeper insight in the H-bonding properties of the monitored molecules. This experimental line can also represent an important rout toward innovation in the photocatalytic

application of the carbon nitride. In conclusion, the studies reported in the present work represent examples of the state of the art of what can be done in terms of chemical/physical characterization of complex architectures grown on surfaces. In view of an effective employment of these systems in prototype devices, a further step towards the real working conditions has to be made. On one hand, the access to Near Ambient Pressure (NAP) spectroscopic techniques as well as to operando experiments would allow for testing the stability of the systems once operating and exposed to *quasi* ambient conditions; on the other hand, in order to optimize the interfaces performances in terms of charge transport, a more complete analysis of the electronic dynamics of the systems is required, which could be obtained by means of time resolved spectroscopy like pump and probe or resonant photoemission spectroscopies.

ACKNOWLEDGMENTS